

**ELECTRONIC CORRELATIONS IN
METALLOPROTEINS: A QUANTUM MONTE
CARLO STUDY**

**A Thesis Submitted to
the Graduate School of Engineering and Sciences of
İzmir Institute of Technology
in Partial Fulfillment of the Requirements for the Degree of**

MASTER OF SCIENCE

in Physics

**by
Selma MAYDA**

**July 2013
İZMİR**

We approve the thesis of **Selma MAYDA**

Examining Committee Members:

Prof. Dr. Nejat BULUT

Department of Physics, Izmir Institute of Technology

Prof. Dr. R. Tuğrul SENGER

Department of Physics, Izmir Institute of Technology

Prof. Dr. Nuran ELMACI

Department of Chemistry, Izmir Institute of Technology

12 July 2013

Prof. Dr. Nejat BULUT

Supervisor, Department of Physics
Izmir Institute of Technology

Prof. Dr. Nejat BULUT

Head of the Department of Physics

Prof. Dr. R. Tuğrul SENGER

Dean of the Graduate School of
Engineering and Sciences

ACKNOWLEDGMENTS

First and foremost, I would like to thank my adviser Professor Nejat Bulut for his encouraging, support, patience and guidance that he always gave. The environment that he provided us at Iztech Physics Department satisfied studying more efficiently and his lectures on many-body physics help me to understand many things about my field. He will always be a special person for me.

I would like to thank my office and group mate Zafer Kandemir for his friendship and discussion on our topics.

I am very grateful to Cihan Bacaksız for his help and many interesting discussions on physics.

Finally, I would like to express my gratitude to my family for their support and love.

ABSTRACT

ELECTRONIC CORRELATIONS IN METALLOPROTEINS: A QUANTUM MONTE CARLO STUDY

Metalloproteins are proteins that contain a metal atom. Some metalloproteins include a transition metal such as vitamin B₁₂ (Co) and hemoglobin (Fe) and these structures show semiconducting properties. In this thesis, as an example of metalloproteins, vitamin B₁₂ is studied and electronic and magnetic properties of Co *3d* electrons are examined by the quantum Monte Carlo method (QMC). Since vitamin B₁₂ contains a cobalt (Co) atom and has a semiconductor gap, its electronic and magnetic properties can be described by multi-orbital Haldane-Anderson model. Haldane-Anderson model explains the electronic properties of semiconductors which contain a transition metal impurity and considers the onsite Coulomb interactions of impurity *3d* orbitals. To solve this model, we use Hirsch-Fye quantum Monte Carlo algorithm (HFQMC) without making any approximations. Firstly, the occupations and intra-orbital electronic correlations of *3d* orbitals are calculated. After that, the total magnetization and the inter-orbital correlations of *3d* orbitals are obtained. Next, the total magnetic susceptibility and magnetic susceptibilities between the *3d* orbitals are calculated. Finally, we discuss the physical meaning of the QMC calculations.

ÖZET

METALOPROTEİNLERDE ELEKTRONİK BAĞLILIKLAR: KUANTUM MONTE CARLO ÇALIŞMASI

Metaloproteinler bir metal atomu içeren proteinlerdir. Vitamin B₁₂ (Co) ve hemoglobin (Fe) gibi metaloproteinler bir geçiş metali içerirler ve yarıiletken özelliği gösterirler. Bu tezde, metaloproteinlere örnek olarak, vitamin B₁₂ çalışılmış ve Co 3*d* orbitallerinin elektronik ve manyetik özellikleri kuantum Monte Carlo (QMC) metodu ile açıklanmıştır. Vitamin B₁₂ kobalt (Co) atomu içerdiği ve yarıiletken band aralığına sahip olduğu için onun elektronik ve manyetik özellikleri çok-orbitalli Haldane-Anderson modeli ile tanımlanır. Haldane-Anderson modeli geçiş-metali safsızlık atomu içeren yarıiletken yapıların elektronik özelliklerini açıklar ve safsızlık 3*d* orbitallerindeki Coulomb etkileşmelerini hesaba katar. Bu modeli çözmek için Hirsch-Fye kuantum Monte Carlo algoritmasını (HFQMC) hiç bir yaklaşım yapmaksızın kullandık. İlk olarak, safsızlık 3*d* orbitallerinin doluluk oranları ve orbital içi elektronik bağılıkları hesaplanmıştır. Daha sonra 3*d* orbitallerinin toplam manyetizasyonu ve 3*d* orbitalleri arası bağılıklar açıklanmıştır. Bunun ardından, toplam manyetik alınganlık ve 3*d* orbitalleri arası manyetik alınganlıklar hesaplanmıştır. Son olarak QMC hesaplarının fiziksel anlamları tartışılmıştır.

TABLE OF CONTENTS

LIST OF FIGURES	viii
LIST OF TABLES	xi
CHAPTER 1. INTRODUCTION	1
CHAPTER 2. ANDERSON MODEL FOR ELECTRONIC STRUCTURE OF VI- TAMIN B ₁₂	6
CHAPTER 3. QUANTUM MONTE CARLO MEASUREMENTS	8
3.1. Static quantum Monte Carlo measurements	9
3.2. Dynamical quantum Monte Carlo measurements.....	11
CHAPTER 4. RESULTS FOR STATIC QUANTUM MONTE CARLO MEA- SUREMENTS	13
4.1. Occupations of <i>3d</i> orbitals	13
4.1.1. Comparison of QMC results and DFT results for occupations of <i>3d</i> orbitals.....	13
4.2. Semiconductor gap	14
4.2.1. Comparison of QMC results and DFT results for semicon- ductor gap.....	15
4.3. Impurity magnetic correlation functions	15
4.3.1. Comparison of QMC results and DFT results for effective magnetic moment	16
4.4. Total impurity magnetic correlation function	17
CHAPTER 5. RESULTS FOR DYNAMICAL QUANTUM MONTE CARLO MEA- SUREMENTS	36
CHAPTER 6. CONCLUSION	46
REFERENCES	49

APPENDICES

APPENDIX A. HIRSCH-FYE QUANTUM MONTE CARLO ALGORITHM FOR
THE SINGLE-IMPURITY ANDERSON MODEL 51

APPENDIX B. HIRSCH-FYE QUANTUM MONTE CARLO ALGORITHM FOR
THE MULTI-ORBITAL ANDERSON MODEL 68

APPENDIX C. CALCULATION OF THE HOST-IMPURITY AND HOST GREEN'S
FUNCTIONS 83

LIST OF FIGURES

Figure	Page
Figure 1.1. Structure of hemoglobin	1
Figure 1.2. Structure of vitamin B ₁₂	2
Figure 1.3. Density of states of vitamin B ₁₂	3
Figure 1.4. (Ga,Mn)As	3
Figure 1.5. Band structure of GaAs	4
Figure 4.1. 3 <i>d</i> orbitals from the QMC measurements and DFT measurements	14
Figure 4.2. High spin state and low spin state of Co 3 <i>d</i> ⁵	18
Figure 4.3. Total magnetic correlations of 3 <i>d</i> orbitals $\langle (M^z)^2 \rangle$ vs temperature <i>T</i> . ..	19
Figure 4.4. Measurements at <i>T</i> = 600 K for $\langle (M^z)^2 \rangle$	20
Figure 4.5. Spin states for $\mu_{eff}^T = 3$ and spin states for $\mu_{eff}^T = 1.7$	21
Figure 4.6. Onsite Coulomb interaction of 3 <i>d</i> orbitals <i>U</i> = 4 eV. Occupations of 3 <i>d</i> orbitals $\langle n_\nu \rangle$ vs <i>T</i>	22
Figure 4.7. Onsite Coulomb interaction of 3 <i>d</i> orbitals <i>U</i> = 4 eV. Red solid line shows HOMO and red dash line shows LUMO. (a) Occupations of 3 <i>d</i> orbitals $\langle n_\nu \rangle$ vs μ at temperature <i>T</i> = 300 K. (b) Occupations of 3 <i>d</i> orbitals $\langle n_\nu \rangle$ vs μ at temperature <i>T</i> = 600 K.	23
Figure 4.8. Onsite Coulomb interaction of 3 <i>d</i> orbitals <i>U</i> = 8 eV. Red solid line shows HOMO and red dash line shows LUMO. (a) Occupations of 3 <i>d</i> orbitals $\langle n_\nu \rangle$ vs μ at temperature <i>T</i> = 300 K. (b) Occupations of 3 <i>d</i> orbitals $\langle n_\nu \rangle$ vs μ at temperature <i>T</i> = 600 K.	24
Figure 4.9. Red solid line shows HOMO and red dash line shows LUMO. (a) Onsite Coulomb interaction of 3 <i>d</i> orbitals <i>U</i> = 4 eV and occupations of 3 <i>d</i> orbitals $\langle n_\nu \rangle$ vs μ at temperature <i>T</i> = 300 K. (b) Onsite Coulomb interaction of 3 <i>d</i> orbitals <i>U</i> = 8 eV and occupations of 3 <i>d</i> orbitals $\langle n_\nu \rangle$ vs μ at temperature <i>T</i> = 300 K.	25
Figure 4.10. Red solid line shows HOMO and red dash line shows LUMO. Blue solid line is energy level of $3z^2 - r^2$. For $3z^2 - r^2$ orbital, $\langle n_\nu \rangle$ vs μ at temperature <i>T</i> = 300 K for <i>U</i> = 4 eV and <i>U</i> = 8 eV and $\rho_\nu(\varepsilon)$ vs ε at temperature <i>T</i> = 300 K for <i>U</i> = 4 eV and <i>U</i> = 8 eV.	26
Figure 4.11. Onsite Coulomb interaction <i>U</i> = 4 eV. (a) Impurity magnetic correlation function $\langle (M_\nu^z)^2 \rangle$ vs temperature <i>T</i> . (b) Impurity effective magnetic moment $\mu_{eff,\nu}$ vs temperature <i>T</i>	27

- Figure 4.12. Onsite Coulomb interaction $U = 4$ eV. Red solid line shows HOMO and red dash line shows LUMO. (a) Impurity magnetic correlation function $\langle (M_\nu^z)^2 \rangle$ vs μ at temperature $T = 300$ K. (b) Impurity magnetic correlation function $\langle (M_\nu^z)^2 \rangle$ vs μ at temperature $T = 600$ K. 28
- Figure 4.13. Onsite Coulomb interaction $U = 8$ eV. Red solid line shows HOMO and red dash line shows LUMO. (a) Impurity magnetic correlation function $\langle (M_\nu^z)^2 \rangle$ vs μ at temperature $T = 300$ K. (b) Impurity magnetic correlation function $\langle (M_\nu^z)^2 \rangle$ vs μ at temperature $T = 600$ K. 29
- Figure 4.14. Temperature $T = 300$ K. Red solid line shows HOMO and red dash line shows LUMO. (a) Impurity magnetic correlation function $\langle (M_\nu^z)^2 \rangle$ vs μ for onsite Coulomb interaction $U = 4$ eV. (b) Impurity magnetic correlation function $\langle (M_\nu^z)^2 \rangle$ vs μ for onsite Coulomb interaction $U = 8$ eV. 30
- Figure 4.15. Number of warmup and measurement sweeps are shown as $N \times (\text{warmup} + \text{measurements})$. N is the number of simulations. For $T = 200$ K $14 \times (1k + 1k)$, $T = 300$ K $9 \times (5k + 10k)$, $T = 460$ K $10 \times (1k + 16k)$, $T = 600$ K $32 \times (10k + 50k)$, $T = 770$ K $10 \times (10k + 480k)$, $T = 1160$ K $40 \times (1k + 80k)$. (a) Total impurity magnetic correlation function of Co $3d$ $\langle (M^z)^2 \rangle$ vs temperature T . Dash line shows the $\sum_{\nu=1}^5 \langle (M_\nu^z)^2 \rangle$. (b) Total effective magnetic moment of Co $3d$ electrons μ_{eff}^T vs temperature T 31
- Figure 4.16. Number of warmup and measurement sweeps are shown as $N \times (\text{warmup} + \text{measurements})$. N is the number of simulations. For $T = 200$ K $14 \times (1k + 1k)$, $T = 300$ K $9 \times (5k + 10k)$, $T = 460$ K $10 \times (1k + 16k)$, $T = 600$ K $32 \times (10k + 50k)$, $T = 770$ K $10 \times (10k + 480k)$, $T = 1160$ K $40 \times (1k + 80k)$. (a) Total impurity magnetic correlation function $\langle (M^z)^2 \rangle$ vs temperature T . Dash line shows the $\sum_{\nu=1}^5 \langle (M_\nu^z)^2 \rangle$. (b) Magnetic correlation function $\langle M_\nu^z M_{\nu'}^z \rangle$ between the $3z^2 - r^2$ and xy orbitals vs temperature T 32

- Figure 4.17. Onsite Coulomb interaction $U = 4$ eV. Number of warmup and measurement sweeps are shown as $N \times (\text{warmup} + \text{measurements})$. N is the number of simulations. For $T = 300$ K $9 \times (5k + 10k)$, $T = 1550$ K $(1k + 60k)$. (a) Magnetic correlation function $\langle M_\nu^z M_{\nu'}^z \rangle$ between the $3d$ orbitals vs $3d$ orbitals ν at temperature $T = 300$ K. (b) Magnetic correlation function $\langle M_\nu^z M_{\nu'}^z \rangle$ between the $3d$ orbitals vs $3d$ orbitals ν at temperature $T = 1550$ K. 33
- Figure 4.18. Number of warmup and measurement sweeps are shown as $N \times (\text{warmup} + \text{measurements})$. N is the number of simulations. For $T = 200$ K $10 \times (1k + 1k)$, $T = 300$ K $10 \times (5k + 10k)$, $T = 460$ K $6 \times (5k + 80k)$, $T = 600$ K $10 \times (10k + 50k)$, $T = 770$ K $10 \times (10k + 480k)$, $T = 1160$ K $10 \times (1k + 80k)$. (a) Total impurity magnetic correlation function $\langle (M^z)^2 \rangle$ vs temperature T . Dash line shows the $\sum_{\nu=1}^5 \langle (M_\nu^z)^2 \rangle$. (b) Magnetic correlation function $\langle M_\nu^z M_{\nu'}^z \rangle$ between the $3z^2 - r^2$ and xy orbitals vs temperature T 34
- Figure 4.19. Onsite Coulomb interaction $U = 8$ eV. Number of warmup and measurement sweeps are shown as $N \times (\text{warmup} + \text{measurements})$. N is the number of simulations. For $T = 300$ K $10 \times (5k + 10k)$, $T = 1550$ K $(1k + 40k)$. (a) Magnetic correlation function $\langle M_\nu^z M_{\nu'}^z \rangle$ between the $3d$ orbitals vs $3d$ orbitals ν at temperature $T = 300$ K. (b) Magnetic correlation function $\langle M_\nu^z M_{\nu'}^z \rangle$ between the $3d$ orbitals vs $3d$ orbitals ν at temperature $T = 1550$ K. 35
- Figure 5.1. Number of warmup and measurement sweeps are shown as (warmup + measurements). For $T = 200$ K $(1k + 1k)$, $T = 300$ K $(5k + 10k)$, $T = 450$ K $(5k + 10k)$, $T = 600$ K $(5k + 80k)$, $T = 800$ K $(10k + 100k)$, $T = 1000$ K, $(5k + 80k)$ $T = 1200$ K $(5k + 80k)$, $T = 1500$ $(5k + 80k)$. Red solid line shows magnetic susceptibility of 5 free spin. Red dash line shows magnetic susceptibility of 1 free spin. Black solid line is total magnetic susceptibility $\chi(i\omega_m = 0)$ vs temperature T 38

Figure 5.2. Number of warmup and measurement sweeps are shown as (warmup + measurements). For $T = 200$ K ($1k + 1k$), $T = 300$ K ($5k + 10k$), $T = 450$ K ($5k + 10k$), $T = 600$ K ($5k + 80k$), $T = 800$ K ($10k + 100k$), $T = 1000$ K, ($5k + 80k$) $T = 1200$ K ($5k + 80k$), $T = 1500$ K ($5k + 80k$). Red dash line shows magnetic susceptibility of 1 free spin. (a) Magnetic susceptibility between $3z^2 - r^2$ and the other Co $3d$ orbitals $\chi_{1\nu}(i\omega_m = 0)$ vs temperature T . (b) Magnetic susceptibility between xy and the other Co $3d$ orbitals $\chi_{2\nu}(i\omega_m = 0)$ vs temperature T 39

Figure 5.3. Number of warmup and measurement sweeps are shown as (warmup + measurements) . For $T = 200$ K ($1k + 1k$), $T = 300$ K ($5k + 10k$), $T = 450$ K ($5k+10k$), $T = 600$ K ($5k+80k$), $T = 800$ K ($10k+100k$), $T = 1000$ K, ($5k + 80k$) $T = 1200$ K ($5k + 80k$), $T = 1500$ K ($5k + 80k$). Red dash line shows magnetic susceptibility of 1 free spin. (a) Magnetic susceptibility between yz and the other Co $3d$ orbitals $\chi_{3\nu}(i\omega_m = 0)$ vs temperature T . (b) Magnetic susceptibility between $x^2 - y^2$ and the other Co $3d$ orbitals $\chi_{4\nu}(i\omega_m = 0)$ vs temperature T 40

Figure 5.4. Number of warmup and measurement sweeps are shown as (warmup + measurements) . For $T = 200$ K ($1k + 1k$), $T = 300$ K ($5k + 10k$), $T = 450$ K ($5k + 10k$), $T = 600$ K ($5k + 80k$), $T = 800$ K ($10k + 100k$), $T = 1000$ K, ($5k + 80k$) $T = 1200$ K ($5k + 80k$), $T = 1500$ K ($5k + 80k$). Red dash line shows magnetic susceptibility of 1 free spin. Magnetic susceptibility between xz and the other Co $3d$ orbitals $\chi_{5\nu}(i\omega_m = 0)$ vs temperature T 41

Figure 5.5. Number of warmup and measurement sweeps are shown as (warmup + measurements). For $T = 300$ K ($5k + 10k$), $T = 450$ K ($5k + 10k$), $T = 600$ K ($5k+80k$), $T = 800$ K ($5k+80k$), $T = 1000$ K, ($5k+80k$) $T = 1200$ K ($5k + 80k$), $T = 1500$ ($5k + 80k$). Red solid line shows magnetic susceptibility of 5 free spin. Red dash line shows magnetic susceptibility of 1 free spin. Onsite Coulomb interactions of $3d$ orbitals are $U = 8$ eV. Total magnetic susceptibility $\chi(i\omega_m = 0)$ vs temperature T 42

Figure 5.6. Number of warmup and measurement sweeps are shown as (warmup + measurements). For $T = 300$ K ($5k + 10k$), $T = 450$ K ($5k + 10k$), $T = 600$ K ($5k + 80k$), $T = 800$ K ($5k + 80k$), $T = 1000$ K, ($5k + 80k$) $T = 1200$ K ($5k + 80k$), $T = 1500$ ($5k + 80k$). Red dash line shows magnetic susceptibility of 1 free spin. (a) Magnetic susceptibility between $3z^2 - r^2$ and the other Co $3d$ orbitals $\chi_{1\nu}(i\omega_m = 0)$ vs temperature T . (b) Magnetic susceptibility between xy and the other Co $3d$ orbitals $\chi_{2\nu}(i\omega_m = 0)$ vs temperature T 43

Figure 5.7. Number of warmup and measurement sweeps are shown as (warmup + measurements). For $T = 300$ K ($5k + 10k$), $T = 450$ K ($5k + 10k$), $T = 600$ K ($5k + 80k$), $T = 800$ K ($5k + 80k$), $T = 1000$ K, ($5k + 80k$) $T = 1200$ K ($5k + 80k$), $T = 1500$ ($5k + 80k$). Red dash line shows magnetic susceptibility of 1 free spin. (a) Magnetic susceptibility between yz and the other Co $3d$ orbitals $\chi_{3\nu}(i\omega_m = 0)$ vs temperature T . (b) Magnetic susceptibility between $x^2 - y^2$ and the other Co $3d$ orbitals $\chi_{4\nu}(i\omega_m = 0)$ vs temperature T 44

Figure 5.8. Number of warmup and measurement sweeps are shown as (warmup + measurements). For $T = 300$ K ($5k + 10k$), $T = 450$ K ($5k + 10k$), $T = 600$ K ($5k + 80k$), $T = 800$ K ($5k + 80k$), $T = 1000$ K, ($5k + 80k$) $T = 1200$ K ($5k + 80k$), $T = 1500$ ($5k + 80k$). Red dash line shows magnetic susceptibility of 1 free spin. Magnetic susceptibility between xz and the other Co $3d$ orbitals $\chi_{5\nu}(i\omega_m = 0)$ vs temperature T 45

LIST OF TABLES

<u>Table</u>		<u>Page</u>
Table 4.1.	QMC, DFT and LSDA results for occupations of $3d$ orbitals.	14
Table 4.2.	QMC, DFT and LSDA results for semiconductor gap Δ (eV).	16
Table 4.3.	QMC, DFT and LSDA results for magnetic moment of $3d$ electrons. ...	17

CHAPTER 1

INTRODUCTION

Proteins are the most important constituents of living cells and they are responsible for many essential functions in living organisms [1]. It is known that one-third of all proteins contain a metal atom and these materials are named as metalloproteins [2]. Metalloproteins have attracted scientists' attention since the sperm whale myoglobin, the first X-ray crystal structure of protein, showed the presence of an iron atom in 1950s [3]. An important part of metalloproteins contain a transition metal such as iron (Fe), cobalt (Co), nickel (Ni) and zinc (Zi), and these metals are usually arranged by nitrogen, oxygen or sulfur atoms which belong to amino acids in the polypeptide chain in the proteins. Some examples for metalloproteins which contain transition metal atoms are hemoglobin (Fe), vitamin B₁₂ (Co) and enzymes. These structures are very important because metal

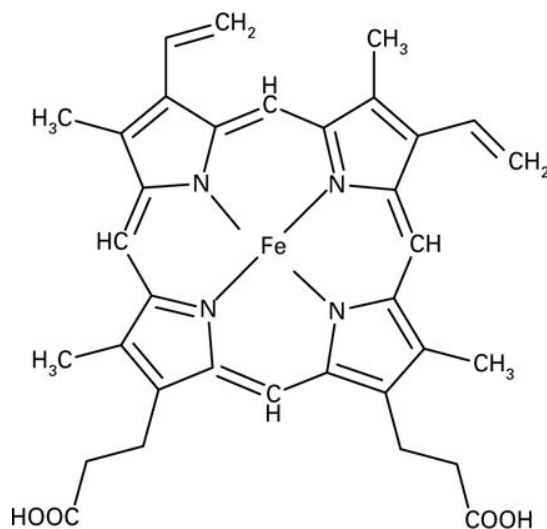


Figure 1.1. Structure of hemoglobin

imbalance or lack of activity of metalloproteins lead to many diseases [4]. Moreover, they are used for many biological processes such as transition O_2 and CO_2 through the cells, normal functioning of brain and nervous systems, transport and storage proteins, and it is

known that protein-bound transition metals play key roles in these processes [3], [4].

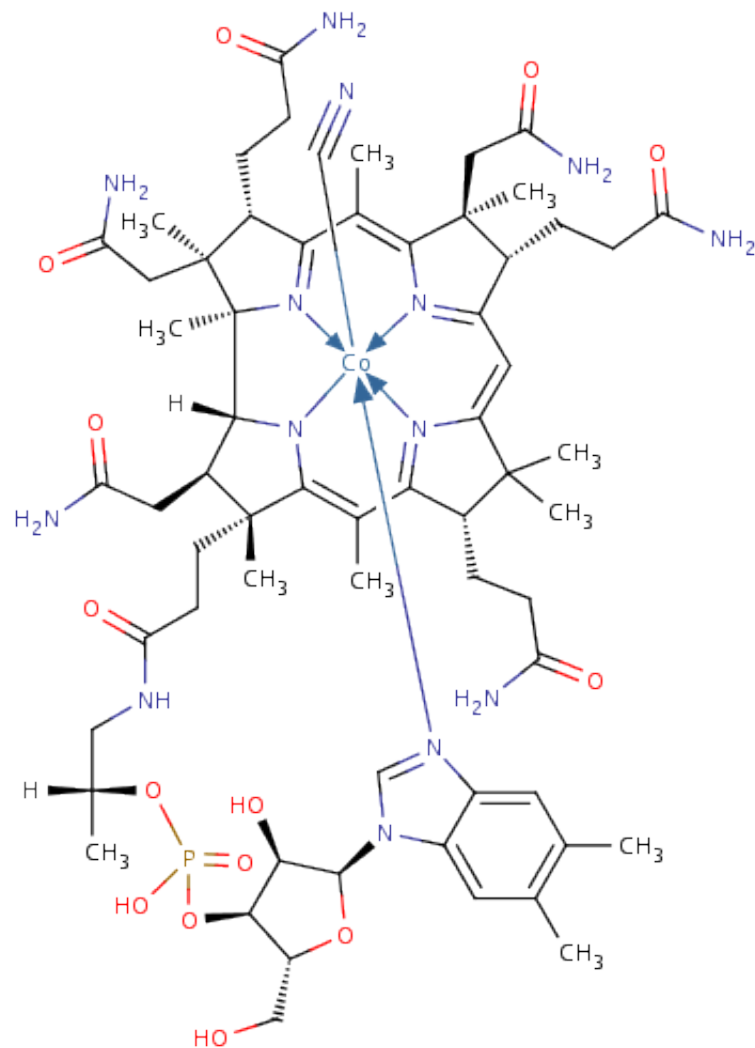


Figure 1.2. Structure of vitamin B₁₂

Although the importance of metalloproteins is widely known, the contribution of transition metals to the physics of metalloproteins and functions in many metalloproteins remain unclear [5].

To understand properties of metalloproteins, some researches have been done in recent years. For example, it has been found that hemoglobin and vitamin B₁₂ (see Fig.1.3) have energy gap and they show semiconducting properties [6], [7]. With these characteristics, they resemble diluted magnetic semiconductors (DMS).

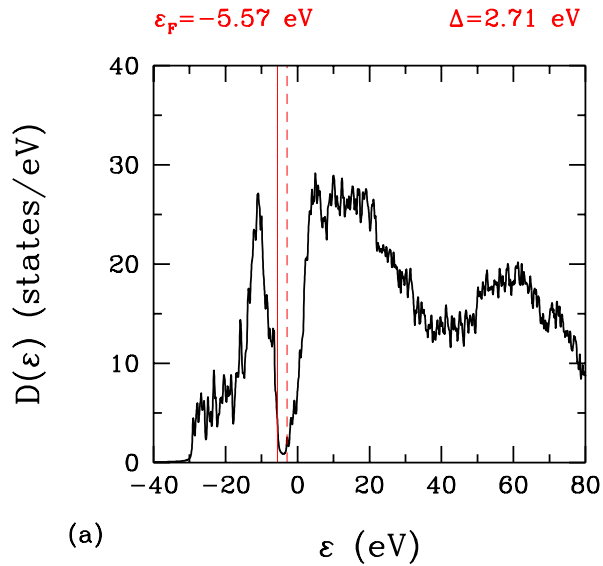


Figure 1.3. Density of states of vitamin B₁₂

DMS are semiconductor materials and show ferromagnetic properties. The idea of DMS is that a small fraction of the original atoms in the non-magnetic host is substituted by transition metals. Therefore, these materials are magnetic due to transition metals and semiconductor due to host structure. For example, (Ga,Mn)As, (In,Mn)As and (Ga,Mn)N are some DMS materials. Fig.1.4 shows (Ga,Mn)As. Here, GaAs is host structure which is a semiconductor as seen in Fig.1.5 and As are substituted by Mn. In DMS, magnetization is resulted from the local magnetic moments of the magnetic impurities and low-density carriers mediate magnetic interactions of impurities [8].

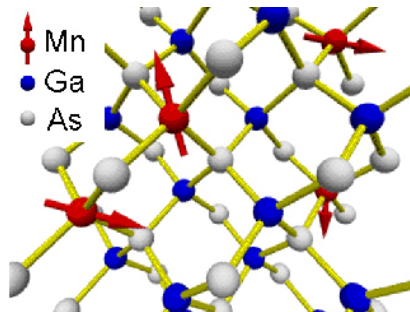


Figure 1.4. (Ga,Mn)As

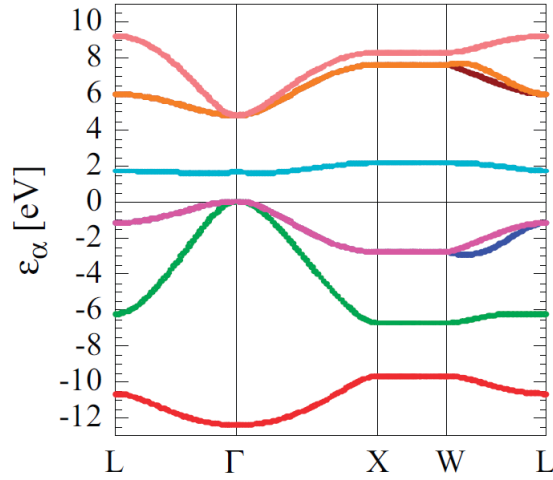


Figure 1.5. Band structure of GaAs

Unlike the traditional electronics, DMS materials have spin-dependent properties [9] and they allow control of quantum spin states [10]. With these characteristics, DMS are important for spintronics or semiconductor-based spin electronics which studies possible applications of electron spins in electronic devices. Therefore, to develop many DMS candidates and understand the origin of magnetism in these materials, many investigations have been carried out since 1980s [11].

In one of the studies on DMS, to understand their magnetic properties, Anderson model was used and the basic electronic structures of DMS were found [8]. This model was introduced by Anderson in [12] to study the multiple charge states of Au impurities in Ge. After that, Anderson model was extended to describe the electronic structure of transition metal impurities in semiconductors [13].

It is known that metalloproteins and DMS materials have similar structures. Both of them contain transition metal and show semiconducting properties. Therefore, to explain the electronic and magnetic properties of metalloproteins, like DMS materials, Anderson model can be used. Understanding of metalloproteins is very important in many aspects. Firstly, metalloproteins can help to interpret physics of DMS materials, which provides developing new electronic materials. Furthermore, explanation of properties of metalloproteins can help in the discovery of new chemical structures which contain transition metals.

In this thesis, electronic and magnetic properties of metalloproteins are studied by using the Anderson model. To study this model, density functional theory (DFT) and quantum Monte Carlo (QMC) methods are used together. This combined DFT+QMC ap-

proach is a "first principle" approach which treats exactly strong electronic correlations at the transition-impurity $3d$ orbitals. As an example for metalloproteins, vitamin B₁₂ is studied and here, by using the Hirsch-Fye QMC algorithm (HFQMC), the occupations, magnetic correlation functions, effective magnetic moments and susceptibilities of impurity $3d$ orbitals are calculated and presented.

In Chapter 2, the impurity Anderson Hamiltonian is introduced for single and multi-orbital cases. After that, in Chapter 3, physical quantities which we calculate through the static QMC measurements and dynamical QMC measurements are described. Results for the static QMC measurements are explained in Chapter 4 and in these, QMC results are compared with the DFT results. Next, the results for the dynamical QMC measurements are discussed in Chapter 5. Furthermore, HFQMC algorithm for single-orbital and multi-orbital cases are explained in Appendix A and Appendix B, respectively. Finally, in Appendix C, the calculation of host-impurity and host Green's functions are described.

CHAPTER 2

ANDERSON MODEL FOR ELECTRONIC STRUCTURE OF VITAMIN B₁₂

Haldane-Anderson model [13] is the extension of the Anderson model [12] to describe the electronic structure of transition metal impurities in semiconductors. The Anderson Hamiltonian is

$$H = \sum_{k\sigma} (\varepsilon_k - \mu) c_{k\sigma}^\dagger c_{k\sigma} + \sum_{\sigma} (\varepsilon_d - \mu) d_{\sigma}^\dagger d_{\sigma} + \sum_{k,\sigma} (V_k c_{k\sigma}^\dagger d_{\sigma} + h.c.) + U n_{d\uparrow} n_{d\downarrow} \quad (2.1)$$

Here, ε_k denotes the eigenvalues of the host electrons, $c_{k\sigma}^\dagger$ ($c_{k\sigma}$) is the creation (annihilation) operator for the host electrons, V_k is the hybridization term between the host and impurity electrons, ε_d denotes the eigenvalues of the impurity electrons, d_{σ}^\dagger (d_{σ}) is the creation (annihilation) operator for the impurity electrons, U specifies the Coulomb interaction on d sites and $n_{d\sigma}$ is the site occupation number of a d electron with $\sigma = \uparrow$ and $\sigma = \downarrow$ which denote the two orientations of the electron spins.

The above Anderson Hamiltonian is used for the single orbital case. However, in this thesis, the electronic structure of vitamin B₁₂ that contains Co as an impurity atom is studied. It is known that transition metal impurities have partially filled d or f orbitals [14] and so electron exchanges occur not only between the impurity and host states but also between the impurity states. Therefore, we have to expand single orbital case to multi-orbital Anderson model. If the Anderson Hamiltonian is rewritten for the multi-orbital case, it is

$$\begin{aligned} H = & \sum_{m\sigma} (\boxed{\varepsilon_m} - \boxed{\mu}) c_{m\sigma}^\dagger c_{m\sigma} + \sum_{m\sigma} \sum_{\nu=1}^5 (\boxed{V_{m\nu}} c_{m\sigma}^\dagger d_{\sigma\nu} + h.c.) \\ & + \sum_{\nu,\nu'=1}^5 \sum_{\sigma} (\boxed{t_{\nu\nu'}} d_{\nu\sigma}^\dagger d_{\nu'\sigma} + h.c.) + \sum_{\nu=1}^5 \sum_{\sigma} (\boxed{\varepsilon_{d\nu}} - \mu) n_{d\nu\sigma} \\ & + \sum_{\nu=1}^5 U_{\nu} n_{d\nu\uparrow} n_{d\nu\downarrow}. \end{aligned} \quad (2.2)$$

For single-orbital Anderson model, \vec{k} denotes the wave vector of the host lattice structure. But in the study of metalloproteins, m denotes the discrete host eigenstates. Furthermore, ν is the index of the d orbitals ranging from 1 to 5 and hopping terms between the $3d$ orbitals $t_{\nu\nu'}$ are used for multi-orbital Anderson model.

In this thesis, DFT and QMC methods are combined to study vitamin B₁₂. The terms which are eigenvalues of host and impurity electrons, chemical potential, hopping terms between the $3d$ orbitals and hybridizations of host and impurity orbitals are calculated by DFT (these terms have been shown in boxes in Eq.2.2). After that, these terms are placed in the Anderson Hamiltonian and electronic properties of vitamin B₁₂ have been described.

$$\begin{aligned}
H = & \sum_{m\sigma} (\varepsilon_m - \mu) c_{m\sigma}^\dagger c_{m\sigma} + \sum_{m\sigma} \sum_{\nu=1}^5 (V_{m\nu} c_{m\sigma}^\dagger d_{\sigma\nu} + h.c.) \\
& + \sum_{\nu,\nu'=1}^5 \sum_{\sigma} (t_{\nu\nu'} d_{\nu\sigma}^\dagger d_{\nu'\sigma} + h.c.) + \sum_{\nu=1}^5 \sum_{\sigma} (\varepsilon_{d\nu} - \mu) n_{d\nu\sigma} \\
& + \boxed{\sum_{\nu=1}^5 U_\nu n_{d\nu\uparrow} n_{d\nu\downarrow}} \tag{2.3}
\end{aligned}$$

With onsite Coulomb interactions of $3d$ orbitals U_ν , solving Anderson model is very difficult. Therefore, the numerical results which are discussed in Chapter 4 and Chapter 5 are obtained by HFQMC algorithm. In Appendix A, single-orbital HFQMC algorithm is explained and it was used in [8]. This algorithm is modified for multi-orbital case in Appendix B and it is used to obtain the electronic properties of vitamin B₁₂.

CHAPTER 3

QUANTUM MONTE CARLO MEASUREMENTS

By using multi-orbital Hirsch-Fye QMC technique (see Appendix B), the numerical results were obtained and these results will be represented in Chapter 4 and Chapter 5. With this method, the Green's functions of $3d$ orbitals

$$G_{\nu\nu'\uparrow}(\tau) = - \left\langle T_{\tau} d_{\nu\uparrow}(\tau' + \tau) d_{\nu'\uparrow}^{\dagger}(\tau') \right\rangle, \quad (3.1)$$

$$G_{\nu\nu'\downarrow}(\tau) = - \left\langle T_{\tau} d_{\nu\downarrow}(\tau' + \tau) d_{\nu'\downarrow}^{\dagger}(\tau') \right\rangle. \quad (3.2)$$

are calculated. Here, ν and ν' show the Co $3d$ orbitals and T_{τ} is the Matsubara time-ordering operator. Furthermore, algebra of the fermionic creation and annihilation operators is defined by the following anti-commutation relation:

$$\left\{ d_{\nu}, d_{\nu'}^{\dagger} \right\} = \delta_{\nu,\nu'} \quad (3.3)$$

and the expression for the magnetization and number operators are

$$M_{\nu}^z = d_{\nu\uparrow}^{\dagger} d_{\nu\uparrow} - d_{\nu\downarrow}^{\dagger} d_{\nu\downarrow}, \quad (3.4)$$

$$n_{\nu} = d_{\nu\uparrow}^{\dagger} d_{\nu\uparrow} + d_{\nu\downarrow}^{\dagger} d_{\nu\downarrow}. \quad (3.5)$$

With these information, firstly, the static QMC measurements were made and occupations of $3d$ orbitals $\langle n_{\nu} \rangle$, the equal-time magnetic correlation function $\langle (M_{\nu}^z)^2 \rangle$, total magnetic correlation function $\langle (M^z)^2 \rangle$ of $3d$ orbitals and magnetic correlation functions between $3d$ orbitals were calculated. After that, the dynamical QMC measurements were made. In this part, total magnetic susceptibility $\chi(i\omega_m)$ and the magnetic susceptibilities between $3d$ orbitals $\chi_{\nu\nu'}(i\omega_m)$ were obtained.

To obtain the QMC results, Matsubara time step was equaled $\Delta\tau = 0.3125$ and L values were equaled 16, 32, 48, 64, 128, 192 and 384. For some measurements, to set the temperature values, $\Delta\tau$ was changed a few. In addition, for simulations, number of

warm up sweeps and number of measurement sweeps were calibrated.

Warm up sweeps describe the thermalizes of system at the given temperature. During the warm up sweeps, only the Hubbard-Stratonovich spins (see Appendix A and B) flip to decrease the correlations and no any measurements are made. After warm up sweeps, measurements start. Large number of measurements are grouped into bins and then, by using standard deviation of bins, average values and error values are calculated. Measurement sweeps are simple way to improve the estimate of the QMC errors.

3.1. Static Quantum Monte Carlo Measurements

By using fermion operators, Green's functions, magnetization operator and Wick's theorem, occupations of $3d$ orbitals $\langle n_\nu \rangle$, the equal-time magnetic correlation function $\langle (M_\nu^z)^2 \rangle$, total magnetic correlation function $\langle (M^z)^2 \rangle$ of $3d$ orbitals and magnetic correlation functions between $3d$ orbitals were calculated and their equations are represented below, respectively.

The occupations of $3d$ orbitals are calculated by

$$\langle n_\nu \rangle = \left\langle d_{\nu\uparrow}^\dagger d_{\nu\uparrow} + d_{\nu\downarrow}^\dagger d_{\nu\downarrow} \right\rangle \quad (3.6)$$

$$= \frac{1}{L} \sum_{i=1}^L \langle [(1 - G_{\nu\nu\uparrow}(\tau_i, \tau_i)) + (1 - G_{\nu\nu\downarrow}(\tau_i, \tau_i))] \rangle_{\{S_{i\nu}\}}. \quad (3.7)$$

Impurity magnetic correlation function is expressed by

$$\langle (M_\nu^z)^2 \rangle = \left\langle \left(d_{\nu\uparrow}^\dagger d_{\nu\uparrow} - d_{\nu\downarrow}^\dagger d_{\nu\downarrow} \right) \left(d_{\nu\uparrow}^\dagger d_{\nu\uparrow} - d_{\nu\downarrow}^\dagger d_{\nu\downarrow} \right) \right\rangle \quad (3.8)$$

$$= \left\langle \left(d_{\nu\uparrow}^\dagger d_{\nu\uparrow} - d_{\nu\downarrow}^\dagger d_{\nu\downarrow} \right) \left(d_{\nu\uparrow}^\dagger d_{\nu\uparrow} - d_{\nu\downarrow}^\dagger d_{\nu\downarrow} \right) \right\rangle + \left\langle \left(d_{\nu\uparrow} d_{\nu\uparrow}^\dagger d_{\nu\uparrow}^\dagger d_{\nu\uparrow} + d_{\nu\downarrow} d_{\nu\downarrow}^\dagger d_{\nu\downarrow}^\dagger d_{\nu\downarrow} \right) \right\rangle \quad (3.9)$$

$$= \frac{1}{L} \sum_{i=1}^L \langle [(G_{\nu\nu\uparrow}(\tau_i, \tau_i) - G_{\nu\nu\downarrow}(\tau_i, \tau_i))^2 + G_{\nu\nu\uparrow}(\tau_i, \tau_i) (1 - G_{\nu\nu\uparrow}(\tau_i, \tau_i)) + G_{\nu\nu\downarrow}(\tau_i, \tau_i) (1 - G_{\nu\nu\downarrow}(\tau_i, \tau_i))] \rangle_{\{S_{i\nu}\}}. \quad (3.10)$$

$\langle (M_\nu^z)^2 \rangle$ means the square of magnetic moment of 3d electrons:

$$(\mu_{eff,\nu}^z)^2 = \langle (M_\nu^z)^2 \rangle. \quad (3.11)$$

Total magnetic correlation function of impurity is

$$\langle (M^z)^2 \rangle = \left\langle \sum_{\nu=1}^5 (d_{\nu\uparrow}^\dagger d_{\nu\uparrow} - d_{\nu\downarrow}^\dagger d_{\nu\downarrow}) \sum_{\nu'=1}^5 (d_{\nu'\uparrow}^\dagger d_{\nu'\uparrow} - d_{\nu'\downarrow}^\dagger d_{\nu'\downarrow}) \right\rangle \quad (3.12)$$

$$= \left\langle \sum_{\nu=1}^5 \sum_{\nu'=1}^5 (d_{\nu\uparrow}^\dagger d_{\nu\uparrow} - d_{\nu\downarrow}^\dagger d_{\nu\downarrow}) (d_{\nu'\uparrow}^\dagger d_{\nu'\uparrow} - d_{\nu'\downarrow}^\dagger d_{\nu'\downarrow}) \right\rangle$$

$$+ \left\langle \sum_{\nu=1}^5 \sum_{\nu'=1}^5 (d_{\nu\uparrow} d_{\nu'\uparrow}^\dagger d_{\nu'\uparrow}^\dagger d_{\nu\uparrow} + d_{\nu\downarrow} d_{\nu'\downarrow}^\dagger d_{\nu'\downarrow}^\dagger d_{\nu\downarrow}) \right\rangle \quad (3.13)$$

$$= \frac{1}{L} \sum_{\nu=1}^5 \sum_{\nu'=1}^5 \sum_{i=1}^L \langle [(G_{\nu\nu\uparrow}(\tau_i, \tau_i) - G_{\nu\nu\downarrow}(\tau_i, \tau_i))$$

$$\times (G_{\nu'\nu'\uparrow}(\tau_i, \tau_i) - G_{\nu'\nu'\downarrow}(\tau_i, \tau_i))$$

$$+ G_{\nu\nu'\uparrow}(\tau_i, \tau_i) (\delta_{\nu\nu'} - G_{\nu'\nu\uparrow}(\tau_i, \tau_i))$$

$$+ G_{\nu\nu'\downarrow}(\tau_i, \tau_i) (\delta_{\nu\nu'} - G_{\nu'\nu\downarrow}(\tau_i, \tau_i))] \rangle_{\{S_{i\nu}\}}. \quad (3.14)$$

$\langle (M^z)^2 \rangle$ also means the square of total magnetic moment of 3d electrons:

$$(\mu_{eff}^z)^2 = \langle (M^z)^2 \rangle. \quad (3.15)$$

and the magnetic correlation functions between 3d orbitals are

$$\langle (M_\nu^z M_{\nu'}^z) \rangle = \left\langle (d_{\nu\uparrow}^\dagger d_{\nu\uparrow} - d_{\nu\downarrow}^\dagger d_{\nu\downarrow}) (d_{\nu'\uparrow}^\dagger d_{\nu'\uparrow} - d_{\nu'\downarrow}^\dagger d_{\nu'\downarrow}) \right\rangle \quad (3.16)$$

$$= \left\langle (d_{\nu\uparrow}^\dagger d_{\nu\uparrow} - d_{\nu\downarrow}^\dagger d_{\nu\downarrow}) (d_{\nu'\uparrow}^\dagger d_{\nu'\uparrow} - d_{\nu'\downarrow}^\dagger d_{\nu'\downarrow}) \right\rangle$$

$$+ \left\langle (d_{\nu\uparrow} d_{\nu'\uparrow}^\dagger d_{\nu'\uparrow}^\dagger d_{\nu\uparrow} + d_{\nu\downarrow} d_{\nu'\downarrow}^\dagger d_{\nu'\downarrow}^\dagger d_{\nu\downarrow}) \right\rangle \quad (3.17)$$

$$\begin{aligned}
&= \frac{1}{L} \sum_{i=1}^L \langle [(G_{\nu\nu\uparrow}(\tau_i, \tau_i) - G_{\nu\nu\downarrow}(\tau_i, \tau_i)) \\
&\quad \times (G_{\nu'\nu'\uparrow}(\tau_i, \tau_i) - G_{\nu'\nu'\downarrow}(\tau_i, \tau_i)) \\
&\quad + G_{\nu\nu'\uparrow}(\tau_i, \tau_i) (\delta_{\nu\nu'} - G_{\nu'\nu\uparrow}(\tau_i, \tau_i)) \\
&\quad + G_{\nu\nu'\downarrow}(\tau_i, \tau_i) (\delta_{\nu\nu'} - G_{\nu'\nu\downarrow}(\tau_i, \tau_i))] \rangle_{\{S_{l\nu}\}}. \tag{3.18}
\end{aligned}$$

In these equations, $\{S_{l\nu}\}$ indicates the Hubbard-Stratonovich field summation.

3.2. Dynamical Quantum Monte Carlo Measurements

After, static QMC measurements, total magnetic susceptibility $\chi(i\omega_m)$ and the magnetic susceptibilities between $3d$ orbitals $\chi_{\nu\nu'}(i\omega_m)$ were obtained.

Time ordered total magnetic susceptibility is

$$\chi(\tau) = \langle T_\tau m^z(\tau) m^z(0) \rangle. \tag{3.19}$$

By Fourier transformation, frequency-dependent susceptibility is calculated:

$$\chi(i\omega_m) = \int_0^\beta d\tau e^{i\omega_m\tau} \chi(\tau). \tag{3.20}$$

In experiment, the retarded magnetic susceptibility is measured and it is calculated by Kubo linear response theory:

$$\chi_{ret}(\omega) = -i \int_{-\infty}^{\infty} e^{i\omega t} \langle [m^z(t), m^z(0)] \rangle \theta(t) dt. \tag{3.21}$$

When the Matsubara frequency $i\omega_m$ and real frequency ω equal zero, the measured susceptibilities are same

$$\chi(i\omega_m = 0) = \chi_{ret}(\omega = 0). \tag{3.22}$$

Therefore, to compare the experimental results for magnetic susceptibility, zero-frequency magnetic susceptibilities were calculated.

$$\chi(i\omega_m = 0) = \int_0^\beta d\tau \chi(\tau). \quad (3.23)$$

In addition, the magnetic susceptibilities between $3d$ orbitals were obtained by the following equations

$$\chi_{\nu\nu'}(\tau) = \langle T_\tau m_\nu^z(\tau) m_{\nu'}^z(0) \rangle, \quad (3.24)$$

and by Fourier transformation,

$$\chi_{\nu\nu'}(i\omega_m = 0) = \int_0^\beta d\tau \chi_{\nu\nu'}(\tau). \quad (3.25)$$

CHAPTER 4

RESULTS FOR STATIC QUANTUM MONTE CARLO MEASUREMENTS

In this chapter, results for static QMC measurements will be represented. Firstly, occupations of Co $3d$ orbitals n_ν will be discussed and these measurements will be compared with DFT results. After that, semiconductor gap Δ of vitamin B₁₂ and its DFT results will be explained. Then, impurity magnetic correlation functions will be analyzed. From these magnetic correlation functions, effective magnetic moments of $3d$ electrons are calculated and their values will be compared with DFT results. Finally, results of total magnetic correlation function of $3d$ orbitals and correlations between these orbitals will be explained.

For QMC measurements, the onsite Coulomb interactions of impurities were set to $U = 4$ eV and $U = 8$ eV. These values are not the real values and to see the effect of Coulomb interaction, $U = 4$ eV and $U = 8$ eV were used in measurements.

4.1. Occupations of $3d$ Orbitals

By using Eq.3.7, the occupations of $3d$ orbitals are calculated and Figure 4.6 shows the occupations with respect to different temperature values for $U = 4$ eV. This graph shows that occupations of Co $3d$ orbitals do not change with changing in temperature. Furthermore, it has been found that the value of occupations are 1 or less than 1, which means that each $3d$ orbitals has 1 electron instead of 2 electrons. This is a very important result because Co has 7 $3d$ electrons, however; QMC measurements show that $3d$ orbitals have 5 electrons due to strong onsite Coulomb interactions. Moreover, the most occupied state is $3d_{3z^2-r^2}$ because it has the lowest energy and $3d_{xz}$ has the least occupations because it has the highest energy.

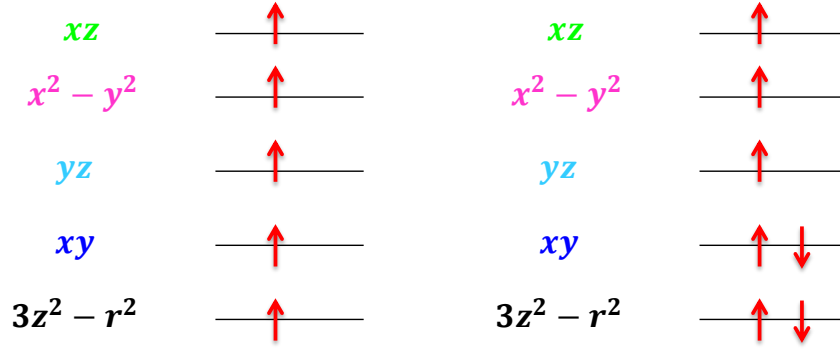


Figure 4.1. $3d$ orbitals from the QMC measurements and DFT measurements

4.1.1. Comparison of QMC Results and DFT Results for Occupations of $3d$ Orbitals

Table 4.1 indicates the comparison of QMC and DFT results for occupations of $3d$ orbitals. While occupation values are less than 1 in QMC results, they are approximately 2 in DFT results and this situation is shown in Fig.4.1. Furthermore, total electron number of Co $3d$ orbitals equals 4.5 with respect to QMC and it is obtained 7.2 from DFT. The reason of this situation is that DFT does not consider the onsite Coulomb interactions of $3d$ electrons and due to this reason, $3d$ orbitals are doubly-occupied.

Table 4.1. QMC, DFT and LSDA results for occupations of $3d$ orbitals.

ν	QMC ($U = 4$ eV)	QMC ($U = 8$ eV)	DFT	LSDA n_ν
$3z^2 - r^2$	1.02	0.97	1.81975	1.74869
xy	1.00	0.92	1.65561	1.65126
yz	0.91	0.77	1.44569	1.48235
$x^2 - y^2$	0.87	0.74	1.36078	1.39305
xz	0.74	0.72	0.98964	1.10553

4.2. Semiconductor Gap

To find the semiconductor gap Δ of vitamin B₁₂, the occupations of $3d$ orbitals were calculated for different chemical potentials. Figure 4.7-a and 4.7-b show the $\langle n_\nu \rangle$ vs μ for $U = 4$ eV at $T = 300$ K and $T = 600$ K, respectively. For $U = 8$ eV at $T = 300$ K and $T = 600$ K, $\langle n_\nu \rangle$ vs μ is discussed in Fig. 4.8-a and 4.8-b. Here, red solid lines show HOMO level and dash lines are LUMO level, and they were obtained from DFT calculations. Figure 4.7 and 4.8 indicate that in semiconductor gap, $\langle n_\nu \rangle$ changes and doubly occupied states which have $\epsilon_{d\nu} + U$ energy values are formed. This means that semiconductor gap which was obtained from QMC is less than DFT results due to hybridization between the impurity and host orbitals and onsite Coulomb interactions of $3d$ orbitals. As seen in Fig. 4.7a-b and 4.8a-b, the value of semiconductor gap do not change with changing in temperature both for $U = 4$ eV and $U = 8$ eV.

To see the effect of onsite Coulomb interactions on semiconductor gap, in Fig. 4.9, $\langle n_\nu \rangle$ vs μ is analyzed at $T = 300$ K for $U = 4$ eV and $U = 8$ eV, respectively. For $U = 4$ eV, doubly occupied states $\epsilon_{d\nu} + U$ have lower energy than for $U = 8$ eV case and so the value of semiconductor gap equals 0.4 eV for $U = 4$ eV and 1.6 eV for $U = 8$ eV. Moreover, to illustrate the differences between these two cases, electron density of $3d_{3z^2-r^2}$ is calculated as an example for $3d$ orbitals and it is shown in Fig. 4.10. To obtain ρ_ν , firstly, cubic spline of $\langle n_\nu \rangle$ vs μ was done and after that, the derivative of cubic spline with respect to energy ϵ was taken. These figures indicate more clearly doubly occupied states in semiconductor gap.

4.2.1. Comparison of QMC Results and DFT Results for Semiconductor Gap

In Table 4.2, QMC results and DFT results for semiconductor gap of vitamin B₁₂ are compared. In this table, it is seen that the results for QMC and DFT for semiconductor gap are very different because QMC uses the onsite Coulomb interactions of $3d$ orbitals exactly and hybridization between the impurity and host orbitals. Due to these parameters, doubly occupied states are formed in semiconductor gap and so QMC results for semiconductor gap is smaller than 2.71 eV.

Table 4.2. QMC, DFT and LSDA results for semiconductor gap Δ (eV).

	Semiconductor gap Δ (eV)
QMC ($U = 4$ eV)	0.4
QMC ($U = 8$ eV)	1.6
DFT	2.71325
LSDA α	1.9263
LSDA β	2.09365

4.3. Impurity Magnetic Correlation Functions

After the occupations of $3d$ orbitals, impurity magnetic correlation functions were calculated and $\langle (M_\nu^z)^2 \rangle$ vs temperature T are discussed in Fig. 4.11a. This figure shows that there is no significant changes in $\langle (M_\nu^z)^2 \rangle$ for different temperatures. In the previous part, $\langle n_\nu \rangle$ have been discussed and it has been said that each $3d$ orbitals have 1 electron instead of 2 electrons due to onsite impurity Coulomb interactions. Therefore, $\langle (M_\nu^z)^2 \rangle$ does not equal 0 because of single-occupancy of $3d$ orbitals.

By using impurity magnetic correlation functions, effective magnetic moments of $3d$ electrons $\mu_{eff,\nu}$ which is shown in Fig. 4.11b were calculated. In QMC measurements, $\mu_{eff,\nu}$ equals the square of $\langle (M_\nu^z)^2 \rangle$ and due to single-occupancy of $3d$ orbitals, their values are approximately 1.

In Fig. 4.12a-b and Fig. 4.13a-b, $\langle (M_\nu^z)^2 \rangle$ vs chemical potential μ is indicated for $U = 4$ eV and $U = 8$ eV at $T = 300$ K and $T = 600$ K. Again here, red solid lines show HOMO level and dash lines are LUMO level. From these figures, it is said that behaviour of impurity magnetic correlations functions for different chemical potentials is the same at $T = 300$ K and $T = 600$ K for both $U = 4$ eV and $U = 8$ eV. Moreover, $\langle (M_\nu^z)^2 \rangle$ vs μ shows doubly occupied states in semiconductor gap and due to these states, in semiconductor gap, values of $\langle (M_\nu^z)^2 \rangle$ decrease.

Fig. 4.13a-b indicate $\langle (M_\nu^z)^2 \rangle$ vs μ for $U = 4$ eV and $U = 8$ eV at $T = 300$ K. In semiconductor gap, decreases of values of $\langle (M_\nu^z)^2 \rangle$ are observed at higher energies for $U = 8$ eV so again, it is said that semiconductor gap is larger than for $U = 4$ eV case.

4.3.1. Comparison of QMC Results and DFT Results for Effective Magnetic Moment

Table 4.3 indicates the differences between the QMC and DFT results for effective magnetic moment of $3d$ electrons. QMC results for $\mu_{eff,\nu}$ are calculated by

$$(\mu_{eff}^T)^2 = \langle (M^z)^2 \rangle. \quad (4.1)$$

and DFT results for $\mu_{eff,\nu}$ are obtained from

$$\mu_{eff,\nu} = n_{\nu\uparrow} - n_{\nu\downarrow}. \quad (4.2)$$

Because DFT uses the onsite Coulomb interactions of impurity electrons as an approximation, it gives that $3d$ orbitals are doubly-occupied. Therefore, $\mu_{eff,\nu}$ equals 0 ; however, QMC measurements say that $\mu_{eff,\nu}$ are approximately 1 due to single-occupancy of impurity orbitals.

Table 4.3. QMC, DFT and LSDA results for magnetic moment of $3d$ electrons.

ν	QMC ($U = 4$ eV)	QMC ($U = 8$ eV)	LSDA
$3z^2 - r^2$	0.94	0.97	0.02090
xy	0.91	0.93	0.03594
yz	0.87	0.85	0.00883
$x^2 - y^2$	0.84	0.83	0.01245
xz	0.78	0.82	0.00229

4.4. Total Impurity Magnetic Correlation Function

In this part of the static QMC results, total impurity magnetic correlation function $\langle (M^z)^2 \rangle$ is analyzed. Fig. 4.15a-b shows the $\langle (M^z)^2 \rangle$ vs temperature T and total effective magnetic moment μ_{eff}^T vs T for $U = 4$ eV.

In Fig. 4.15a, dash line indicates the sum of impurity magnetic correlation functions which are

$$\sum_{\nu=1}^5 \langle (M_{\nu}^z)^2 \rangle. \quad (4.3)$$

It is known from the previous part that $\langle (M_{\nu}^z)^2 \rangle$ does not change with temperature, however; $\langle (M^z)^2 \rangle$ are affected by changes in temperature, which means that inter-orbital magnetic correlation function $\langle M_{\nu}^z M_{\nu'}^z \rangle$ are temperature dependent. Moreover, in Fig 4.15a, total magnetic correlation function of $3d$ orbitals increase at high temperatures and decrease at low temperatures.

To explain this situation, μ_{eff}^T was calculated by

$$(\mu_{eff}^T)^2 = \langle (M_{\nu}^z)^2 \rangle \quad (4.4)$$

and μ_{eff}^T vs T is discussed in Fig. 4.15b. These QMC results indicate that at high temperatures, correlations between the $3d$ orbitals are ferromagnetic (FM) and they are anti-ferromagnetic (AFM) at low temperatures. In other words, $3d$ electrons have high spin state at high temperatures and they have low spin states at low temperatures. For example, one possible visualization of high spin state and low spin state of Co $3d^5$ orbitals can be Fig. 4.2. In Fig. 4.2, the left one shows the high spin state at high temperatures



Figure 4.2. High spin state and low spin state of Co $3d^5$.

and all correlations are FM between the $3d$ electrons. The right one represents the low spin state at low temperatures and AFM correlations are seen between some $3d$ electrons. Therefore, at low temperatures, $\langle (M^z)^2 \rangle$ and μ_{eff}^T decrease.

Fig. 4.16a-b shows the comparison of $\langle (M^z)^2 \rangle$ vs T and $\langle M_\nu^z M_{\nu'}^z \rangle$ between the $3z^2 - r^2$ and xy orbitals vs T . Here, $3z^2 - r^2$ and xy orbitals was chosen as an example for inter-orbital magnetic correlations and it is observed that these orbitals have the most negative correlations. In Fig.4.16b, at high temperatures, magnetic correlations between the $3z^2 - r^2$ and xy orbitals are FM and at low temperatures, they are AFM as in the 4.16a. From inter-orbital correlations of $3z^2 - r^2$ and xy , what happens at high and low temperatures is seen more clearly.

It is the most important point that at $T = 600$ K, we have big error bars and it is focused in Fig. 4.3. For this temperature value, 10 simulations were performed and

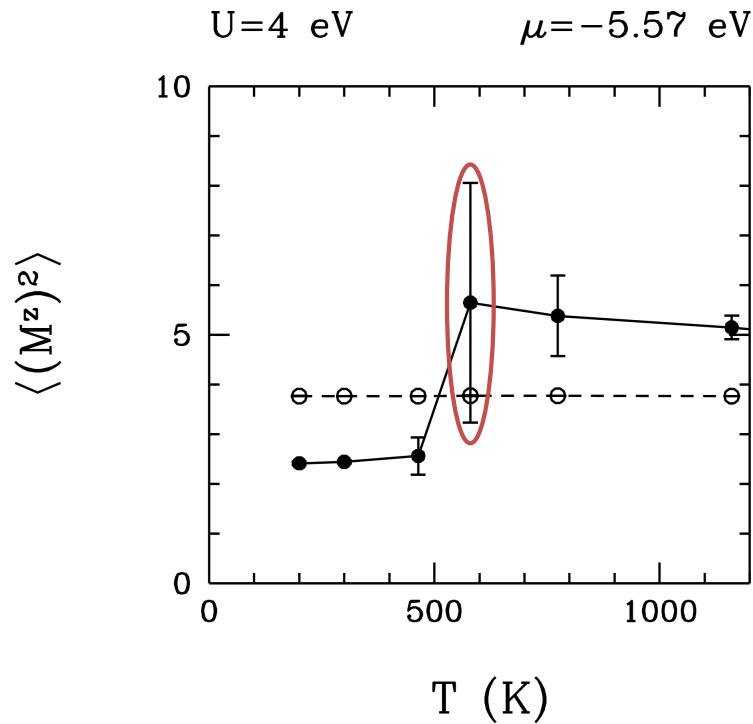


Figure 4.3. Total magnetic correlations of $3d$ orbitals $\langle (M^z)^2 \rangle$ vs temperature T .

each of them had 50.000 measurement sweeps. As seen in Fig. 4.4, the results of these simulations for $\langle (M^z)^2 \rangle$ fluctuate between 2 and 9 and the possible explanation of this situation can be as the following:

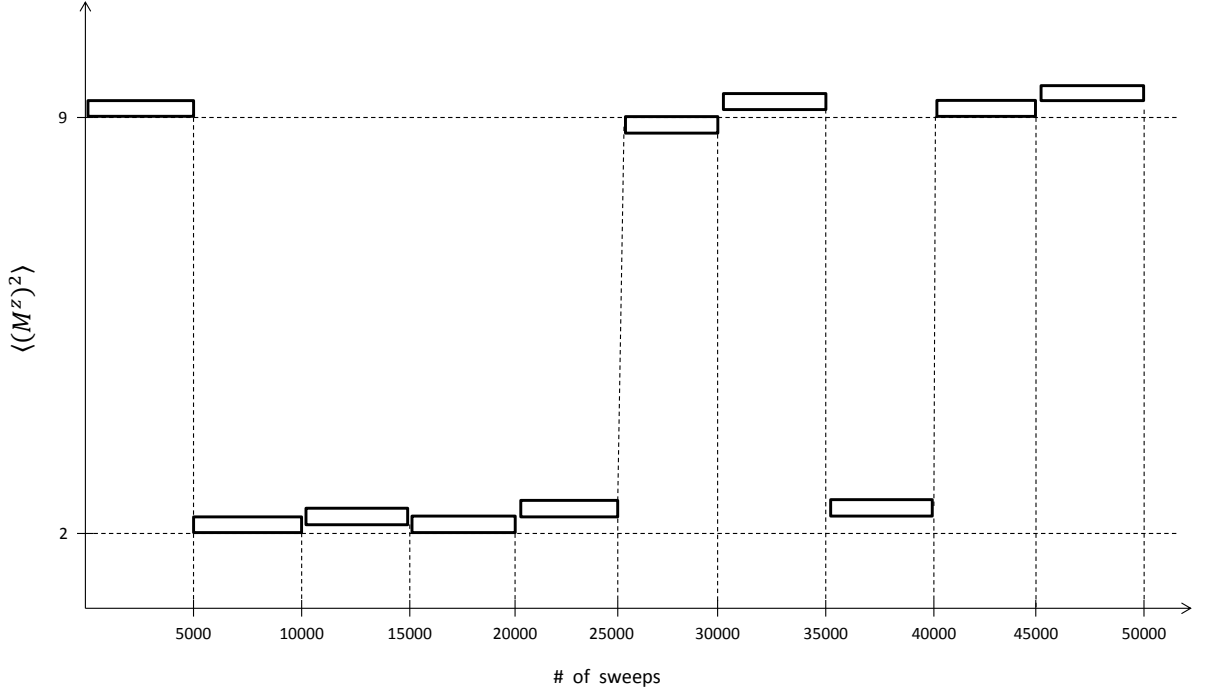


Figure 4.4. Measurements at $T = 600$ K for $\langle (M^z)^2 \rangle$.

When $\langle (M^z)^2 \rangle$ are 9, $\mu_{eff}^T = 3$ and when $\langle (M^z)^2 \rangle$ are 2, $\mu_{eff}^T = 1.7$. If $\mu_{eff}^T = 3$ case is defined as high spin state, $\mu_{eff}^T = 1.7$ case can be low spin state and this situation is shown in Fig. 4.5. While the left picture in Fig. 4.5 defines the high spin state and $\mu_{eff}^T = 3$ case, the right one indicates the low spin state and $\mu_{eff}^T = 1.7$ case. The QMC measurements are fluctuate between these values at $T = 600$ K because at this temperature, the energies of high spin state and low spin state can be close each other.

After that, to see the all magnetic correlations between the Co $3d$ orbitals, $\langle M_\nu^z M_{\nu'}^z \rangle$ was calculated and these results are discussed with respect to $3d$ orbitals ν in Fig. 4.17 at $T = 300$ K and $T = 1550$ K, respectively. As being expressed, at $T = 300$ K, AFM correlations are seen between the $3d$ orbitals and all correlations are FM at $T = 1550$ K.

Up to now, all results have shown total impurity magnetic correlation function and inter-orbital correlation functions for $U = 4$ eV case. To see the effect of onsite Coulomb interactions of $3d$ orbitals, same measurements were made for $U = 8$ eV.

Fig. 4.18a-b show $\langle (M^z)^2 \rangle$ vs T and $\langle M_\nu^z M_{\nu'}^z \rangle$ between the $3z^2 - r^2$ and xy orbitals vs T . Similar to $U = 4$ eV case, at high temperatures, total magnetic correlations are FM and at low temperatures, AFM correlations exist between the $3d$ orbitals. The most important differences between the $U = 4$ eV and $U = 8$ eV is that fluctuation

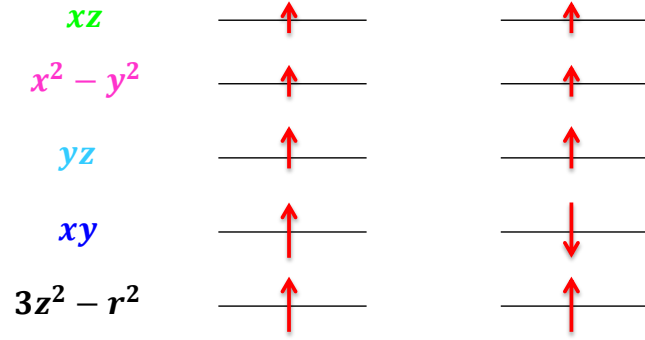


Figure 4.5. Spin states for $\mu_{eff}^T = 3$ and spin states for $\mu_{eff}^T = 1.7$.

between the high spin state and low spin state is seen at $T = 300$ K for $U = 8$ eV. Again, the most negative correlations were observed between the $3z^2 - r^2$ and xy orbitals and Fig. 4.18b indicates that the behaviour of correlations between these orbitals specifies total impurity correlation function for different temperatures.

In Fig. 4.19a-b, inter-orbital magnetic correlation functions are discussed at $T = 300$ K and $T = 1550$ K. At $T = 300$ K, AFM correlations exist but what happens at lower temperatures is very important for $U = 8$ eV. Because, in contrast to $U = 4$ eV case, fluctuation between the high and low spin states are observed at $T = 300$ K and so it is estimated that AFM correlations can be seen at below the 300 K for $U = 8$ eV. At $T = 1550$ K, all correlations are FM as $U = 4$ eV.

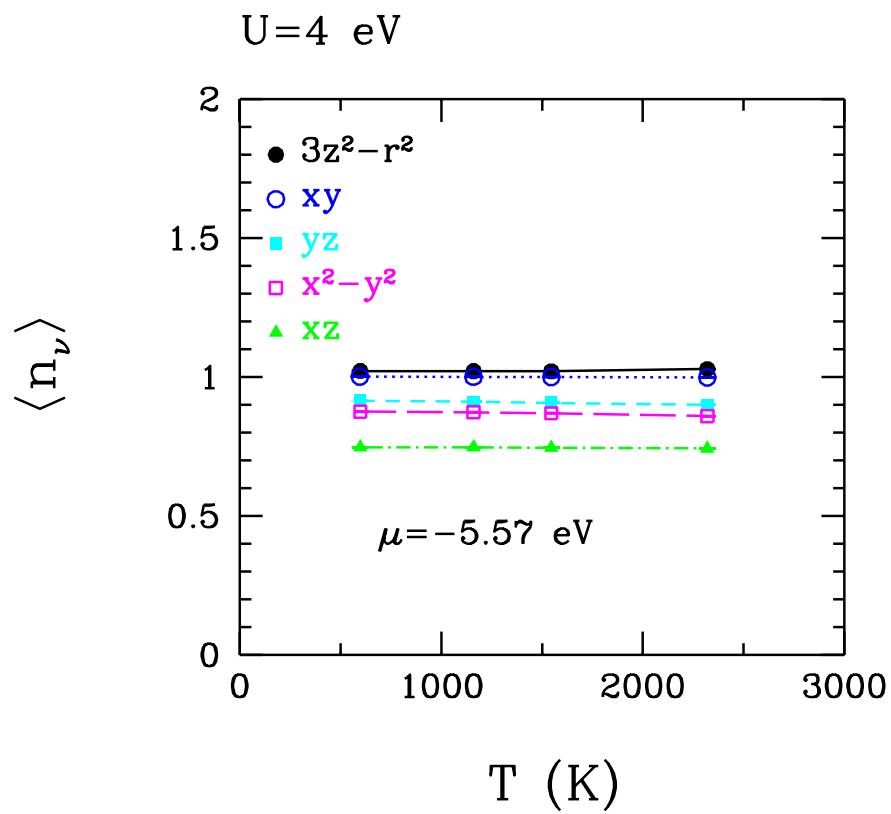


Figure 4.6. Onsite Coulomb interaction of 3d orbitals $U = 4$ eV. Occupations of 3d orbitals $\langle n_\nu \rangle$ vs T .

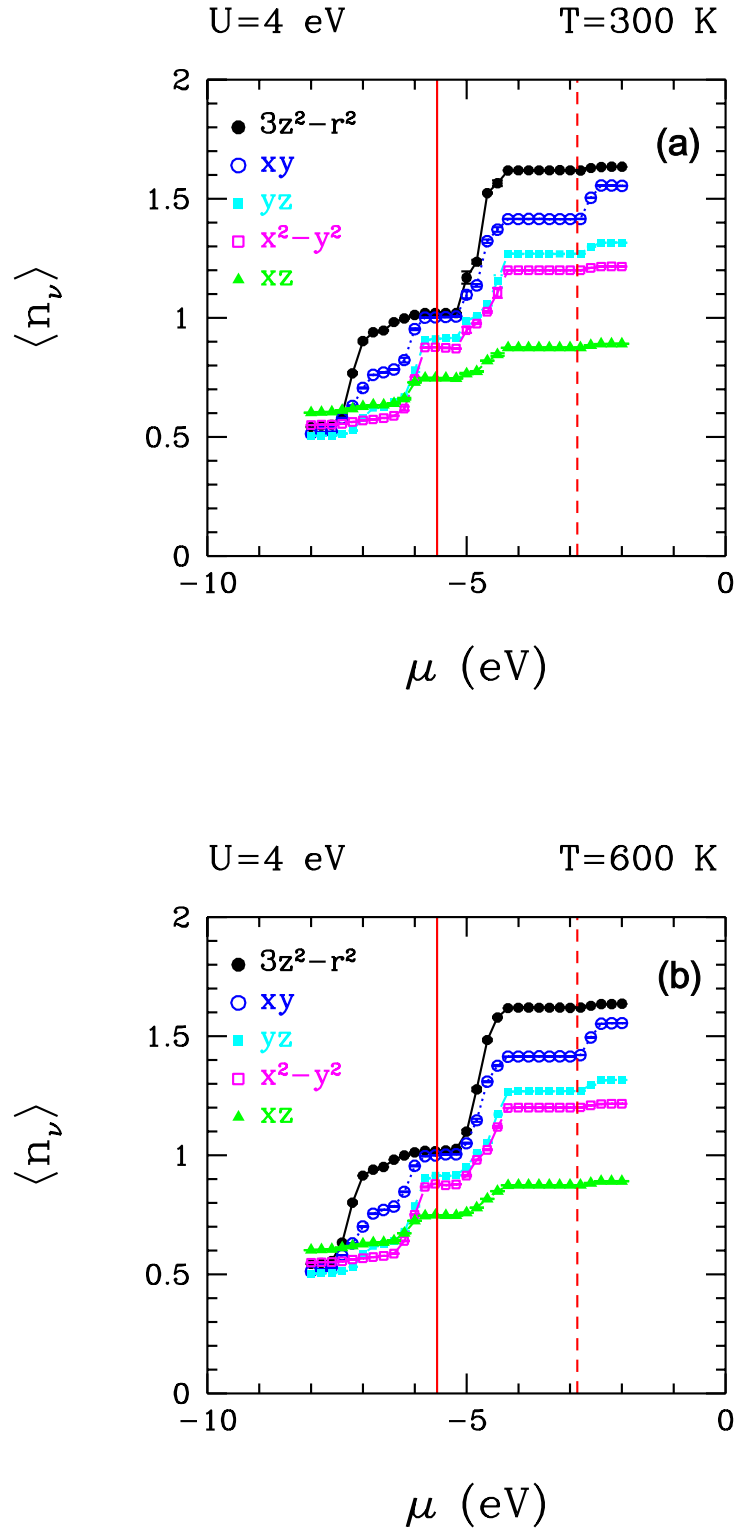


Figure 4.7. Onsite Coulomb interaction of $3d$ orbitals $U = 4$ eV. Red solid line shows HOMO and red dash line shows LUMO. (a) Occupations of $3d$ orbitals $\langle n_\nu \rangle$ vs μ at temperature $T = 300$ K. (b) Occupations of $3d$ orbitals $\langle n_\nu \rangle$ vs μ at temperature $T = 600$ K.

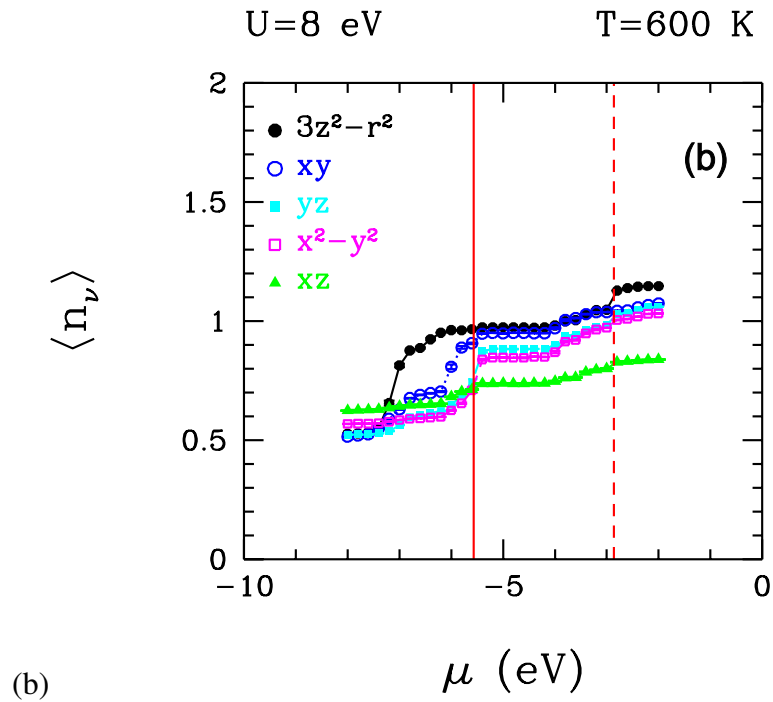
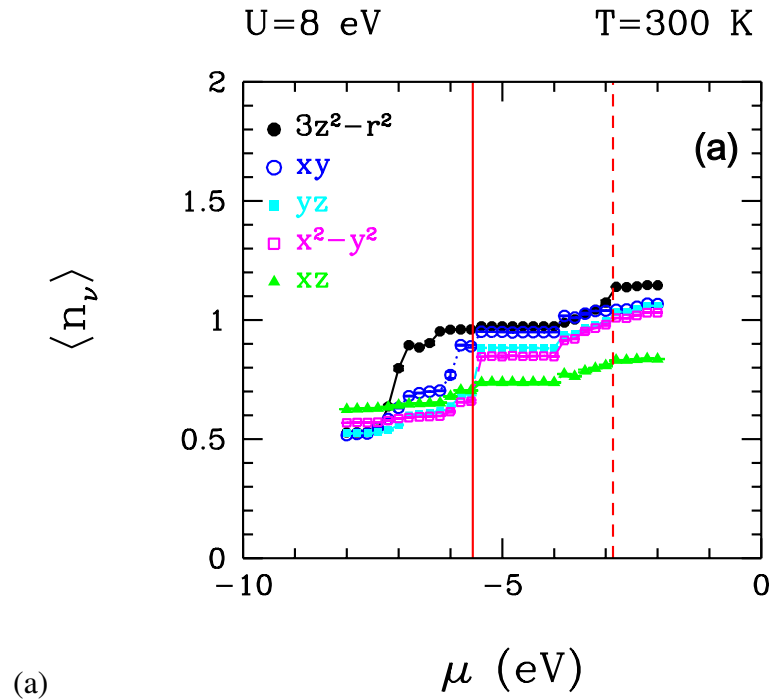


Figure 4.8. Onsite Coulomb interaction of 3d orbitals $U = 8$ eV. Red solid line shows HOMO and red dash line shows LUMO. (a) Occupations of 3d orbitals $\langle n_\nu \rangle$ vs μ at temperature $T = 300$ K. (b) Occupations of 3d orbitals $\langle n_\nu \rangle$ vs μ at temperature $T = 600$ K.

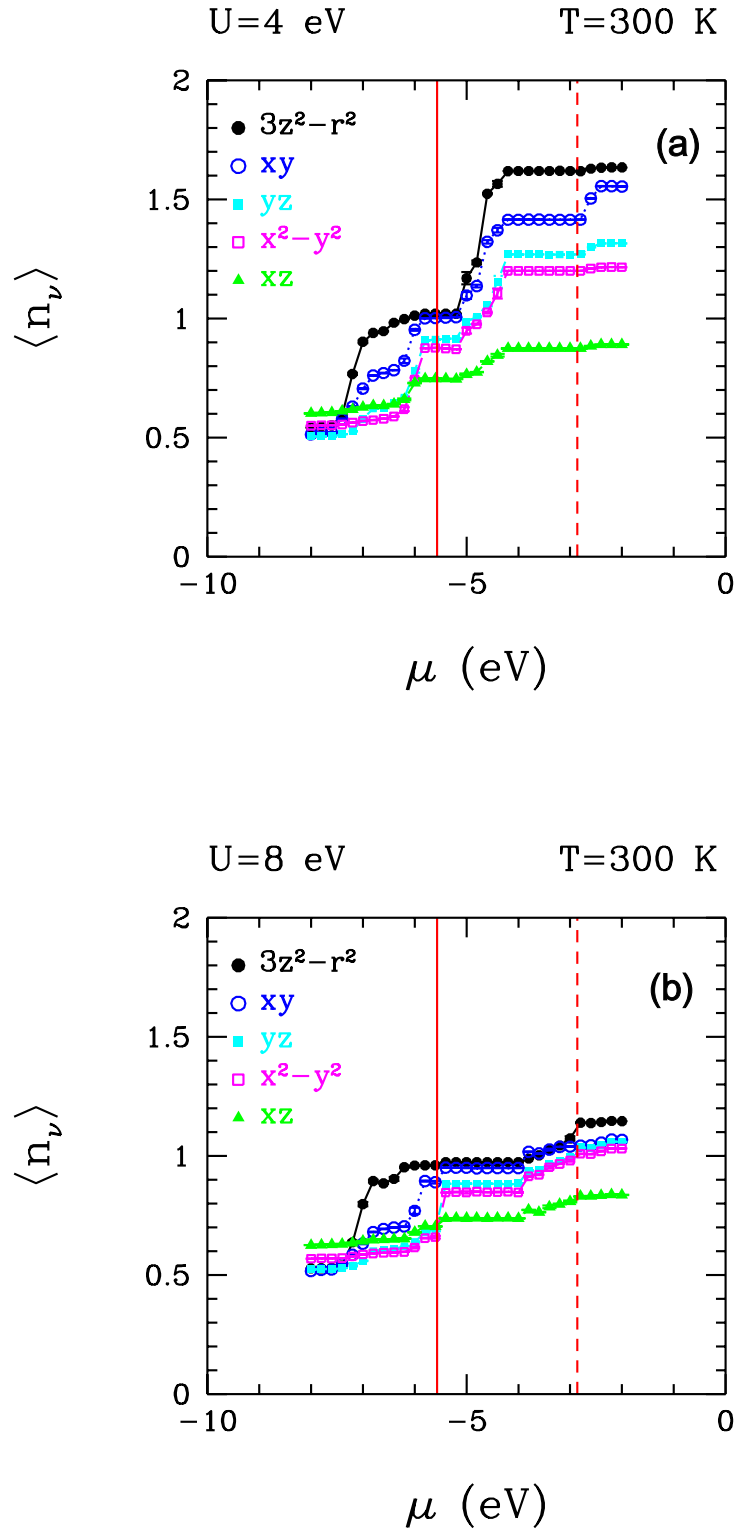


Figure 4.9. Red solid line shows HOMO and red dash line shows LUMO. (a) Onsite Coulomb interaction of $3d$ orbitals $U = 4$ eV and occupations of $3d$ orbitals $\langle n_\nu \rangle$ vs μ at temperature $T = 300$ K. (b) Onsite Coulomb interaction of $3d$ orbitals $U = 8$ eV and occupations of $3d$ orbitals $\langle n_\nu \rangle$ vs μ at temperature $T = 300$ K.

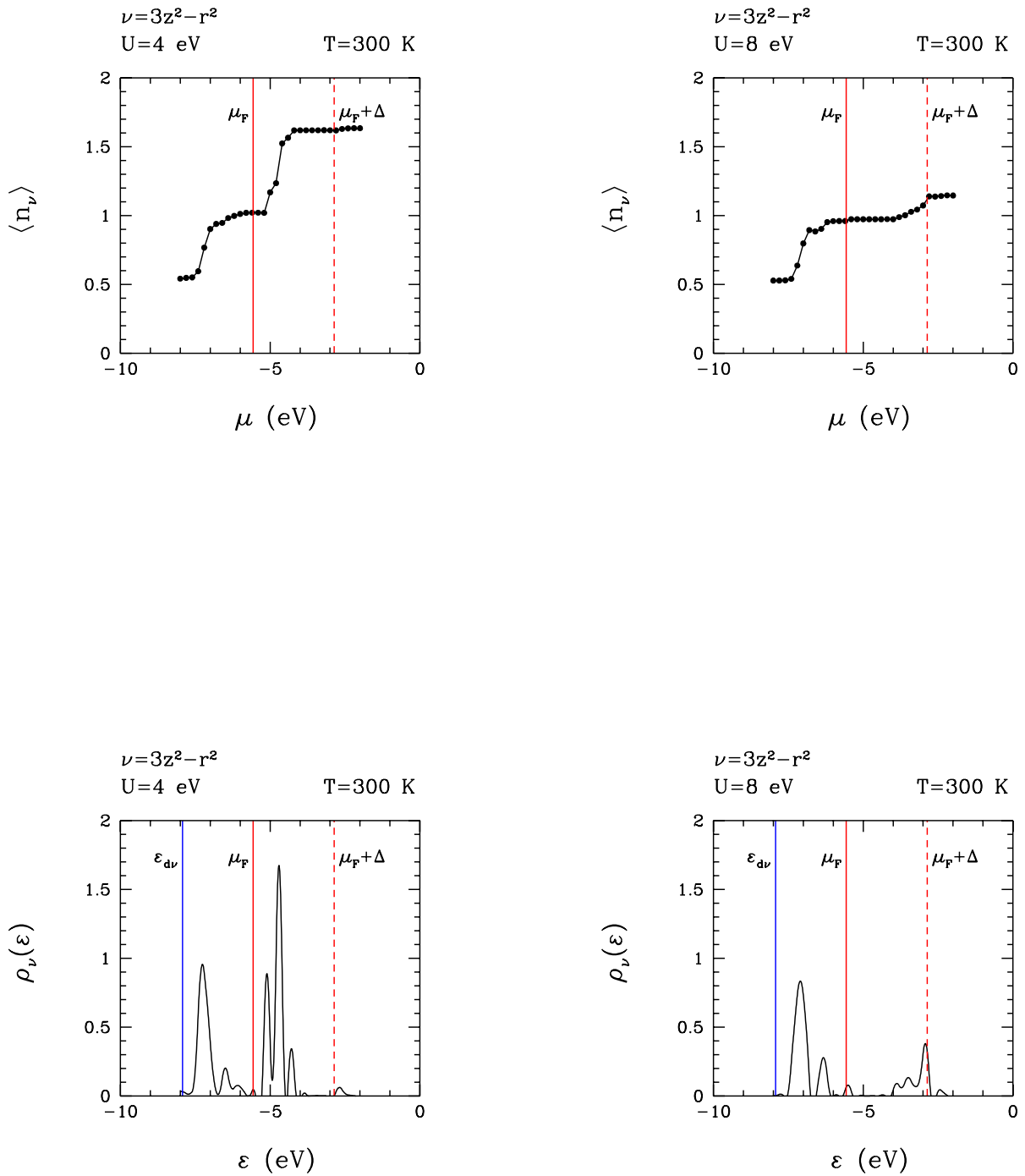


Figure 4.10. Red solid line shows HOMO and red dash line shows LUMO. Blue solid line is energy level of $3z^2 - r^2$. For $3z^2 - r^2$ orbital, $\langle n_\nu \rangle$ vs μ at temperature $T = 300$ K for $U = 4$ eV and $U = 8$ eV and $\rho_\nu(\varepsilon)$ vs ε at temperature $T = 300$ K for $U = 4$ eV and $U = 8$ eV.

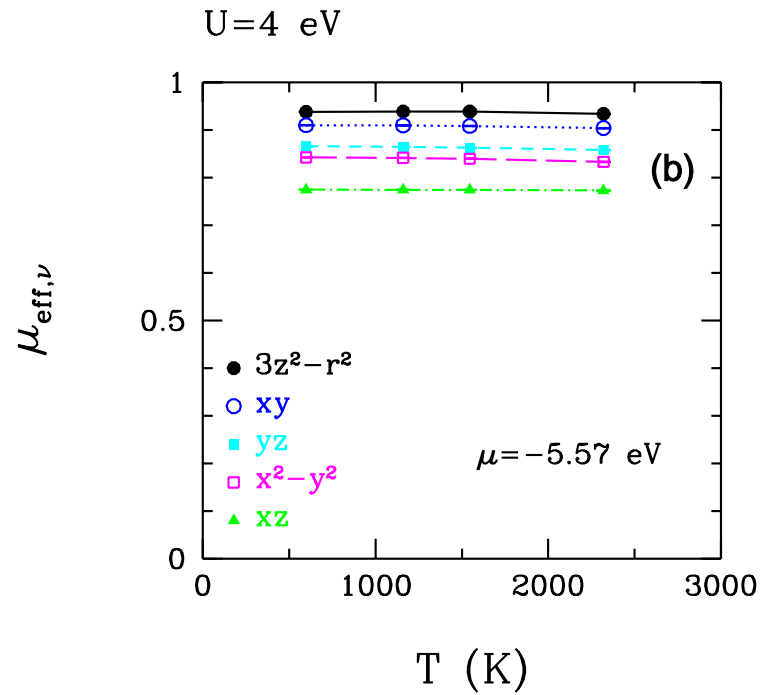
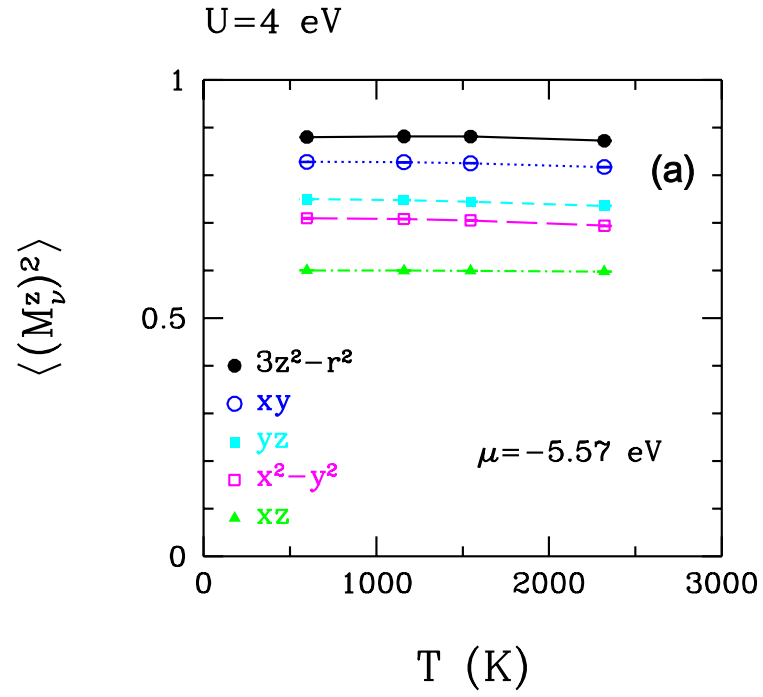


Figure 4.11. Onsite Coulomb interaction $U = 4$ eV. (a) Impurity magnetic correlation function $\langle (M_{\nu}^z)^2 \rangle$ vs temperature T . (b) Impurity effective magnetic moment $\mu_{eff,\nu}$ vs temperature T .

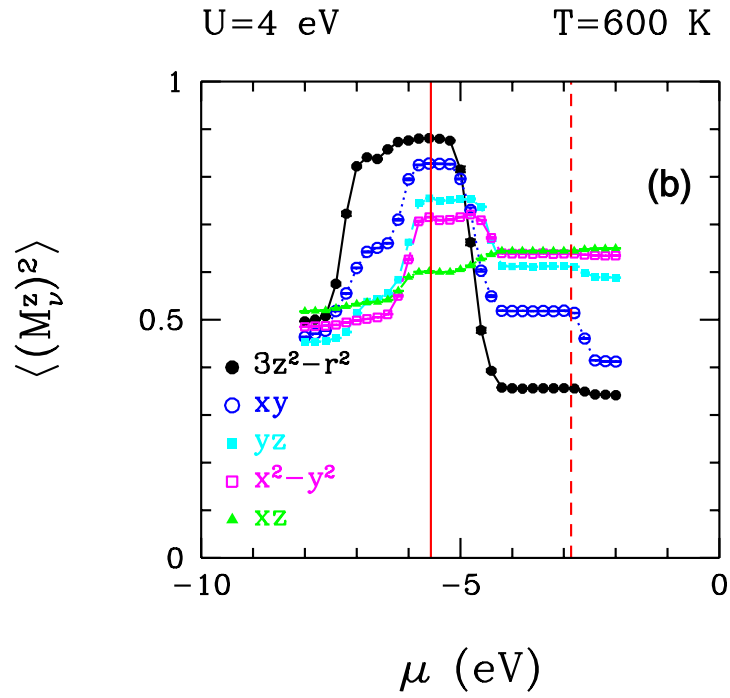
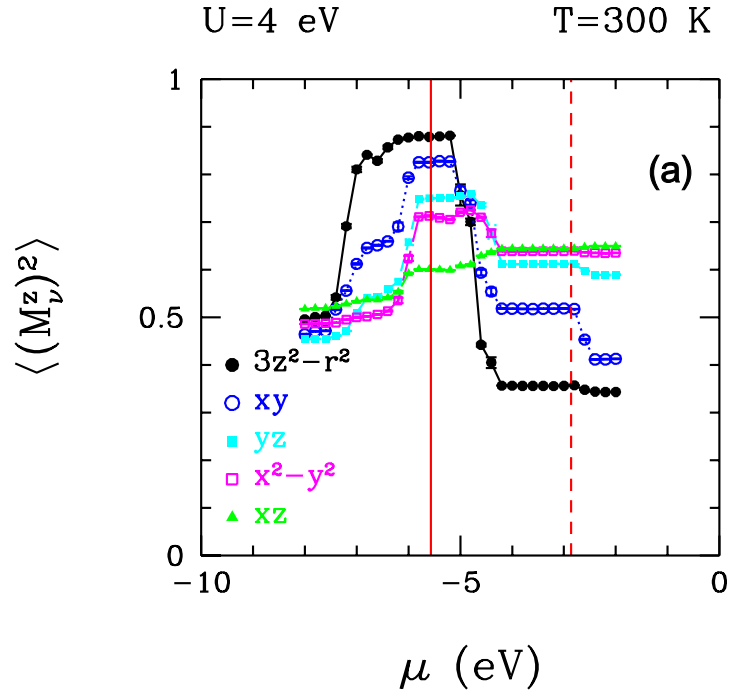


Figure 4.12. Onsite Coulomb interaction $U = 4$ eV. Red solid line shows HOMO and red dash line shows LUMO. (a) Impurity magnetic correlation function $\langle (M_\nu^z)^2 \rangle$ vs μ at temperature $T = 300$ K. (b) Impurity magnetic correlation function $\langle (M_\nu^z)^2 \rangle$ vs μ at temperature $T = 600$ K.

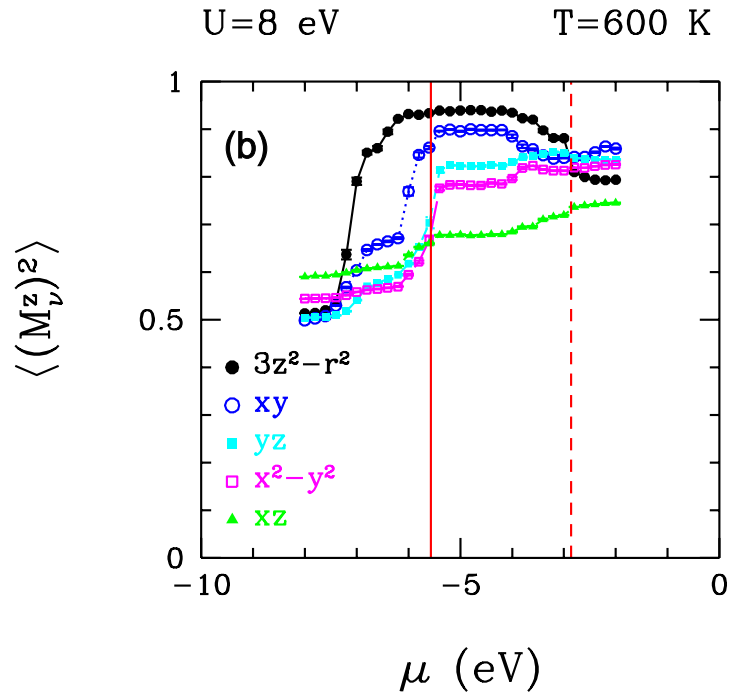
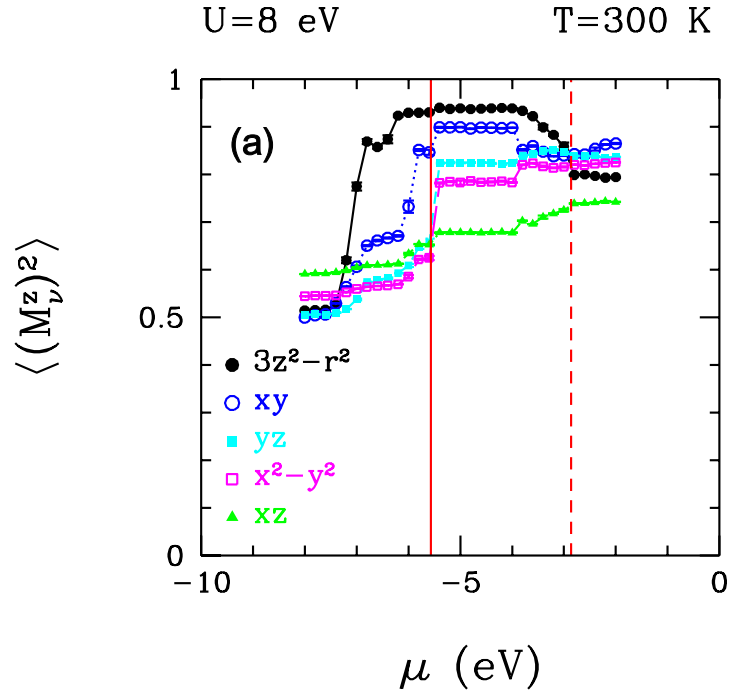


Figure 4.13. Onsite Coulomb interaction $U = 8$ eV. Red solid line shows HOMO and red dash line shows LUMO. (a) Impurity magnetic correlation function $\langle (M_\nu^z)^2 \rangle$ vs μ at temperature $T = 300$ K. (b) Impurity magnetic correlation function $\langle (M_\nu^z)^2 \rangle$ vs μ at temperature $T = 600$ K.

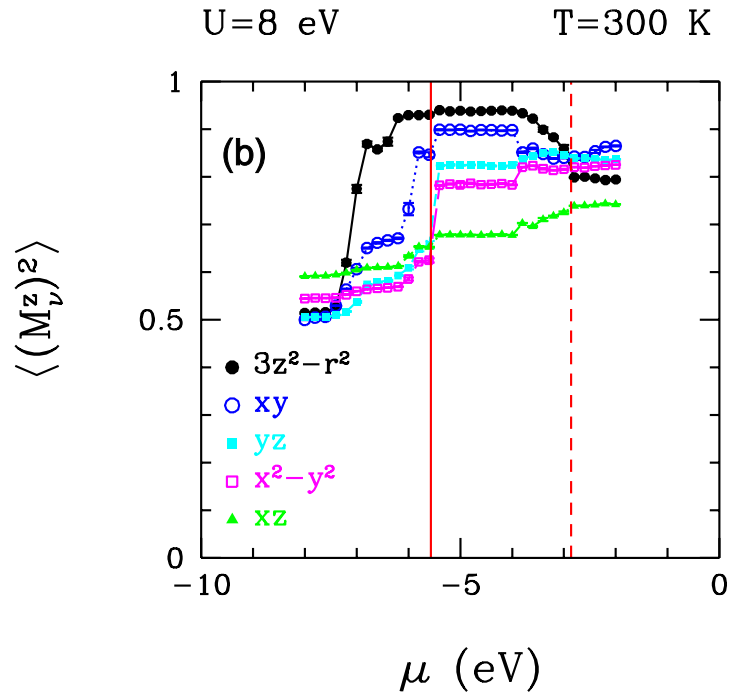
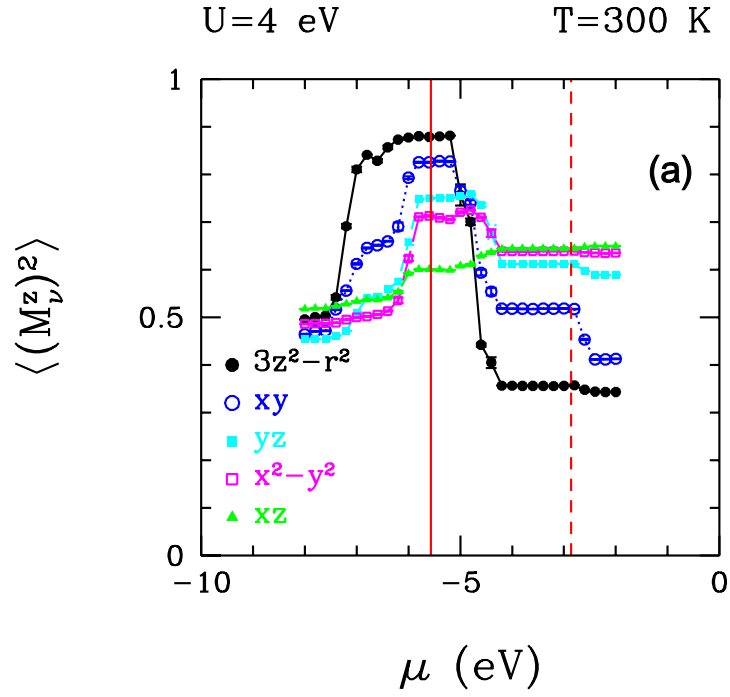


Figure 4.14. Temperature $T = 300$ K. Red solid line shows HOMO and red dash line shows LUMO. (a) Impurity magnetic correlation function $\langle (M_v^z)^2 \rangle$ vs μ for onsite Coulomb interaction $U = 4$ eV. (b) Impurity magnetic correlation function $\langle (M_v^z)^2 \rangle$ vs μ for onsite Coulomb interaction $U = 8$ eV.

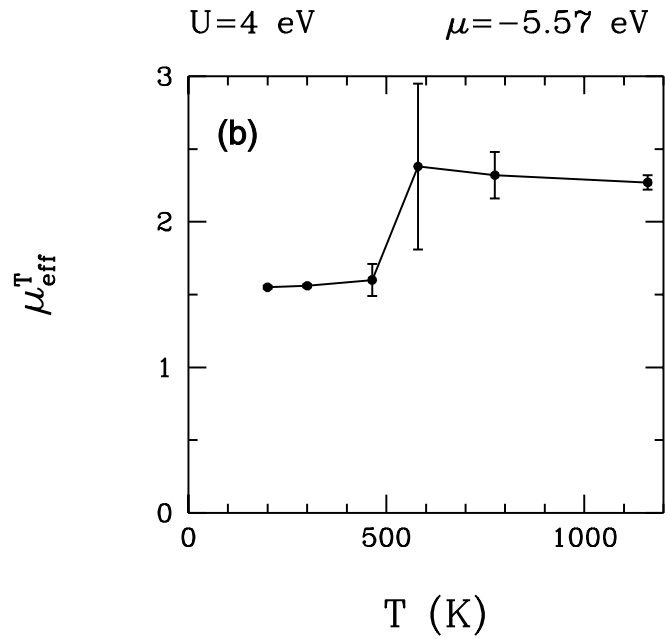
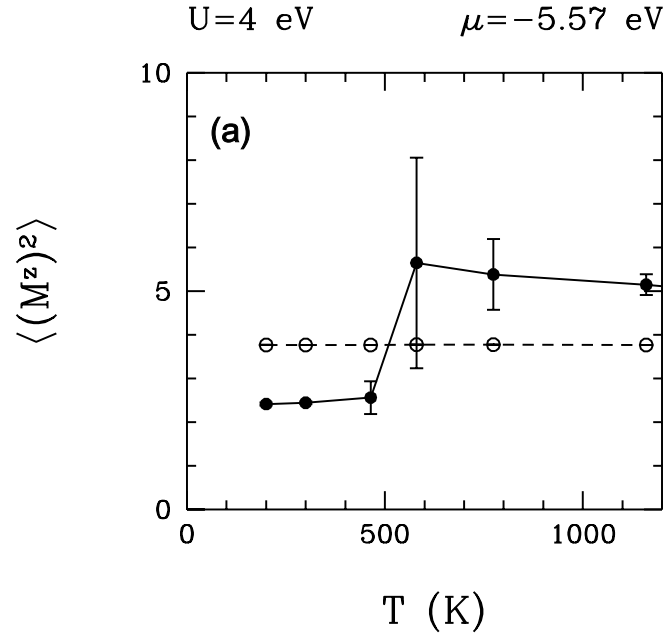


Figure 4.15. Number of warmup and measurement sweeps are shown as $N \times (\text{warmup} + \text{measurements})$. N is the number of simulations. For $T = 200$ K $14 \times (1k + 1k)$, $T = 300$ K $9 \times (5k + 10k)$, $T = 460$ K $10 \times (1k + 16k)$, $T = 600$ K $32 \times (10k + 50k)$, $T = 770$ K $10 \times (10k + 480k)$, $T = 1160$ K $40 \times (1k + 80k)$. (a) Total impurity magnetic correlation function of Co $3d$ $\langle (M^z)^2 \rangle$ vs temperature T . Dash line shows the $\sum_{\nu=1}^5 \langle (M_{\nu}^z)^2 \rangle$. (b) Total effective magnetic moment of Co $3d$ electrons μ_{eff}^T vs temperature T .

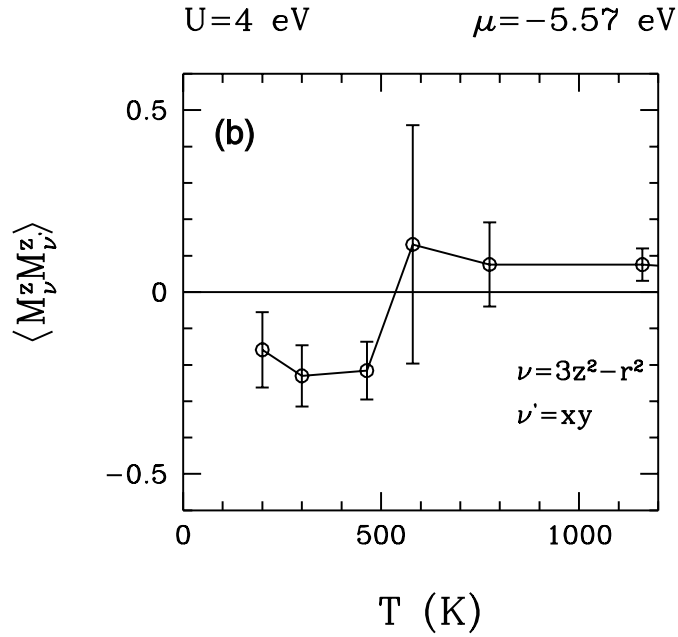
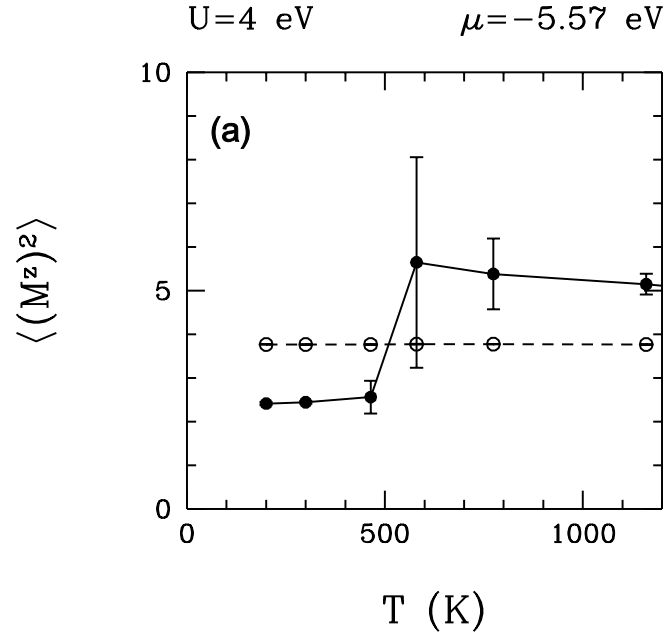


Figure 4.16. Number of warmup and measurement sweeps are shown as $N \times (\text{warmup} + \text{measurements})$. N is the number of simulations. For $T = 200$ K $14 \times (1k+1k)$, $T = 300$ K $9 \times (5k+10k)$, $T = 460$ K $10 \times (1k+16k)$, $T = 600$ K $32 \times (10k + 50k)$, $T = 770$ K $10 \times (10k + 480k)$, $T = 1160$ K $40 \times (1k + 80k)$. (a) Total impurity magnetic correlation function $\langle (M^z)^2 \rangle$ vs temperature T . Dash line shows the $\sum_{\nu=1}^5 \langle (M_\nu^z)^2 \rangle$. (b) Magnetic correlation function $\langle M_\nu^z M_{\nu'}^z \rangle$ between the $3z^2 - r^2$ and xy orbitals vs temperature T .

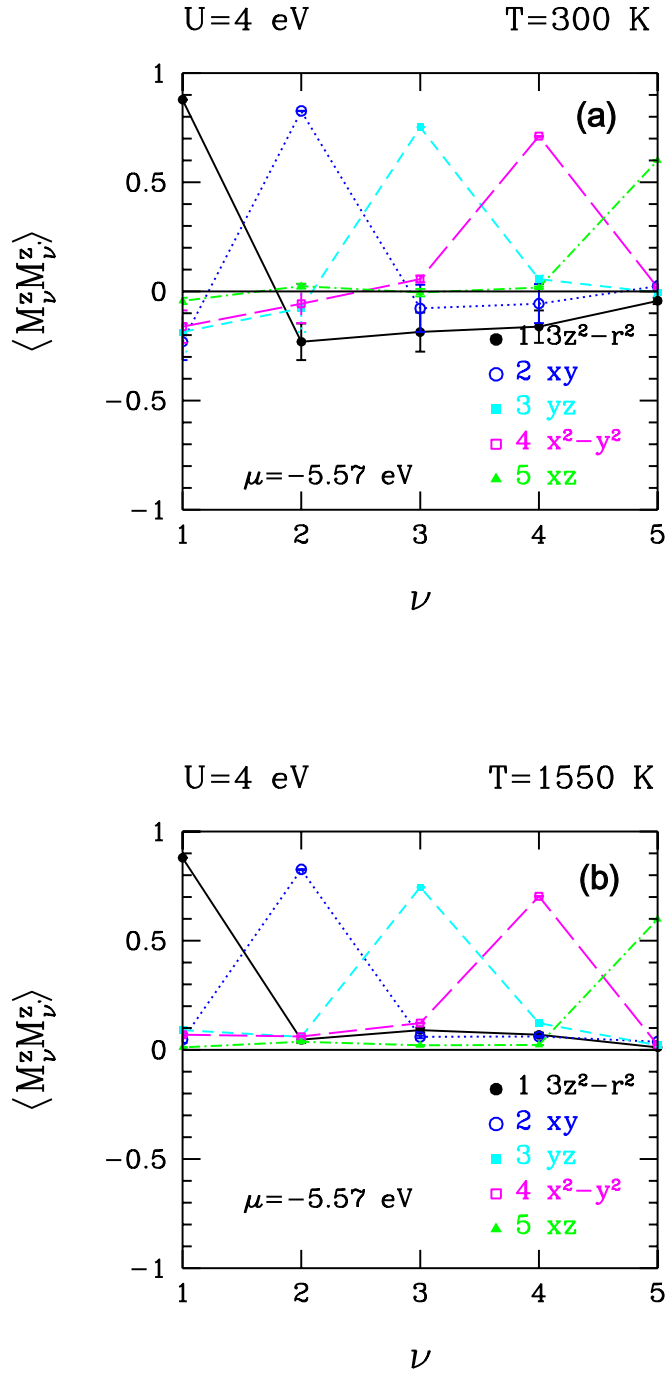


Figure 4.17. Onsite Coulomb interaction $U = 4$ eV. Number of warmup and measurement sweeps are shown as $N \times (\text{warmup} + \text{measurements})$. N is the number of simulations. For $T = 300$ K $9 \times (5k + 10k)$, $T = 1550$ K $(1k + 60k)$. (a) Magnetic correlation function $\langle M_\nu^z M_{\nu'}^z \rangle$ between the $3d$ orbitals vs $3d$ orbitals ν at temperature $T = 300$ K. (b) Magnetic correlation function $\langle M_\nu^z M_{\nu'}^z \rangle$ between the $3d$ orbitals vs $3d$ orbitals ν at temperature $T = 1550$ K.

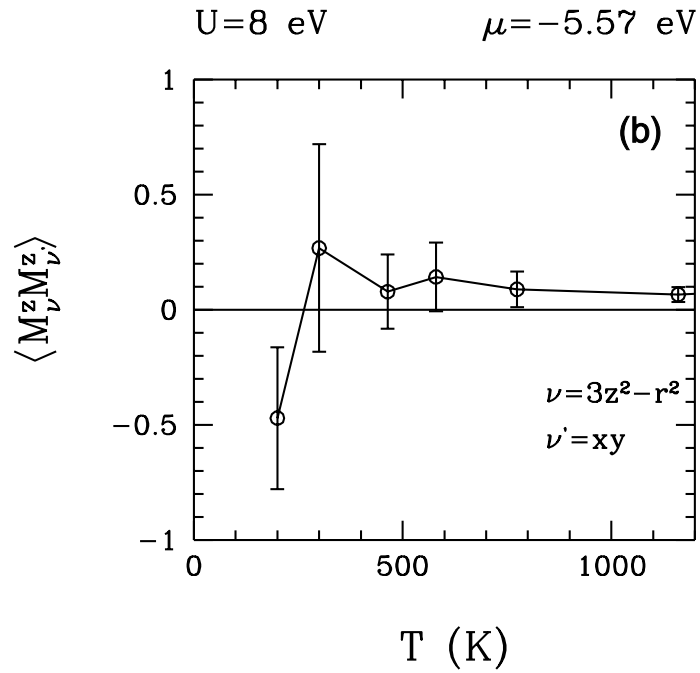
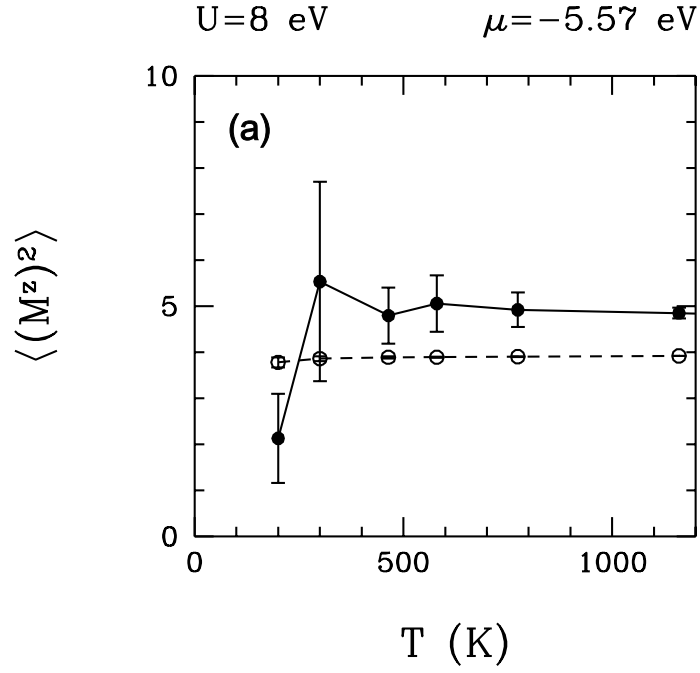


Figure 4.18. Number of warmup and measurement sweeps are shown as $N \times (\text{warmup} + \text{measurements})$. N is the number of simulations. For $T = 200$ K $10 \times (1k+1k)$, $T = 300$ K $10 \times (5k+10k)$, $T = 460$ K $6 \times (5k+80k)$, $T = 600$ K $10 \times (10k + 50k)$, $T = 770$ K $10 \times (10k + 480k)$, $T = 1160$ K $10 \times (1k + 80k)$. (a) Total impurity magnetic correlation function $\langle (M^z)^2 \rangle$ vs temperature T . Dash line shows the $\sum_{\nu=1}^5 \langle (M_\nu^z)^2 \rangle$. (b) Magnetic correlation function $\langle M_\nu^z M_{\nu'}^z \rangle$ between the $3z^2 - r^2$ and xy orbitals vs temperature T .

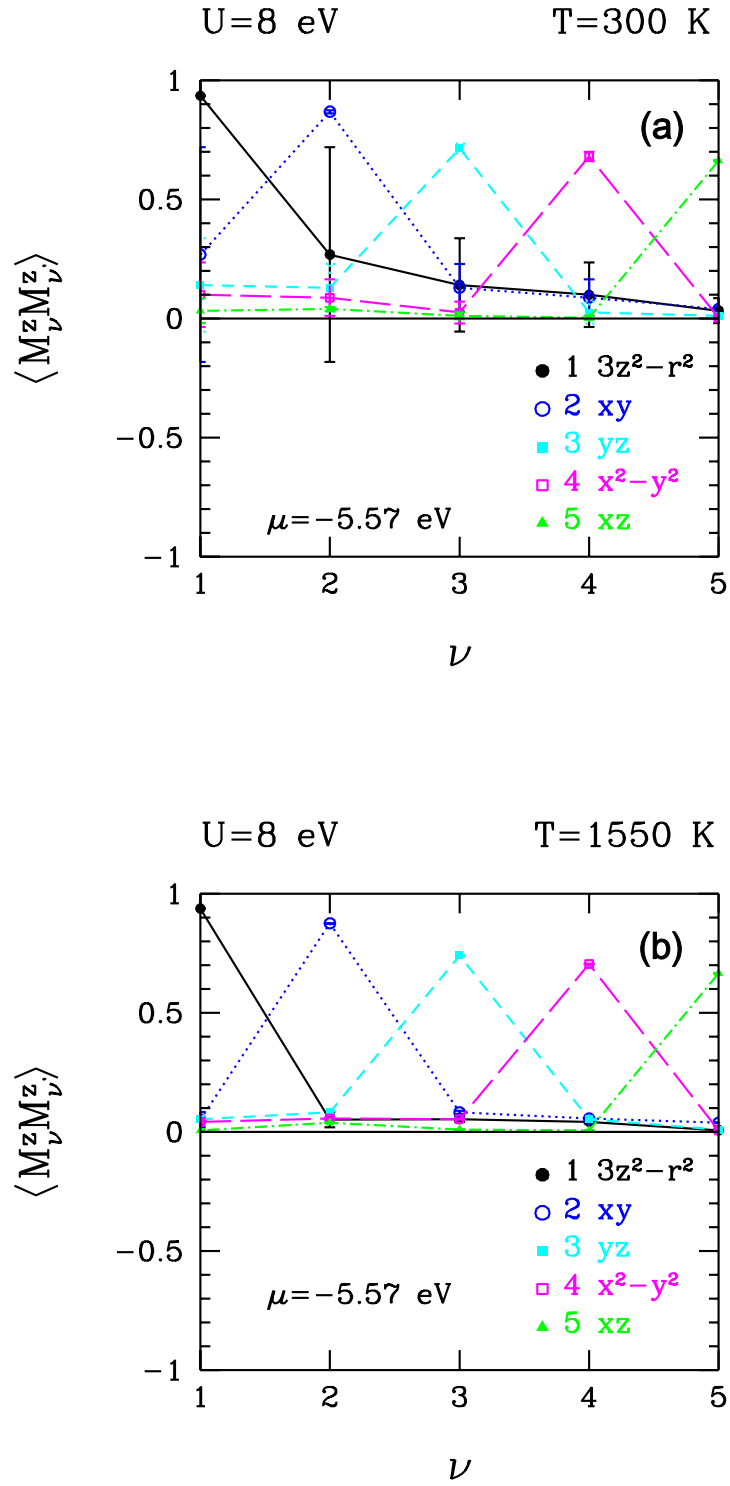


Figure 4.19. Onsite Coulomb interaction $U = 8$ eV. Number of warmup and measurement sweeps are shown as $N \times (\text{warmup} + \text{measurements})$. N is the number of simulations. For $T = 300$ K $10 \times (5k + 10k)$, $T = 1550$ K $(1k + 40k)$. (a) Magnetic correlation function $\langle M_\nu^z M_{\nu'}^z \rangle$ between the $3d$ orbitals vs $3d$ orbitals ν at temperature $T = 300$ K. (b) Magnetic correlation function $\langle M_\nu^z M_{\nu'}^z \rangle$ between the $3d$ orbitals vs $3d$ orbitals ν at temperature $T = 1550$ K.

CHAPTER 5

RESULTS FOR DYNAMICAL QUANTUM MONTE CARLO MEASUREMENTS

In this chapter, results for dynamical QMC measurements are discussed. By using Eq. 3.23, total magnetic susceptibility of Co $3d$ orbitals are calculated. After that, Eq. 3.25 is used to obtain magnetic susceptibilities between the $3d$ orbitals. This calculations were performed to interpret magnetic properties of impurity orbitals in detail.

In figures of magnetic susceptibilities, the red dash lines indicate the magnetic susceptibility of single-free electron and the solid red lines define the total magnetic susceptibility of 5 non-interacting electrons. These susceptibilities are calculated by using Curie Law which describes the magnetization of paramagnets:

$$\chi = \frac{C}{T}. \quad (5.1)$$

Here, C shows the Curie constant and T is the temperature. Curie constant is written as

$$C = \frac{Ng^2\mu_B^2S(S+1)}{3k_B}. \quad (5.2)$$

N is the electron number, g is the Lande constant, μ_B shows the Bohr magneton, S is the spin states and k_B is the Boltzmann constant. To calculate the magnetic susceptibility of non-interacting electrons:

$$g = 2 \quad (5.3)$$

$$S = \frac{1}{2} \quad (5.4)$$

and $N = 1$ for single particle and $N = 5$ for 5 non-interacting particles. Magnetic susceptibilities of single particle and 5 non-interacting particles were calculated to explain total magnetic susceptibility of $3d$ orbitals and magnetic susceptibilities between them.

Fig. 5.1 shows the total magnetic susceptibility of Co $3d$ orbitals $\chi(i\omega_m = 0)$

vs temperature T . Between $T = 1500$ K and $T = 800$ K, $3d$ electrons behave like 5 non-interacting electrons, however; between the $T = 800$ K and $T = 450$ K, $\chi(i\omega_m = 0)$ decreases unlike the total susceptibility of 5 non-interacting electrons. This situation indicates that between these temperature values, interactions are seen between the $3d$ electrons and they are AFM because of decreasing in $\chi(i\omega_m = 0)$. After that, at lower temperatures, Co $3d$ electrons behave like single electron, which means that between 4 $3d$ electrons, AFM correlations exist and they cancel each other. Therefore, below the $T = 600$ K, total susceptibility of $3d$ electrons are similar with the Curie temperature type susceptibility of single-free electron.

Fig.5.2, 5.3 and 5.4 indicate the magnetic susceptibilities between the $3d$ electrons. It is seen that susceptibilities between the $3z^2 - r^2$ and the other orbitals are the strongest and at low temperatures $\chi_{\nu\nu'}(i\omega_m = 0)$ between the xy , yz , $x^2 - y^2$ and xz are very small.

To see the magnetic susceptibility for different onsite $3d$ Coulomb interactions, QMC measurements for $U = 8$ eV were done and for this case, in Fig.5.5, the total magnetic susceptibility of Co $3d$ orbitals $\chi(i\omega_m = 0)$ vs temperature T is discussed. Here, Co $3d$ electrons behave like 5 non-interacting electrons and measurements at lower temperature values must be done to understand effect of Coulomb interactions much better.

Similar to $U = 4$ eV case, fig.5.6, 5.7 and 5.8 indicate the magnetic susceptibilities between the $3d$ electrons for $U = 8$ eV. It is seen that susceptibilities between the $3z^2 - r^2$ and the other orbitals are the strongest and at low temperatures $\chi_{\nu\nu'}(i\omega_m = 0)$ between the xy , yz , $x^2 - y^2$ and xz are very small.

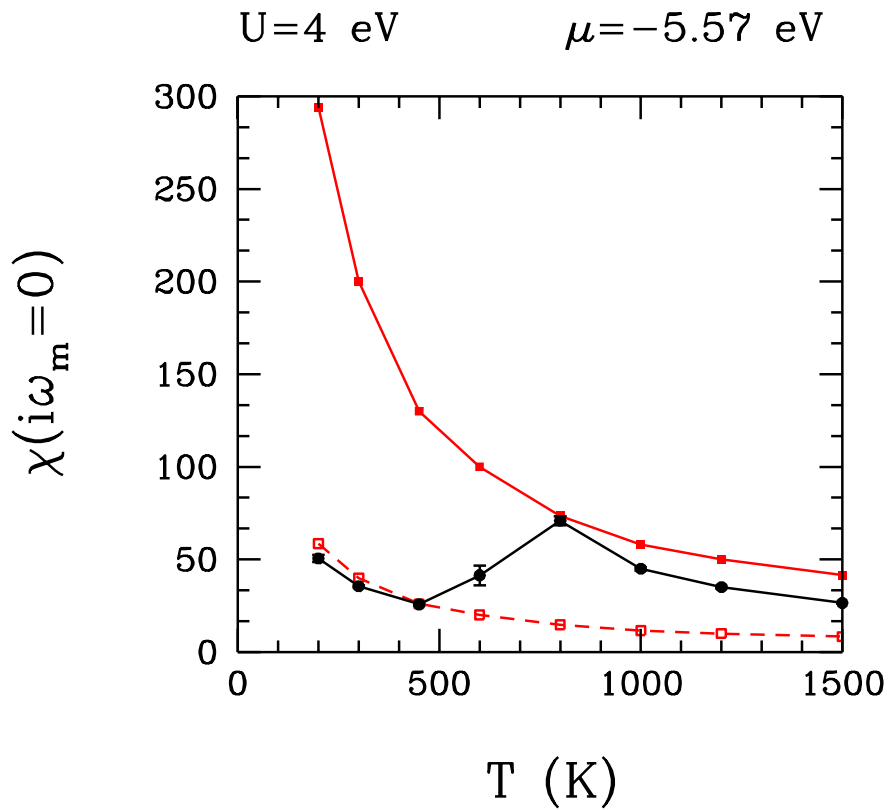


Figure 5.1. Number of warmup and measurement sweeps are shown as (warmup + measurements). For $T = 200 \text{ K}$ ($1k+1k$), $T = 300 \text{ K}$ ($5k+10k$), $T = 450 \text{ K}$ ($5k+10k$), $T = 600 \text{ K}$ ($5k+80k$), $T = 800 \text{ K}$ ($10k+100k$), $T = 1000 \text{ K}$, ($5k+80k$) $T = 1200 \text{ K}$ ($5k+80k$), $T = 1500$ ($5k+80k$). Red solid line shows magnetic susceptibility of 5 free spin. Red dash line shows magnetic susceptibility of 1 free spin. Black solid line is total magnetic susceptibility $\chi(i\omega_m = 0)$ vs temperature T .

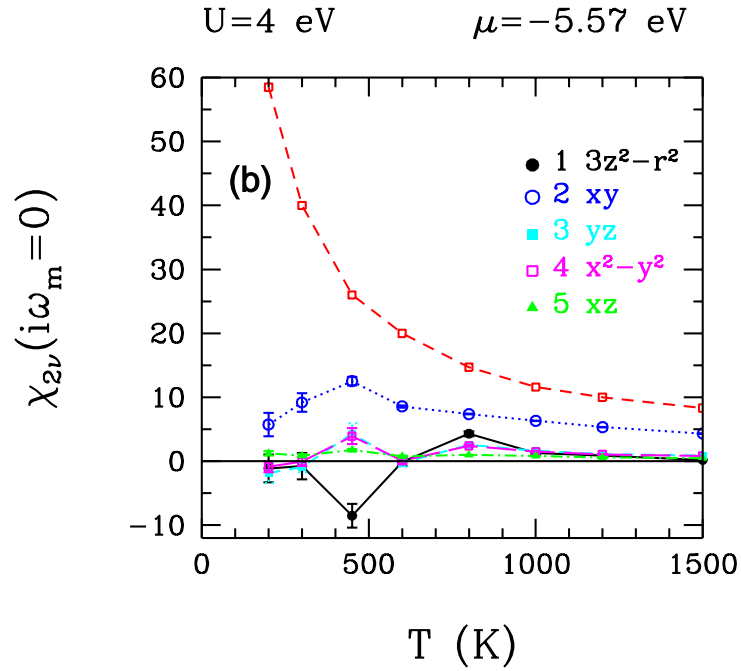
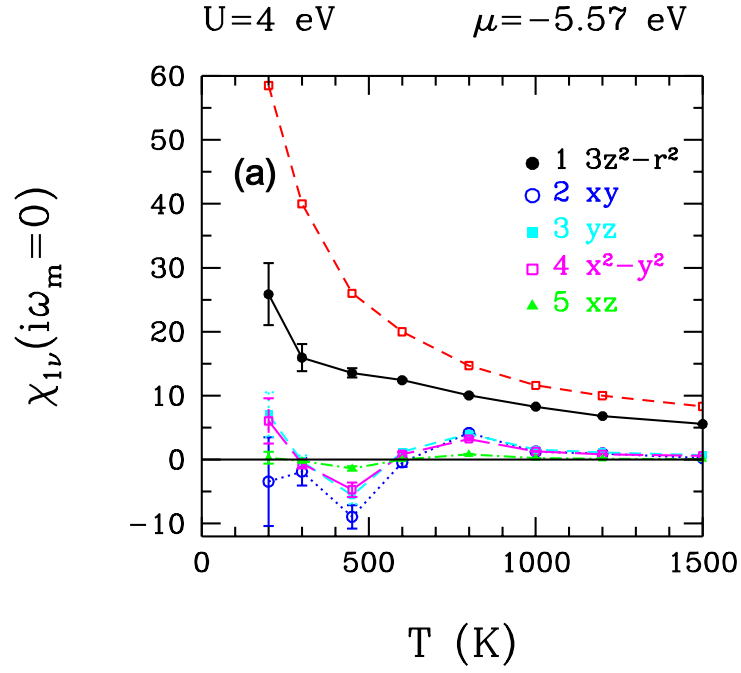


Figure 5.2. Number of warmup and measurement sweeps are shown as (warmup + measurements). For $T = 200$ K ($1k + 1k$), $T = 300$ K ($5k + 10k$), $T = 450$ K ($5k + 10k$), $T = 600$ K ($5k + 80k$), $T = 800$ K ($10k + 100k$), $T = 1000$ K, ($5k + 80k$) $T = 1200$ K ($5k + 80k$), $T = 1500$ K ($5k + 80k$). Red dash line shows magnetic susceptibility of 1 free spin. (a) Magnetic susceptibility between $3z^2 - r^2$ and the other Co $3d$ orbitals $\chi_{1\nu}(i\omega_m = 0)$ vs temperature T . (b) Magnetic susceptibility between xy and the other Co $3d$ orbitals $\chi_{2\nu}(i\omega_m = 0)$ vs temperature T

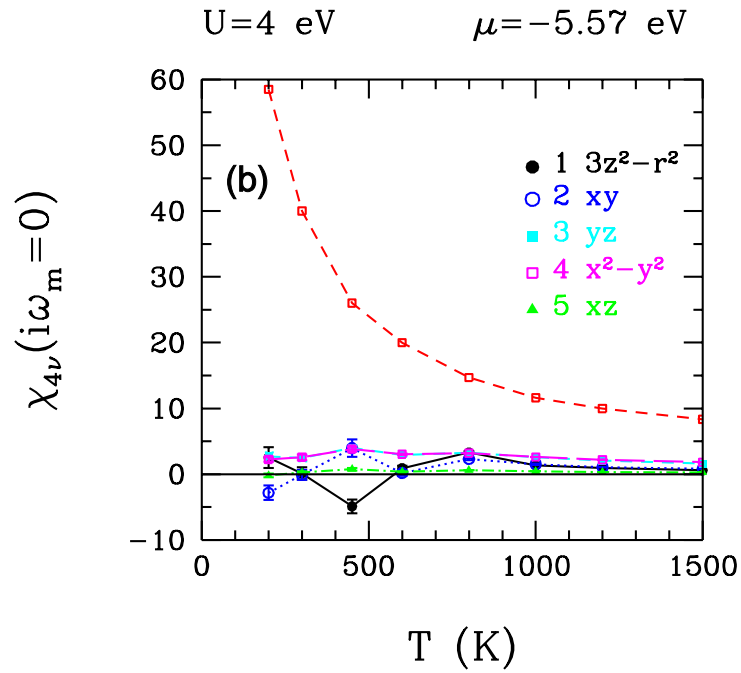
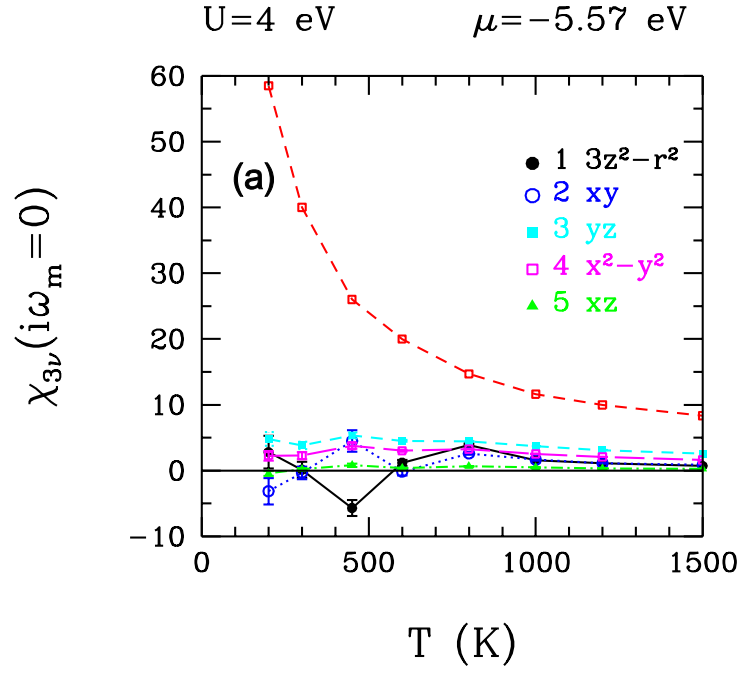


Figure 5.3. Number of warmup and measurement sweeps are shown as (warmup + measurements) . For $T = 200$ K ($1k + 1k$), $T = 300$ K ($5k + 10k$), $T = 450$ K ($5k + 10k$), $T = 600$ K ($5k + 80k$), $T = 800$ K ($10k + 100k$), $T = 1000$ K, ($5k + 80k$) $T = 1200$ K ($5k + 80k$), $T = 1500$ K ($5k + 80k$). Red dash line shows magnetic susceptibility of 1 free spin. (a) Magnetic susceptibility between yz and the other Co $3d$ orbitals $\chi_{3\nu}(i\omega_m = 0)$ vs temperature T . (b) Magnetic susceptibility between $x^2 - y^2$ and the other Co $3d$ orbitals $\chi_{4\nu}(i\omega_m = 0)$ vs temperature T .

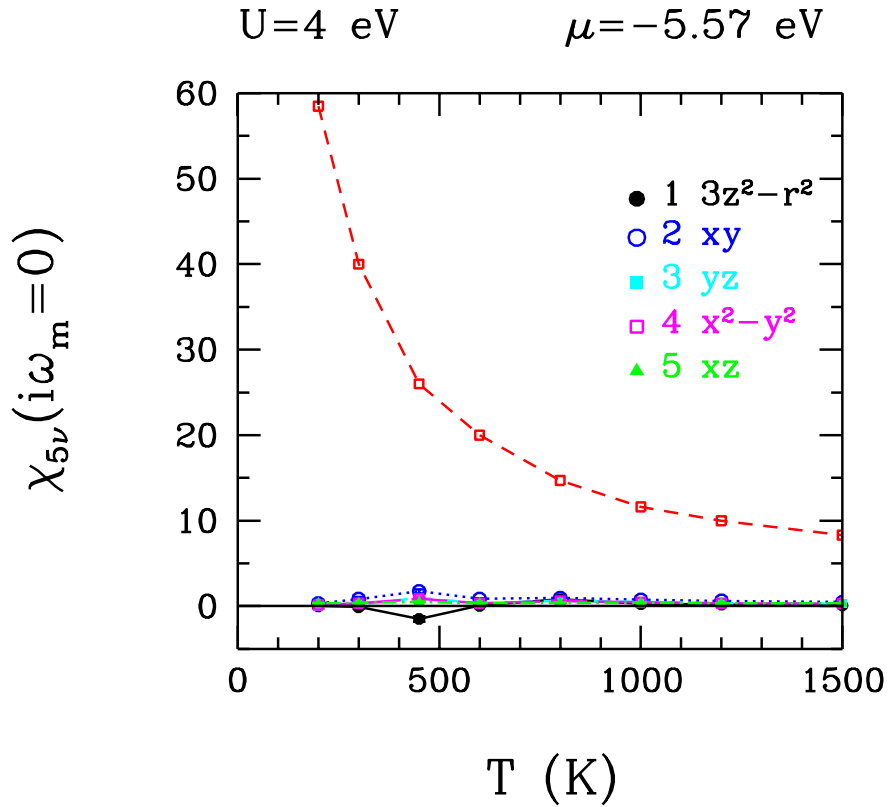


Figure 5.4. Number of warmup and measurement sweeps are shown as (warmup + measurements). For $T = 200$ K ($1k+1k$), $T = 300$ K ($5k+10k$), $T = 450$ K ($5k+10k$), $T = 600$ K ($5k+80k$), $T = 800$ K ($10k+100k$), $T = 1000$ K, ($5k+80k$) $T = 1200$ K ($5k+80k$), $T = 1500$ K ($5k+80k$). Red dash line shows magnetic susceptibility of 1 free spin. Magnetic susceptibility between xz and the other Co $3d$ orbitals $\chi_{5\nu}(i\omega_m = 0)$ vs temperature T .

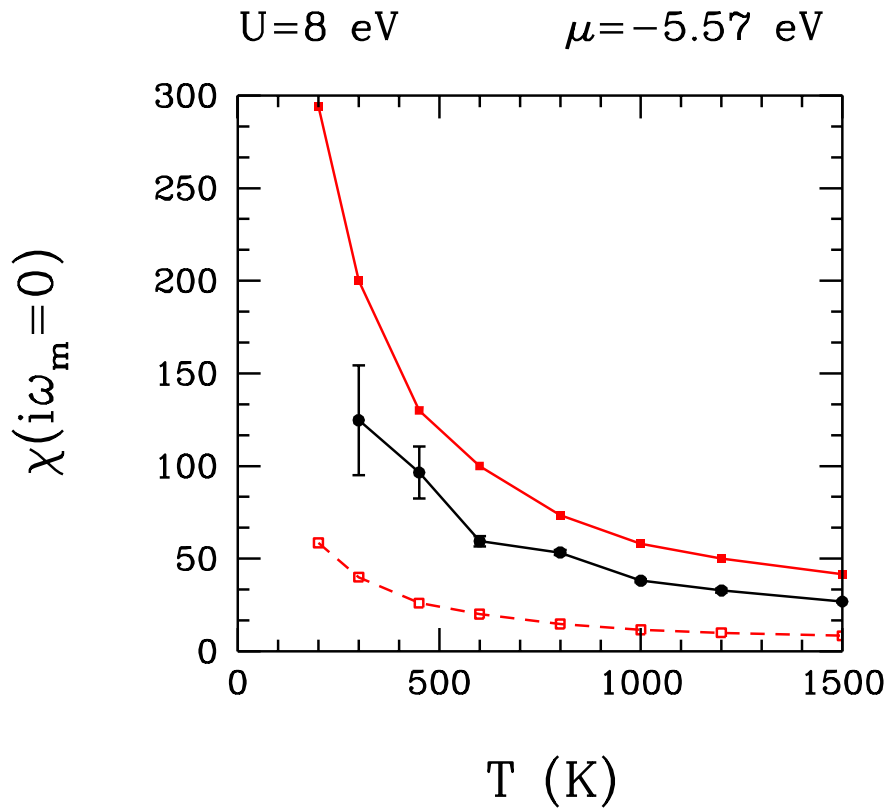


Figure 5.5. Number of warmup and measurement sweeps are shown as (warmup + measurements). For $T = 300 \text{ K}$ ($5k + 10k$), $T = 450 \text{ K}$ ($5k + 10k$), $T = 600 \text{ K}$ ($5k + 80k$), $T = 800 \text{ K}$ ($5k + 80k$), $T = 1000 \text{ K}$, ($5k + 80k$) $T = 1200 \text{ K}$ ($5k + 80k$), $T = 1500$ ($5k + 80k$). Red solid line shows magnetic susceptibility of 5 free spin. Red dash line shows magnetic susceptibility of 1 free spin. Onsite Coulomb interactions of $3d$ orbitals are $U = 8 \text{ eV}$. Total magnetic susceptibility $\chi(i\omega_m = 0)$ vs temperature T .

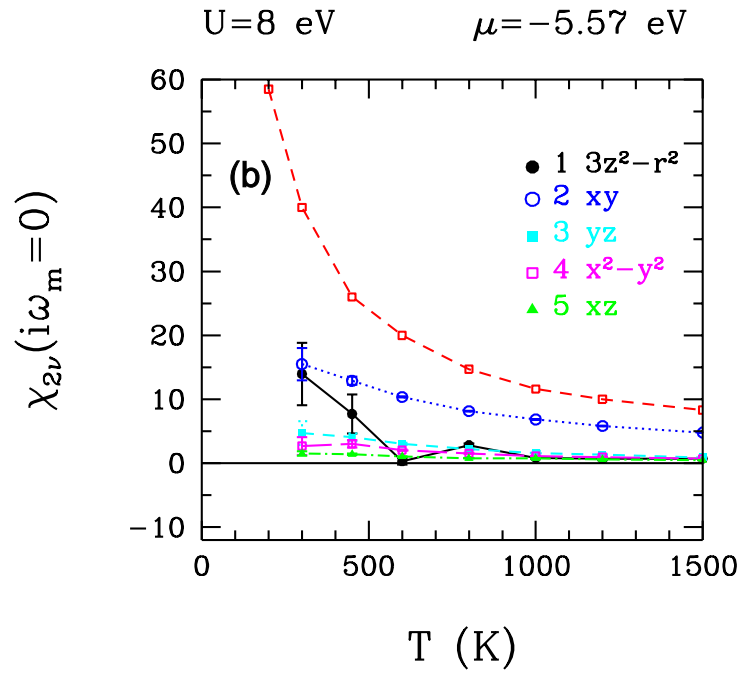
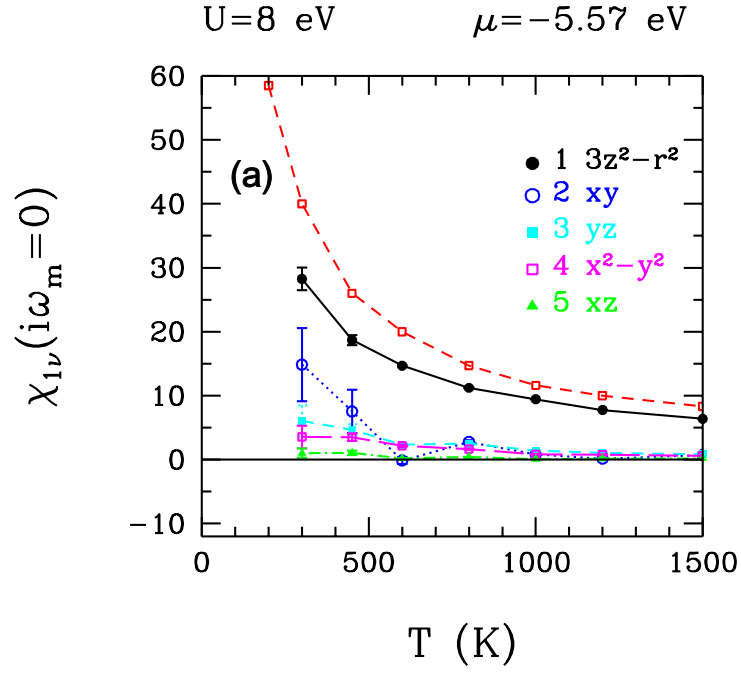


Figure 5.6. Number of warmup and measurement sweeps are shown as (warmup + measurements). For $T = 300$ K ($5k + 10k$), $T = 450$ K ($5k + 10k$), $T = 600$ K ($5k+80k$), $T = 800$ K ($5k+80k$), $T = 1000$ K, ($5k+80k$) $T = 1200$ K ($5k + 80k$), $T = 1500$ ($5k + 80k$). Red dash line shows magnetic susceptibility of 1 free spin. (a) Magnetic susceptibility between $3z^2 - r^2$ and the other Co $3d$ orbitals $\chi_{1\nu}(i\omega_m = 0)$ vs temperature T . (b) Magnetic susceptibility between xy and the other Co $3d$ orbitals $\chi_{2\nu}(i\omega_m = 0)$ vs temperature T

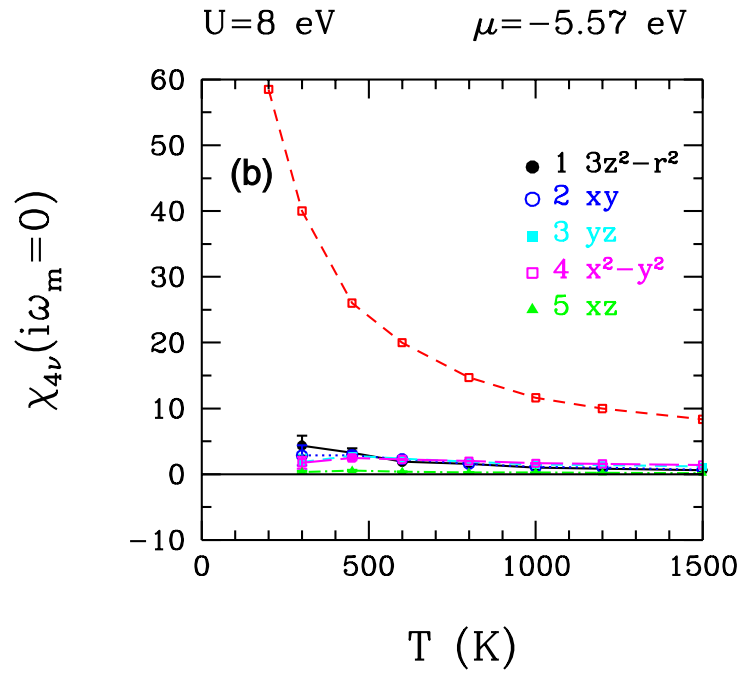
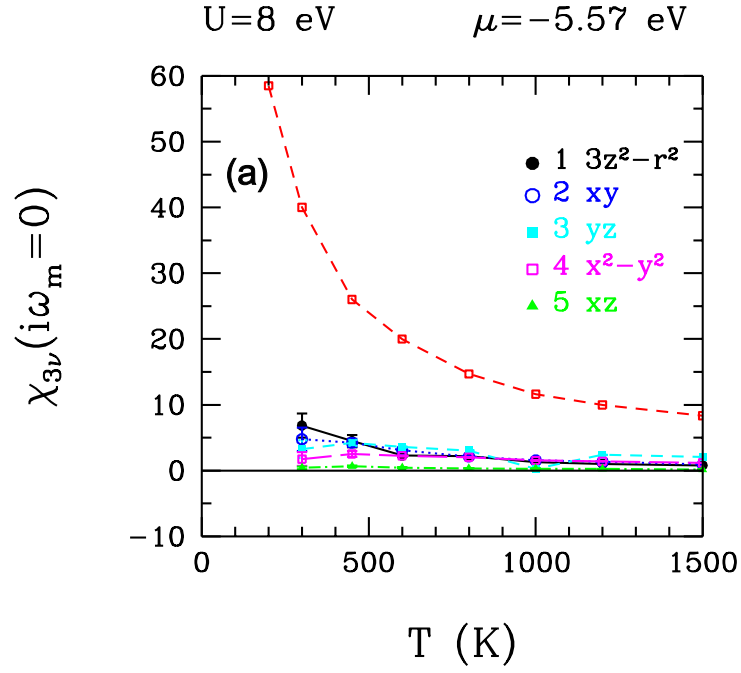


Figure 5.7. Number of warmup and measurement sweeps are shown as (warmup + measurements). For $T = 300$ K ($5k + 10k$), $T = 450$ K ($5k + 10k$), $T = 600$ K ($5k+80k$), $T = 800$ K ($5k+80k$), $T = 1000$ K, ($5k+80k$) $T = 1200$ K ($5k + 80k$), $T = 1500$ ($5k + 80k$). Red dash line shows magnetic susceptibility of 1 free spin. (a) Magnetic susceptibility between yz and the other Co $3d$ orbitals $\chi_{3\nu}(i\omega_m = 0)$ vs temperature T . (b) Magnetic susceptibility between $x^2 - y^2$ and the other Co $3d$ orbitals $\chi_{4\nu}(i\omega_m = 0)$ vs temperature T .

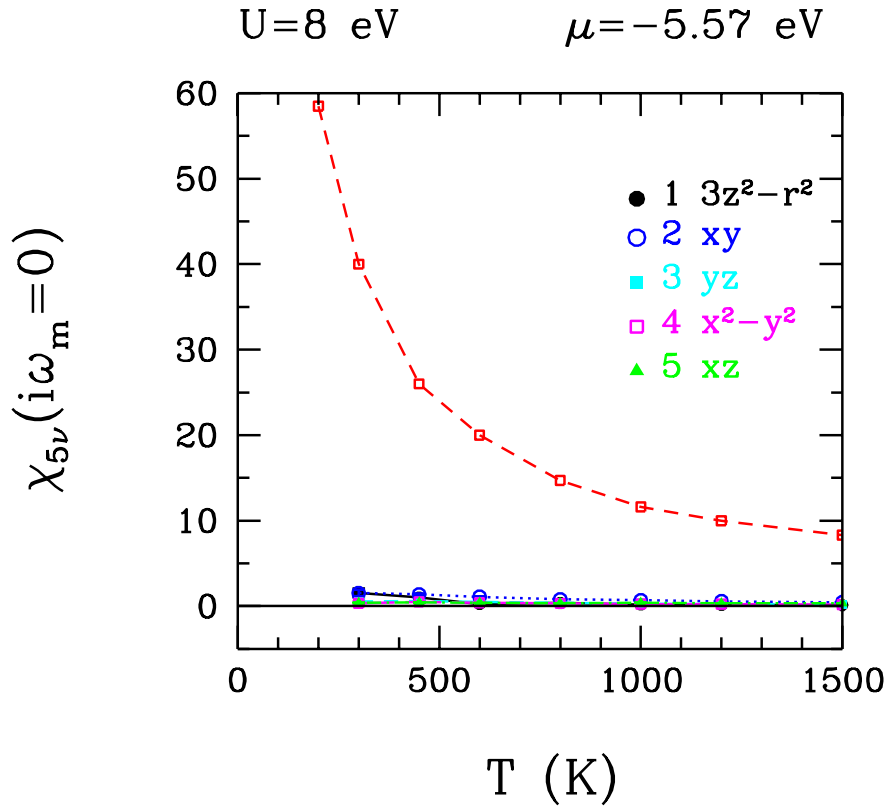


Figure 5.8. Number of warmup and measurement sweeps are shown as (warmup + measurements). For $T = 300$ K ($5k + 10k$), $T = 450$ K ($5k + 10k$), $T = 600$ K ($5k + 80k$), $T = 800$ K ($5k + 80k$), $T = 1000$ K, ($5k + 80k$) $T = 1200$ K ($5k + 80k$), $T = 1500$ ($5k + 80k$). Red dash line shows magnetic susceptibility of 1 free spin. Magnetic susceptibility between xz and the other Co $3d$ orbitals $\chi_{5\nu}(i\omega_m = 0)$ vs temperature T .

CHAPTER 6

CONCLUSION

In this thesis, the magnetic and electronic properties of $3d$ electrons of vitamin B₁₂ have been shown by using Hirsch-Fye QMC algorithm to the impurity Anderson model. For this model, Co $3d$ orbitals have been defined as impurity and the other orbitals construct host structure. For vitamin B₁₂, multi-orbital Anderson model have been defined and some terms which are eigenvalues of host and impurity electrons, hybridization between the impurity and host, hopping terms between the $3d$ orbitals and chemical potential were obtained from DFT calculations. By using DFT+QMC approach, onsite Coulomb interactions of $3d$ electrons are considered exactly. In Chapter 3, the results for static QMC measurements have been discussed. Furthermore, in this chapter, static QMC results have been compared with DFT results. Then, in Chapter 4, the results of dynamical QMC measurements have been represented. Single-orbital Hirsch-Fye QMC algorithm have been explained in Appendix A and this algorithm was used in study [8]. For metalloproteins, single-orbital Hirsch-Fye QMC algorithm have been converted multi-orbital case in Appendix B.

Firstly, the occupations have been discussed. QMC results have shown that occupations of $3d$ orbitals are less than 1 and $3d$ orbitals have 4.5 electrons. However, from DFT results, occupations of $3d$ orbitals were found to be approximately 2 and their total electron number were found to be 7.2. After that, by Hirsch-Fye QMC algorithm, square of the magnetic correlation function of $3d$ orbitals have been obtained and from these numerical results, effective magnetic moments of $3d$ orbitals have been calculated. These measurements have shown that effective magnetic moments are approximately 1. On the other hand, DFT found that effective magnetic moments equaled nearly 0. The reason of differences between the QMC and DFT measurements is that QMC considers onsite Coulomb interaction, however; DFT uses the Coulomb interaction as an approximation. QMC measurements say that with these strong electron-electron interactions, $3d$ orbitals can not be doubly-occupied and so their magnetic moments equal 1. This comparison shows the effect of strong onsite Coulomb interactions on occupations and magnetic correlation functions of $3d$ orbitals.

In static QMC measurements, occupations and magnetic correlation functions have been studied for different chemical potential values and these measurements have

been done for $U = 4$ eV and $U = 8$ eV. Due to hybridization between the host and impurity states, and onsite Coulomb interactions of $3d$ electrons, in semiconductor gap, the new states have been observed. This means that QMC results for semiconductor gap do not have same values with DFT results. Moreover, for QMC measurements, the semiconductor gap are different for $U = 4$ eV and $U = 8$ eV. The reason is that due to Coulomb interactions, the impurity states are broaden and their values equal $\epsilon_\nu + U$ so for $U = 8$ eV case, these states have been seen at higher energies. Therefore, semiconductor gap is large than for $U = 4$ eV case.

Next, the total magnetization functions of $3d$ orbitals have been calculated. Despite the fact that square of the magnetic correlation functions of $3d$ orbitals do not have temperature dependency, total magnetic correlation function of $3d$ orbitals are affected by changes in temperature. Therefore, it can be said that inter-orbital magnetic correlations are temperature dependent. Furthermore, numerical results have shown that at high temperatures, correlations between the $3d$ electrons are FM and at low temperatures, AFM correlations exist between them.

It is the important point that for total magnetic correlation function, at $T = 600$ K, the big error bars have been observed. While number of measurement sweeps were increased, error could not been decreased and at this temperature value, effective magnetic moment have changed between 1.7 and 3. The possible explanation of this situation can be that energies of high spin states and low spin states are very close so correlations fluctuate between FM and AFM.

In addition $U = 4$ eV case, all calculations were done for $U = 8$ eV to see the effect of Coulomb interactions on the measurements. For $U = 8$ eV, correlations again fluctuate between the FM and AFM, however; in this case, this situation has occurred at $T = 300$ K.

To control the results for total magnetic correlation functions, inter-orbital correlation functions have been obtained for $U = 4$ eV and $U = 8$ eV. For the former case, at high temperatures, all correlations are FM and at low temperatures, AFM correlations are seen. In other words, at high temperatures, electrons are at high spin state and they are a low spin state at low temperatures. For $U = 8$ eV, all correlations are FM at $T = 1550$ K. For this case, measurements should be done for lower temperatures than $T = 300$ K because due to strong Coulomb interactions, it is expected that low spin states can be detected below the $T = 300$ K.

After that, dynamical QMC measurements have been discussed and total magnetic susceptibility and susceptibilities between the $3d$ orbitals have been found. To explain

these results, Curie type magnetic susceptibilities of single electron and 5-free electrons were calculated. It has been observed that at high temperatures, $3d$ electrons behave as 5-free electron. Below $T = 800$ K, the total magnetic susceptibility decrease, which means that electrons go to low spin state and AFM correlations exist. At lower energies than $T = 450$ K, $3d$ electrons have similar behaviour with single free electron. The reason of this situation can be that 4 $3d$ electrons form 2 pairs and their correlations are AFM. Therefore, susceptibilities of these electrons can cancel each other and the only 1 $3d$ electron determines the total susceptibility.

To see what happens between the $3d$ electrons, inter-orbital magnetic susceptibilities were measured. It has been found that the strongest correlations are observed between the $3z^2 - r^2$ and the other $3d$ orbitals. The behavior of these correlations are similar with total magnetic susceptibility. The susceptibilities between the xy , yz , $x^2 - y^2$ and xz are small and these orbitals' interactions are very weak.

These results indicate that due to strong Coulomb interactions, $3d$ electrons show interesting electronic and magnetic properties. At high temperatures and low temperatures, it has been observed that electrons are at high spin states and low spin states, respectively. With correlations between the $3d$ electrons, the possible explanations for spin states have been done. To control these results, experiments on $3d$ orbitals of vitamin B₁₂ are necessary.

In addition, dynamical magnetic susceptibility measurements have shown that Co are paramagnetic because total magnetic susceptibility of Co $3d$ orbitals are similar with Curie type magnetic susceptibility at high and low temperatures. Paramagnetism of Co atom was estimated in study [15]. However, new experimental results for Co atom in vitamin B₁₂ are necessary.

In study [15], it was said that vitamin B₁₂ is diamagnetic. To obtain magnetic properties of vitamin B₁₂ and compare with previous results, QMC measurements for host and impurities should be done (see Appendix C for calculation of host-impurity Green's functions). Also with these measurements, total number of Co $3d$ orbitals can be found, which satisfies controlling whether Co is $3d^5$ or not.

REFERENCES

- [1] Stefano Marino. *A combined computational and experimental approach in the structural investigations of metalloproteins*. PhD thesis, Universita Degli Studi Di Padova, 2006.
- [2] N.J Robinson K.J Waldron. How to bacterial cells ensure that metalloproteins get the correct metal? *Nat.Rev.Microbiol*, 1:25–35, 7.
- [3] P. Kesari S. Jain P. K. Naik, P. Ranjan. About metalloproteins [http : //www.juit.ac.in/attachments/metallopred/aboutmetalloprotein.html](http://www.juit.ac.in/attachments/metallopred/aboutmetalloprotein.html).
- [4] Mike Hendrich. Metalloproteins [http : //www.chem.cmu.edu/groups/hendrich/](http://www.chem.cmu.edu/groups/hendrich/).
- [5] Jason Shearer. Metalloproteins [http : //www.chem.unr.edu/faculty/jms/](http://www.chem.unr.edu/faculty/jms/).
- [6] M.Era H.Kashiwagi F.Sato, T.Yoshihiro. Calculation of all-electron wavefunction of heme protein sytochrome c by density functional theory. *Chem.Phy.Lett.*, 341:645, 2001.
- [7] Zafer Kandemir. Mapping of the electronic structures of metalloproteins onto multi-orbital anderson model using density functional theory. Master’s thesis, Izmir Institute of Technology, 2013.
- [8] Yoshihiro Tomoda. Quantum monte carlo analysis on magnetic impurities in semiconductors. Master’s thesis, Institute for Materials Research, Tohoku University.
- [9] Zlatko MICKOVIC. *Study of Diluted Magnetic Semiconductors:the Case of Transition Metal Doped ZnO*. PhD thesis, Ecole Polytechnique Federale De Lausanne, 2010.
- [10] Germanas Peleckis. *Studies on diluted oxide magnetic semiconductors for spin electronic applications*. PhD thesis, University of Wollongong, 2006.
- [11] Rekha Rajaram. *Study of magnetism in diluted magnetic semiconductors based on III-V Nitrides*. PhD thesis, Stanford University, 2007.
- [12] P.W.Anderson. Localized magnetic states in metals. *Physical Review*, 124:1, 1961.
- [13] F.D.M. Haldane and P.W.Anderson. Simple model of multiple charge states of transition-metal impurities in semiconductors. *Physical Review B*, 13:2553, 1976.
- [14] Brigitte Surer. *First-principles simulations of multi-orbital systems with strong electronic correlations*. PhD thesis, ETH ZURICH, 2011.

- [15] Robert R. Sealock Harvey Diehl, Roy W. Vander Haar. The magnetic susceptibility of vitamin B₁₂. *Journal of the American Chemical Society*, 72:5312–5313, 1950.
- [16] J.E.Hirsch. Two-dimensional hubbard model: Numerical simulation study. *Physical Review B*, 31:7, 1985.
- [17] Rutgers University. Lecture note: Quantum monte carlo method in details.
- [18] J.E.Hirsch. Monte carlo method for magnetic impurities in metals. *Physical Review Letters*, 56:23, 1986.
- [19] S.Maekawa Y.Tomoda, N.Bulut. Inter-impurity and impurity-host magnetic correlations in semiconductors with low-density transition-metal impurities. *Physica B*, 404:1159–1168, 2008.

APPENDIX A

HIRSCH-FYE QUANTUM MONTE CARLO ALGORITHM FOR THE SINGLE-IMPURITY ANDERSON MODEL

In this appendix, the Hirsch-Fye Quantum Monte Carlo (HFQMC) algorithm for the single-orbital Anderson model is described. This algorithm uses the Hubbard-Stratonovich (HS) transformation to convert the interacting electron system to a non-interacting one. Moreover, with the HS transformation, electrons move in a fluctuating magnetic field which is defined by a random set of spin configurations. These configurations are accepted or rejected by Monte Carlo (MC) algorithms such as the heat-bath algorithm or the Metropolis algorithm. In this way, the finite temperature Green's functions which measure the electronic and magnetic properties of the system are calculated.

HFQMC algorithm is used for many strongly correlated systems such as diluted magnetic semiconductors (DMS). In DMS, a transition metal that behaves as a magnetic impurity is placed in semiconductor host. Some examples for DMS are manganese-doped indium arsenide and gallium arsenide (GaMnAs), cobalt-doped titanium dioxide, iron-doped tin dioxide. In [8], HFQMC algorithm was used for DMS and, the magnetic properties and electronic states were shown. In Appendix B, this single orbital algorithm will be changed to multi-orbital Anderson model to explain the electronic properties of Co 3d electrons.

A.1. Form of the Hamiltonian

The Hamiltonian for the single-orbital and single-impurity Anderson model can be defined ([13]) by

$$H = \sum_{k\sigma} (\varepsilon_k - \mu) c_{k\sigma}^\dagger c_{k\sigma} + \sum_{k\sigma} V_k (c_{k\sigma}^\dagger d_\sigma + h.c.) + \sum_{\sigma} (\varepsilon_d - \mu) n_{d\sigma} + U n_{d\uparrow} n_{d\downarrow}. \quad (\text{A.1})$$

Here, ε_k denotes the eigenvalues of the host electrons, $c_{k\sigma}^\dagger$ ($c_{k\sigma}$) is the creation (annihilation) operator for the host electrons, V_k is the hybridization term between the host

and impurity electrons, ε_d denotes the eigenvalues of the impurity electrons, d_σ^\dagger (d_σ) is the creation (annihilation) operator for the impurity electrons, U specifies the Coulomb interaction between the d electrons and $n_{d\sigma}$ is the site occupation number of a d electron with $\sigma = \uparrow$ and $\sigma = \downarrow$ which denote the two orientations of the electron spins and μ is the chemical potential.

The above Hamiltonian can be rewritten as a sum of two terms, H_0 and H_1 :

$$H \equiv H_0 + H_1, \quad (\text{A.2})$$

where H_0 is the non-interacting term:

$$H_0 = \sum_{k\sigma} (\varepsilon_k - \mu) c_{k\sigma}^\dagger c_{k\sigma} + \sum_{k\sigma} V_k (c_{k\sigma}^\dagger d_\sigma + h.c.) + \sum_{\sigma} (\varepsilon_d - \mu) n_{d\sigma} + \frac{U}{2} (n_{d\uparrow} + n_{d\downarrow}) \quad (\text{A.3})$$

and H_1 is the interacting term:

$$H_1 = U n_{d\uparrow} n_{d\downarrow} - \frac{U}{2} (n_{d\uparrow} + n_{d\downarrow}) \quad (\text{A.4})$$

that will be treated using the HS transformation.

A.2. The Hubbard-Stratonovich Transformation, Trotter Break-Up and Partition Function

The partition function Z representation is a convenient starting point to perform the quantum Monte Carlo (QMC) algorithm for the electron-electron interaction systems. When the Coulomb term which is H_1 is taken into account, this problem is very difficult. In order to treat it, we use the Trotter decomposition and Hubbard-Stratonovich transformation. They introduces the freedom on the imaginary time axis and converts H_1 into a form where electrons become decoupled from each other.

First, we introduce the partition function in Monte Carlo method:

$$Z = \text{Tr} [e^{-\beta H}] = \text{Tr} \left[\prod_{l=1}^L e^{-\Delta\tau H} \right] \quad (\text{A.5})$$

$$\text{Tr} \left[\prod_{l=1}^L e^{-\Delta\tau (H_0 + H_1)} \right] \simeq \text{Tr} \left[\prod_{l=1}^L e^{-\Delta\tau H_0} e^{-\Delta\tau H_1} + \vartheta(\Delta\tau^2) \right]. \quad (\text{A.6})$$

The imaginary time interval $[0, \beta]$ is discretized into L time slices with $\beta \equiv \Delta\tau L$, and by using the Trotter break-up, the partition function is obtained. This is the only approximation in the QMC. Next, for Hubbard-Stratonovich transformation, we define the identity

$$n_{d\uparrow} n_{d\downarrow} = -\frac{1}{2} (n_{d\uparrow} - n_{d\downarrow})^2 + \frac{1}{2} (n_{d\uparrow} + n_{d\downarrow}), \quad (\text{A.7})$$

and use it in the interaction term,

$$H_1 = -\frac{U}{2} (n_{d\uparrow} - n_{d\downarrow})^2. \quad (\text{A.8})$$

With $\cosh(\lambda) = e^{\frac{1}{2}\Delta\tau U}$,

$$e^{-\Delta\tau H_1} = e^{-\Delta\tau \frac{U}{2} (n_{d\uparrow} - n_{d\downarrow})^2} \quad (\text{A.9})$$

$$= \frac{1}{2} \sum_{S=\pm 1} e^{\lambda S (n_{d\uparrow} - n_{d\downarrow})}. \quad (\text{A.10})$$

Here, S is an auxiliary Hubbard-Stratonovich field and the sum over of these discrete S variables is the essential of the Hirsch-Fye QMC algorithm. By using the Hubbard-Stratonovich transformation and Trotter approximation, the partition function is formu-

lated as

$$Z = Tr \left[\prod_{l=1}^L \frac{1}{2} \sum_{S_l=\pm 1} e^{-\Delta\tau H_0} e^{\lambda S_l (n_{d\uparrow} - n_{d\downarrow})} \right] \quad (\text{A.11})$$

$$\begin{aligned} &= Tr \prod_{l=1}^L \frac{1}{2} \sum_{S_l=\pm 1} \exp \left\{ -\Delta\tau \sum_{ij} c_{i\uparrow}^\dagger K_{ij} c_{j\uparrow} \right\} \exp \{ +\lambda S_l n_{d\uparrow} \} \\ &\quad \times \exp \left\{ -\Delta\tau \sum_{ij} c_{i\downarrow}^\dagger K_{ij} c_{j\downarrow} \right\} \exp \{ -\lambda S_l n_{d\downarrow} \} \end{aligned} \quad (\text{A.12})$$

where

$$H^\uparrow(l) = \sum_{ij} c_{i\uparrow}^\dagger K_{ij} c_{j\uparrow} - \frac{\lambda S_l n_{d\uparrow}}{\Delta\tau}, \quad (\text{A.13})$$

$$H^\downarrow(l) = \sum_{ij} c_{i\downarrow}^\dagger K_{ij} c_{j\downarrow} + \frac{\lambda S_l n_{d\downarrow}}{\Delta\tau}, \quad (\text{A.14})$$

$$H_0 = \sum_{i,j,\sigma} a_{i\sigma}^\dagger K_{ij} a_{j\sigma}. \quad (\text{A.15})$$

Here, a denotes both c and d orbitals, K is a $(N+1) \times (N+1)$ matrix for the bilinear part of H and N is the number of the host states.

Let's define

$$V^\sigma = \sigma \lambda S. \quad (\text{A.16})$$

$V^\sigma = \sigma \lambda S |d\rangle \langle d|$ only acts at the impurity site so it is a diagonal $(N+1) \times (N+1)$ matrix with the element $e^{\lambda\sigma S}$ for the impurity site and 1 for the host sites,

$$e^{V^\sigma} = \begin{bmatrix} e^{\lambda\sigma S} & & & & & \\ & 1 & & & & \\ & & 1 & & & \\ & & & \ddots & & \\ & \mathbf{0} & & & & \\ & & & & & \\ & & & & & \\ & & & & & 1 \end{bmatrix} \quad (\text{A.17})$$

Let's introduce now the following matrix $B_l(\sigma) = e^{-\Delta\tau K} e^{V_l^\sigma}$. By using this definition, the partition function is written

$$Z = \sum_{S_1, S_2, \dots, S_L} \prod_{\sigma=\pm 1} \det [I + B_L(\sigma) B_{L-1}(\sigma) \dots B_1(\sigma)] \quad (\text{A.18})$$

$$\equiv \sum_{S_1, S_2, \dots, S_L} \det \vartheta_{S_1 S_2 \dots S_L}(\uparrow) \det \vartheta_{S_1 S_2 \dots S_L}(\downarrow). \quad (\text{A.19})$$

$\vartheta(\sigma)$ is an $(N+1)L \times (N+1)L$ matrix and the derivation of this result is given in [16].

$$\vartheta_{S_1, S_2, \dots, S_L(\sigma)} = \begin{matrix} & l=1 & l=2 & & & l=L \\ \begin{bmatrix} I & 0 & 0 & \dots & \dots & B_L(\sigma) \\ -B_1(\sigma) & I & 0 & \dots & \dots & \\ 0 & -B_2(\sigma) & I & 0 & 0 & 0 \\ \cdot & 0 & \dots & \dots & \dots & 0 \\ \cdot & 0 & 0 & 0 & -B_{L-1}(\sigma) & I \end{bmatrix} & & & & & \end{matrix} \quad (\text{A.20})$$

A.3. Dyson's Equation of the Green's Functions

We define the single particle Green's function as

$$G^\sigma = -\langle T_\tau d_\sigma(\tau) d_\sigma^\dagger(0) \rangle \quad (\text{A.21})$$

$$= -\frac{1}{Z} \text{Tr} T_\tau d_\sigma(\tau) d_\sigma^\dagger(0) e^{-\beta H}. \quad (\text{A.22})$$

Now, we recall $\vartheta(\sigma)$ matrix which is related to the Green's function by the identity

$$G^\sigma = (\vartheta(\sigma))^{-1}, \quad (\text{A.23})$$

as shown in [17]. The size of the $\vartheta_{S_1, S_2, \dots, S_L}$ is $(N+1)L \times (N+1)L$ and the calculation of the Green's functions for every set S_1, S_2, \dots, S_L of spins from this large size matrix is very difficult.

Hirsch and Fye [18] noted that the Green's function G can be calculated only once for a certain spin configuration S_1, S_2, \dots, S_L and after that, G can be updated for a new set of configuration where only one spin is changed. The Green's functions which are different only by one "spin flip" are related to each other by a Dyson's equation. To derive this equation, it is more useful to work with

$$\tilde{G}^\sigma = e^{V^\sigma} G^\sigma. \quad (\text{A.24})$$

This relation is calculated by using $\vartheta(\sigma)$.

$$(\vartheta(\sigma) e^{-V_i^\sigma})^{-1} = (\vartheta(\sigma))^{-1} e^{V^\sigma} \quad (\text{A.25})$$

$$= e^{V^\sigma} G^\sigma \equiv \tilde{G}^\sigma, \quad (\text{A.26})$$

so

$$G^\sigma = e^{-V^\sigma} \tilde{G}^\sigma. \quad (\text{A.27})$$

The matrix representation of $\vartheta(\sigma) e^{V_i^\sigma}$ is

$$\vartheta(\sigma) e^{V_i^\sigma} = \begin{bmatrix} e^{-V_1^\sigma} & & & & e^{\Delta\tau K} \\ -e^{-\Delta\tau K} & e^{-V_2^\sigma} & & & \mathbf{0} \\ & & -e^{\Delta\tau K} & e^{-V_3^\sigma} & \\ \mathbf{0} & & & & -e^{\Delta\tau K} & e^{-V_L^\sigma} \end{bmatrix}$$

.

When the HS field is changed, only the diagonal elements of $\vartheta(\sigma) e^{V^\sigma}$ change so we can write

$$\vartheta(\sigma') e^{-V^{\sigma'}} - \vartheta(\sigma) e^{-V^\sigma} = e^{-V^{\sigma'}} - e^{-V^\sigma} \equiv C. \quad (\text{A.28})$$

Then,

$$(\tilde{G}^{\sigma'})^{-1} - (\tilde{G}^\sigma)^{-1} = C \quad (\text{A.29})$$

$$\tilde{G}^\sigma - \tilde{G}^{\sigma'} = \tilde{G}^\sigma C \tilde{G}^{\sigma'} \quad (\text{A.30})$$

$$\tilde{G}^{\sigma'} = \tilde{G}^\sigma - \tilde{G}^\sigma C \tilde{G}^{\sigma'}. \quad (\text{A.31})$$

By substituting $\tilde{G}^\sigma = e^{V^\sigma} G^\sigma$,

$$e^{V^{\sigma'}} G^{\sigma'} = e^{V^\sigma} G^\sigma - e^{V^\sigma} G^\sigma (e^{-V^{\sigma'}} - e^{-V^\sigma}) e^{V^{\sigma'}} G^{\sigma'}. \quad (\text{A.32})$$

If we divide both sides with $e^{V^{\sigma'}}$, we obtain

$$G^{\sigma'} = e^{V^\sigma - V^{\sigma'}} G^\sigma - e^{V^\sigma - V^{\sigma'}} G^\sigma (I - e^{V^{\sigma'} - V^\sigma}) G^{\sigma'}, \quad (\text{A.33})$$

and

$$G^{\sigma'} = e^{V^{\sigma}-V^{\sigma'}} G^{\sigma} + e^{V^{\sigma}-V^{\sigma'}} G^{\sigma} (e^{V^{\sigma'}-V^{\sigma}} - I) G^{\sigma'}. \quad (\text{A.34})$$

The following relation is used for the new spin configuration Green's function G' and the old spin configuration Green's function G , (by omitting σ)

$$G' = G + (G - I)(e^{V'-V} - I) G'. \quad (\text{A.35})$$

So,

$$G' = G + G(e^{V'-V} - I) G' - (e^{V'-V} - I) G', \quad (\text{A.36})$$

and

$$e^{V'-V} G' = G + G(e^{V'-V} - I) G'. \quad (\text{A.37})$$

Then, the new spin configuration Green's function and the old spin configuration Green's function have the relation

$$G' = e^{V-V'} G + e^{V-V'} G(e^{V'-V} - I) G'. \quad (\text{A.38})$$

Note that $e^{V'-V} - I$ has non-zero matrix elements only at the impurity sites. V' shows the new configuration while V indicates the old configuration so only the components of G at the d sites are related each other. Hence, if we consider only the d component of G from

$$G' = G + (G - I)(e^{V'-V} - I) G', \quad (\text{A.3.39})$$

$$G'_{dd} = G_{dd} + (G_{dd} - I) (e^{V'-V} - I) G'_{dd}, \quad (\text{A.3.40})$$

where G_{dd} is a $L \times L$ matrix, $(e^{V'-V} - I)$ is a $L \times L$ diagonal matrix and I is the $L \times L$ identity matrix.

$$\left(e^{V'-V} \right)_{l,l'} = \delta_{ll'} e^{\lambda \sigma (S_{l'} - S_l)}. \quad (\text{A.3.41})$$

We obtain the new impurity Green's function from the Dyson's equation

$$G'_{dd} = [I - (G_{dd} - I) (e^{V'-V} - I)]^{-1} G_{dd}. \quad (\text{A.3.42})$$

A.4. Impurity Green's Function for the New Hubbard-Stratonovich Field Configuration

After the spin S_l is flipped, we know that the new impurity Green's function is obtained from the relation

$$G'_{dd} = G_{dd} + (G_{dd} - I) (e^{V'-V} - I) G'_{dd}. \quad (\text{A.4.1})$$

By substituting

$$G'_{dd} = [I - (G_{dd} - I) (e^{V'-V} - I)]^{-1} G_{dd} \quad (\text{A.4.2})$$

$$\begin{aligned} G'_{dd} &= G_{dd} + (G_{dd} - I) (e^{V'-V} - I) \\ &\quad \times [I - (G_{dd} - I) (e^{V'-V} - I)]^{-1} G_{dd}. \end{aligned} \quad (\text{A.4.3})$$

$$A = \begin{bmatrix} 1 & A_{1l} & & & & \\ & 1 & A_{2l} & & & \\ & & A_{3l} & & & \\ & & & 1 & & \\ & \mathbf{0} & & & \cdot & \\ & & & & & \cdot \\ & & A_{Ll} & & & 1 \end{bmatrix} \quad (\text{A.4.7})$$

After S_l is flipped, the new impurity Green's function is given by

$$G'_{dd}(l_1, l_2) = G_{dd}(l_1, l_2) + \sum_{l_3, l_4} (G_{dd} - I)_{l_1, l_3} (e^{V' - V})_{l_3, l_3} (A^{-1})_{l_3, l_4} (G_{dd})_{l_4, l_2}, \quad (\text{A.4.8})$$

and

$$G'_{dd}(l_1, l_2) = G_{dd}(l_1, l_2) + \sum_{l_4} (G_{dd}(l_1, l) - \delta_{l_1, l}) (e^{V' - V}) (A^{-1})_{l, l_4} G_{dd}(l_4, l_2). \quad (\text{A.4.9})$$

where

$$(A^{-1})_{l, l_4} = \delta_{l, l_4} \frac{1}{[I + (I - G_{dd}(l, l)) (e^{V'_i - V_i} - I)]}. \quad (\text{A.4.10})$$

Then,

$$G'_{dd}(l_1, l_2) = G_{dd}(l_1, l_2) + (G_{dd}(l_1, l) - \delta_{l_1, l}) (e^{V' - V} - I) \\ \times \frac{1}{[I + (I - G_{dd}(l, l))(e^{V'_l - V_l} - I)]} (G_{dd})_{l, l_2}. \quad (\text{A.4.11})$$

A.5. Ratio of the Fermion Determinants

In a quantum Monte Carlo simulation, new spin configurations are generated by a probability which is proportional to the ratio of the determinants of $\vartheta'(\sigma)$ and $\vartheta(\sigma)$. For a proposed change of the Hubbard-Stratonovich field S_l

$$S_l \rightarrow S'_l = -S_l,$$

the ratio of the determinants for the new and the old configuration is

$$R_\sigma = \frac{\det \vartheta_{S'_l}(\sigma)}{\det \vartheta_{S_l}(\sigma)} = I + [I - G_{dd}^\sigma(l, l)] \left(e^{V_i^{\sigma'} - V_i^\sigma} - I \right). \quad (\text{A.5.1})$$

In order to prove it, we start from

$$\tilde{G}' = \tilde{G} - \tilde{G} (e^{-V'} - e^{-V}) \tilde{G}', \quad (\text{A.5.2})$$

where

$$\tilde{G} = e^V G. \quad (\text{A.5.3})$$

Multiplying both sides with $(\tilde{G}')^{-1}$ on the right, we get

$$I = \tilde{G} (\tilde{G}')^{-1} - \tilde{G} (e^{-V'} - e^{-V}). \quad (\text{A.5.4})$$

Then,

$$\tilde{G} (\tilde{G}')^{-1} = I + \tilde{G} (e^{-V'} - e^{-V}). \quad (\text{A.5.5})$$

Since

$$\tilde{G} = e^V G = e^V \vartheta^{-1}, \quad (\text{A.5.6})$$

we have

$$(e^V \vartheta^{-1}) \left[e^{V'} (\vartheta')^{-1} \right]^{-1} = I + e^V G (e^{-V'} - e^{-V}), \quad (\text{A.5.7})$$

$$e^V (\vartheta^{-1} \vartheta') e^{-V'} = I + e^V G (e^{-V'} - e^{-V}). \quad (\text{A.5.8})$$

Here, we multiply on the left with e^{-V} and on the right with $e^{V'}$, which yields

$$\vartheta^{-1} \vartheta' = e^{-V} e^{V'} + G (e^{-V'} - e^{-V}) e^{V'}, \quad (\text{A.5.9})$$

$$\vartheta^{-1} \vartheta' = e^{V'-V} + G (I - e^{V'-V}) \quad (\text{A.5.10})$$

$$= e^{V'-V} + (G - I)(I - e^{V'-V}) + I(I - e^{V'-V}), \quad (\text{A.5.11})$$

so

$$\vartheta^{-1} \vartheta' = I + (I - G)(e^{V'-V} - I). \quad (\text{A.5.12})$$

Taking the determinant of both sides, we obtain

$$\frac{\det \vartheta'}{\det \vartheta} = \det (I + (I - G)(e^{V' - V} - I)). \quad (\text{A.5.13})$$

The spin flip is only at one d site and this way

$$\det (I + (I - G)(e^{V' - V} - I)) = I + (I - G_{dd}^\sigma(l, l))(e^{V'_i - V_i} - I). \quad (\text{A.5.14})$$

Hence

$$R_\sigma = I + (I - G_{dd}^\sigma(l, l))(e^{V'_i - V_i} - I). \quad (\text{A.5.15})$$

Here, a quantum Monte Carlo algorithm which is the heat-bath algorithm is used to determine whether the new spin state is accepted. In this algorithm, the transition probability from one state S_l to another state S'_l is

$$P(S_l \rightarrow S'_l) = \frac{1}{\prod_\sigma R_\sigma + 1} \quad (\text{A.5.16})$$

A.6. Impurity Green's Function for Vanishing Hubbard - Stratonovich Field

In HF [18], $G^0(l, l')$ is defined by

$$G^0(l, l') = T \sum_{i\omega_n} e^{-i\omega_n \Delta\tau(l-l')} G^0(i\omega_n). \quad (\text{A.6.1})$$

for $l, l' = 1, \dots, L$. However, for $l = l'$ we need to be careful. In the simulation, $G^0(i\omega_n)$ is the impurity Green's function for H_0 defined by

$$H_0 = \sum_{k\sigma} \varepsilon_k c_{k\sigma}^\dagger c_{k\sigma} + \sum_{k\sigma} V_k \left(c_{k\sigma}^\dagger d_\sigma + h.c. \right) + \left(\varepsilon_d + \frac{U}{2} \right) \sum_{\sigma} n_{d\sigma}. \quad (\text{A.6.2})$$

Then

$$G^0(i\omega_n) = \frac{1}{i\omega_n - \left(\varepsilon_d + \frac{U}{2} \right) - F_0(i\omega_n)}, \quad (\text{A.6.3})$$

where the self-energy

$$F_0(i\omega_n) = V^2 \sum_k \frac{1}{i\omega_n - \varepsilon_k}. \quad (\text{A.6.4})$$

Here, $\omega_n = (2n+1)\pi T$ is the Matsubara frequency with the temperature T and F_0 is the self energy. When $l = l'$, we define $G^0(l, l)$ by

$$G^0(l, l) = \lim_{\tau \rightarrow 0^+} T \sum_{i\omega_n} e^{-i\omega_n \tau} G^0(i\omega_n). \quad (\text{A.6.5})$$

We evaluate this expression from

$$G^0(l, l) = \left(T \sum_{i\omega_n} G^0(i\omega_n) - T \sum_{i\omega_n} \frac{1}{i\omega_n - \left(\varepsilon_d + \frac{U}{2} \right)} \right) - \left[1 - f\left(\varepsilon_d + \frac{U}{2} \right) \right]. \quad (\text{A.6.6})$$

In the QMC algorithm, we calculate $G^0(l, l')$ for $l = l'$ case and $l \neq l'$ case. After that, we use

$$G^0(\tau_l) = -G^0(\tau_l + \beta) = -G^0(\tau_{l+L}) \quad (\text{A.6.7})$$

to obtain $G^0(\tau_l)$ for $-L \leq l \leq -1$ and $l = L$. Hence, we have $G^0(\tau_l)$ for $-L \leq l \leq L$.

A.7. Calculation of the Impurity Green's Function for Vanishing Hubbard - Stratonovich Field

Here, we define the Green's function $G_{dd}^\sigma(l, l')$ with the minus sign,

$$G_{dd}^\sigma(l, l') = - \left\langle T_\tau d_\sigma(l) d_\sigma^\dagger(l') \right\rangle. \quad (\text{A.7.1})$$

Here, T_τ is the Matsubara time ordering operator. The non-interacting Green's function can be obtained with setting all spins S_1, S_2, \dots, S_L to 0.

$$\begin{array}{c} \text{d} \quad \text{d} \\ \text{---} \text{---} \\ \text{---} \text{---} \end{array} = \text{---} \text{---} \quad + \quad \begin{array}{c} \text{d} \quad \text{c} \quad \text{c} \quad \text{d} \quad \text{d} \\ \text{---} \times \text{---} \text{---} \times \text{---} \text{---} \\ \text{---} \end{array} \quad \begin{array}{c} (-iV) \quad (-iV^*) \end{array}$$

Figure A.1. Feynman diagram representing the Green's function $G_{dd}^0(i\omega_n)$ for the $U = 0$. The double lines denote G_{dd}^0 while the single lines denote with the indices c and d , $G_c^0(i\omega_n)$ and $G_{dd}^{00}(i\omega_n)$, respectively. Here, $G_c^0(i\omega_n)$ is the Green's function for the host electrons.

$$\begin{aligned} i G_{dd}^0(i\omega_n) &= i G_{dd}^{00}(i\omega_n) \\ &+ (i G_{dd}^{00}(i\omega_n)) (-iV) (i G_c^0(k)) (-iV^*) (i G_{dd}^0(i\omega_n)) \end{aligned} \quad (\text{A.7.2})$$

$$G_{dd}^0(i\omega_n) = G_{dd}^{00}(i\omega_n) + \sum_k (-1)^2 i^4 V^2 G_{dd}^{00}(i\omega_n) G_c^0(k) G_{dd}^0(i\omega_n). \quad (\text{A.7.3})$$

Then, the impurity Green's function for $S_l = 0$ case is

$$G_{dd}^0(i\omega_n) = \frac{G_{dd}^{00}(i\omega_n)}{1 - \sum_k V^2 G_{dd}^{00}(i\omega_n) G_c^0(k)} \quad (\text{A.7.4})$$

$$= \frac{1}{(G_{dd}^{00}(i\omega_n))^{-1} - \sum_k V^2 G_c^0(k)}. \quad (\text{A.7.5})$$

Here, the impurity Green's function and host Green's function with no hybridization and no Coulomb interaction are

$$G_{dd}^{00}(i\omega_n) = \frac{1}{i\omega_n - \varepsilon_d}, \quad (\text{A.7.6})$$

$$G_c^0(k) = \frac{1}{i\omega_n - \varepsilon_k}. \quad (\text{A.7.7})$$

So,

$$G_{dd}^0(i\omega_n) = \frac{1}{i\omega_n - \varepsilon_d - V^2 \sum_k \frac{1}{i\omega_n - \varepsilon_k}}. \quad (\text{A.7.8})$$

A.8. Procedure to Update the Impurity Green's Functions

Up to now, all steps of Hirsch-Fye quantum Monte Carlo algorithm have been derived. In summary, the update of the Green's function in our program is the following. Firstly, we calculate the $G_{dd}^0(i\omega_n)$ which is the Green's function for non-zero hybridization and no Hubbard field. After that, for an initial spin configuration, $G_{dd}(l, l')$ is calculated. State of whole system is changed from S_l to S_l' with probability $P(S_l \rightarrow S_l')$. Then the Green's function is updated if $P(S_l \rightarrow S_l')$ is larger than the random number which is generated from 1 to 0.

APPENDIX B

HIRSCH-FYE QUANTUM MONTE CARLO ALGORITHM FOR THE MULTI-ORBITAL ANDERSON MODEL

In this section, the Hirsch-Fye QMC algorithm for the multi-orbital Anderson model is developed. For this case, we have 5 d orbitals and so the size of the impurity Green's functions is $5L \times 5L$. The algorithm for the multi-orbital case is similar to the single-orbital case but there are some differences. In the below sections, we will discuss the multi-orbital algorithm which we use for the study of metalloproteins.

B.1. Form of the Hamiltonian

Here the Hamiltonian for the multi-orbital case is defined :

$$\begin{aligned}
 H = & \sum_{m\sigma} (\varepsilon_m - \mu) c_{m\sigma}^\dagger c_{m\sigma} + \sum_{m\sigma} \sum_{\nu=1}^5 V_{m\nu} (c_{m\sigma}^\dagger d_{\nu\sigma} + h.c.) \\
 & + \sum_{\nu=1}^5 \sum_{\sigma} (\varepsilon_{d\nu} - \mu) n_{d\nu\sigma} + \sum_{\nu=1}^5 U_{\nu} n_{d\nu\uparrow} n_{d\nu\downarrow}. \tag{B.1.1}
 \end{aligned}$$

In the previous part, \vec{k} denotes the wave vector of the host lattice structure. But in the study of metalloproteins, m denotes the host eigenstates which are obtained by density functional theory calculation of the electronic structure of metalloproteins. Furthermore, ν is the index of the d orbitals ranging from 1 to 5. For proteins, the hopping terms between d orbitals are included so the Hamiltonian is written by

$$\begin{aligned}
 H = & \sum_{m\sigma} (\varepsilon_m - \mu) c_{m\sigma}^\dagger c_{m\sigma} + \sum_{m\sigma} \sum_{\nu=1}^5 V_{m\nu} (c_{m\sigma}^\dagger d_{\nu\sigma} + h.c.) \\
 & + \sum_{\nu,\nu'=1}^5 \sum_{\sigma} (t_{\nu\nu'} d_{\nu\sigma}^\dagger d_{\nu'\sigma} + h.c.) + \sum_{\nu=1}^5 \sum_{\sigma} (\varepsilon_{d\nu} - \mu) n_{d\nu\sigma} \\
 & + \sum_{\nu=1}^5 U_{\nu} n_{d\nu\uparrow} n_{d\nu\downarrow}, \tag{B.1.2}
 \end{aligned}$$

where $t_{\nu\nu'}$ is the hopping term. The Hamiltonian is divided into two parts which are the non-interacting part H_0 and the interacting part H_1

$$H \equiv H_0 + H_1, \quad (\text{B.1.3})$$

where

$$H_0 = \sum_{m\sigma} (\varepsilon_m - \mu) c_{m\sigma}^\dagger c_{m\sigma} + \sum_{m\sigma} \sum_{\nu=1}^5 V_{m\nu} (c_{m\sigma}^\dagger d_{\nu\sigma} + h.c.) \\ + \sum_{\nu=1}^5 \sum_{\sigma} (\varepsilon_{d\nu} - \mu) n_{d\nu\sigma} + \sum_{\nu=1}^5 U_\nu/2 (n_{d\nu\uparrow} + n_{d\nu\downarrow}), \quad (\text{B.1.4})$$

$$H_1 = \sum_{\nu=1}^5 U_\nu n_{d\nu\uparrow} n_{d\nu\downarrow} - \sum_{\nu=1}^5 U_\nu/2 (n_{d\nu\uparrow} + n_{d\nu\downarrow}). \quad (\text{B.1.5})$$

The interaction Hamiltonian H_1 is treated by using the Hubbard-Stratonovich transformation.

B.2. The Hubbard-Stratonovich Transformation, Trotter Break-Up and Partition Function

The next step is the Hubbard-Stratonovich (HS) transformation. In the interaction Hamiltonian, if we replace $n_{d\nu\uparrow} n_{d\nu\downarrow}$ term with

$$n_{d\nu\uparrow} n_{d\nu\downarrow} = -\frac{1}{2} (n_{d\nu\uparrow} - n_{d\nu\downarrow})^2 + \frac{1}{2} (n_{d\nu\uparrow} + n_{d\nu\downarrow}), \quad (\text{B.2.1})$$

we obtain

$$H_1 = \sum_{\nu} -\frac{U_\nu}{2} (n_{d\nu\uparrow} - n_{d\nu\downarrow})^2. \quad (\text{B.2.2})$$

With $\cosh(\lambda_\nu) = e^{\frac{1}{2}\Delta\tau U_\nu}$,

$$\exp\{-\Delta\tau H_1\} = \exp\left\{-\Delta\tau \sum_\nu \frac{U_\nu}{2} (n_{d\nu\uparrow} - n_{d\nu\downarrow})^2\right\} \quad (\text{B.2.3})$$

$$= \frac{1}{2} \sum_{S_\nu = \pm 1} \exp\left\{\sum_\nu \lambda_\nu S_\nu (n_{d\nu\uparrow} - n_{d\nu\downarrow})\right\}, \quad (\text{B.2.4})$$

where S_ν is the auxiliary Hubbard-Stratonovich field. The partition function is

$$Z = \text{Tr} [e^{-\beta H}]. \quad (\text{B.2.5})$$

By taking small time step in imaginary time with $\Delta\tau L = \beta$, we do the Trotter approximation

$$e^{-\Delta\tau(H_0+H_1)} = e^{-\Delta\tau H_0} e^{-\Delta\tau H_1} + \theta(\Delta\tau^2[H_0, H_1]). \quad (\text{B.2.6})$$

The partition function is rewritten:

$$Z = \text{Tr} [e^{-\beta H}] \quad (\text{B.2.7})$$

$$= \text{Tr} \left[\prod_{l=1}^L e^{-\Delta\tau(H_0+H_1)} \right] \quad (\text{B.2.8})$$

$$\simeq \text{Tr} \left[\prod_{l=1}^L e^{-\Delta\tau H_0} e^{-\Delta\tau H_1} + \theta(\Delta\tau^2) \right]. \quad (\text{B.2.9})$$

This is the only approximation in the QMC. By using the Hubbard-Stratonovich transformation and the Trotter approximation, we write the partition function.

$$\begin{aligned}
& Tr \left[\prod_{l=1}^L \exp \{-\Delta\tau H_0\} \times \exp \{-\Delta\tau H_1\} \right] \\
= & Tr \prod_{l=1}^L \frac{1}{2} \sum_{S_{l\nu} = \pm 1} \exp \left\{ -\Delta\tau \sum_{ij} a_{i\uparrow}^\dagger K_{ij} a_{j\uparrow} \right\} \exp \left\{ \sum_{\nu} \lambda_{\nu} S_{l\nu} n_{d\nu\uparrow} \right\} \\
& \times \exp \left\{ -\Delta\tau \sum_{ij} a_{i\downarrow}^\dagger K_{ij} a_{j\downarrow} \right\} \exp \left\{ \sum_{\nu} -\lambda_{\nu} S_{l\nu} n_{d\nu\downarrow} \right\} \quad (\text{B.2.10})
\end{aligned}$$

$$= \frac{1}{2^L} Tr \prod_{l=1}^L \sum_{S_{1\nu}, S_{2\nu}, \dots, S_{L\nu} = \pm 1} \exp \{-\Delta\tau H^\uparrow(l)\} \exp \{-\Delta\tau H^\downarrow(l)\}, \quad (\text{B.2.11})$$

where

$$H_0 = \sum_{i,j,\sigma} a_{i\sigma}^\dagger K_{ij} a_{j\sigma} \quad (\text{B.2.12})$$

$$H^\uparrow(l) = \sum_{ij} a_{i\uparrow}^\dagger K_{ij} a_{j\uparrow} - \frac{\sum_{\nu} \lambda_{\nu} S_{l\nu} n_{d\nu\uparrow}}{\Delta\tau} \quad (\text{B.2.13})$$

$$H^\downarrow(l) = \sum_{ij} a_{i\downarrow}^\dagger K_{ij} a_{j\downarrow} + \frac{\sum_{\nu} \lambda_{\nu} S_{l\nu} n_{d\nu\downarrow}}{\Delta\tau}. \quad (\text{B.2.14})$$

a denotes both c and d orbitals and now, we define

$$V_{\nu}^{\sigma} = \sigma \lambda_{\nu} S_{\nu}. \quad (\text{B.2.15})$$

$V_{\nu}^{\sigma} = \sigma \lambda_{\nu} S_{\nu} |\nu\rangle \langle \nu|$ only acts at the impurity sites and the matrix form of $e^{V_{\nu}^{\sigma}}$ is

$\vartheta_\nu(\sigma)$ is an $(N + 5)L \times (N + 5)L$ matrix, where \mathbf{K} is a $(N + 5) \times (N + 5)$ matrix for the bilinear part of the H and N is the number of the host states. Furthermore, the matrix representation of $e^{V_{l\nu}^\sigma}$ is

$$\begin{array}{c}
 \begin{array}{cccc}
 & l=1 & l=2 & l=3 & & l=L \\
 l=1 & \left[\begin{array}{c} \bullet \\ \bullet \\ \bullet \\ \bullet \\ 1 \\ \vdots \end{array} \right] & & & & \\
 & & (N+5) \times (N+5) & & & \mathbf{0} \\
 l=2 & & \left[\begin{array}{c} \bullet \\ \bullet \\ \bullet \\ \bullet \\ 1 \\ \vdots \end{array} \right] & & & \\
 & & & (N+5) \times (N+5) & & \\
 l=3 & & & \left[\begin{array}{c} \bullet \\ \bullet \\ \bullet \\ \bullet \\ 1 \\ \vdots \end{array} \right] & & \\
 & & & & (N+5) \times (N+5) & \\
 & & \mathbf{0} & & & \\
 l=L & & & & & \left[\begin{array}{c} \bullet \\ \bullet \\ \bullet \\ \bullet \\ 1 \\ \vdots \end{array} \right] \\
 & & & & & L(N+5) \times L(N+5)
 \end{array}
 \end{array}$$

In this matrix, d orbitals are shown with the bullets and the host states are 1. Moreover, the matrix elements at the $l \neq l'$ and $\nu \neq \nu'$ are zero.

B.3. Dyson's Equation for the Green's Functions

We define the single particle Green's function as

$$G_{\nu\nu'}^\sigma = - \left\langle T_\tau d_{\nu\sigma} d_{\nu'\sigma}^\dagger \right\rangle \quad (\text{B.3.1})$$

$$= \frac{-Tr T_\tau e^{-\beta H} d_{\nu\sigma}(l) d_{\nu'\sigma}^\dagger(l')}{Tr e^{-\beta H}}. \quad (\text{B.3.2})$$

The relation between the $\vartheta_\nu(\sigma)$ and the Green's function is

$$G_{\nu\nu'}^\sigma = (\vartheta_\nu(\sigma))^{-1}. \quad (\text{B.3.3})$$

Similar to the single-orbital case, the new configuration Green's function $G'_{\nu\nu'}$ and the old configuration Green's function $G_{\nu\nu'}$ are related to each other by a Dyson's equation (by omitting σ)

$$G'_{\nu\nu'} = G_{\nu\nu'} + (G_{\nu\nu'} - I) (e^{V'_\nu - V_\nu} - I) G'_{\nu\nu'}. \quad (\text{B.3.4})$$

B.4. Impurity Green's Function for the New Hubbard-Stratonovich Field Configuration

After the spin $S_{i\nu}$ is flipped, the new impurity Green's function is obtained from the relation

$$G'_{\nu\nu'} = G_{\nu\nu'} + (G_{\nu\nu'} - I) (e^{V'_{i\nu} - V_{i\nu}} - I) G'_{\nu\nu'}. \quad (\text{B.4.1})$$

By substituting

$$G'_{\nu\nu'} = [I - (G_{\nu\nu'} - I) (e^{V'_{i\nu} - V_{i\nu}} - I)]^{-1} G_{\nu\nu'}, \quad (\text{B.4.2})$$

we have

$$\begin{aligned} G'_{\nu\nu'} &= G_{\nu\nu'} + (G_{\nu\nu'} - I) (e^{V'_{i\nu} - V_{i\nu}} - I) \\ &\quad \times [I - (G_{\nu\nu'} - I) (e^{V'_{i\nu} - V_{i\nu}} - I)]^{-1} G_{\nu\nu'}. \end{aligned} \quad (\text{B.4.3})$$

We define

$$A = I + (I - G_{\nu\nu'}) (e^{V'_{i\nu} - V_{i\nu}} - I). \quad (\text{B.4.4})$$

After $S_{i\nu}$ is flipped, the new impurity Green's function is given by

$$\begin{aligned} G'_{\nu\nu'}(l_1, l_2) &= G_{\nu\nu'}(l_1, l_2) \\ &+ \sum_{l_3, l_4} (G_{\nu\nu'} - I)_{l_1, l_3} (e^{V'_{i\nu} - V_{i\nu}})_{l_3, l_3} (A^{-1})_{l_3, l_4} (G_{\nu\nu'})_{l_4, l_2}. \end{aligned} \quad (\text{B.4.5})$$

Hence

$$\begin{aligned} G'_{\nu\nu'}(l_1, l_2) &= G_{\nu\nu'}(l_1, l_2) \\ &+ \sum_{l_4} (G_{\nu\nu'}(l_1, l) - \delta_{l_1, l} \delta_{\nu, \nu'}) (e^{V'_{i\nu} - V_{i\nu}}) (A^{-1})_{l, l_4} (G_{\nu\nu'})_{l_4, l_2}. \end{aligned} \quad (\text{B.4.6})$$

We define

$$\left(e^{V'_{i\nu} - V_{i\nu}} \right) = \delta_{\nu\nu'} \delta_{i\nu'} e^{\sigma \lambda_{\nu'} (S_{i\nu'} - S_{i\nu})} \quad (\text{B.4.7})$$

so

$$(A^{-1})_{l, l_4; \nu, \nu'} = \delta_{l l_4} \delta_{\nu \nu'} \frac{1}{[I + (I - G_{\nu\nu'}(l, l))(e^{V'_{i\nu} - V_{i\nu}}) - I]}. \quad (\text{B.4.8})$$

Hence

$$\begin{aligned} G'_{\nu\nu'}(l_1, l_2) &= G_{\nu\nu'}(l_1, l_2) + (G_{\nu\nu'}(l_1, l) - \delta_{l_1, l} \delta_{\nu, \nu'}) (e^{V'_{i\nu} - V_{i\nu}} - I) \\ &\times \frac{1}{[I + (I - G_{\nu\nu'}(l, l))(e^{V'_{i\nu} - V_{i\nu}}) - I]} G_{\nu\nu'}(l, l_2) \end{aligned} \quad (\text{B.4.9})$$

B.5. Ratio of the Fermion Determinants

For a proposed change of the HS field $S_{l\nu}$,

$$S_{l\nu} \rightarrow S'_{l\nu} = -S_{l\nu} \quad (\text{B.5.1})$$

As in the single-orbital case, the probability of acceptance of the new configuration is proportional to the ratio of determinants of the new and old configuration.

$$R_{\nu\sigma} = \frac{\det \vartheta_{S'_{l\nu}}(\sigma)}{\det \vartheta_{S_{l\nu}}(\sigma)} = I + [I - G_{\nu\nu'}^\sigma(l, l)] (e^{V_{l\nu}^{\sigma'}} - e^{-V_{l\nu}^\sigma} - I). \quad (\text{B.5.2})$$

In order to prove this, we start from

$$\tilde{G}'_{\nu\nu'} = \tilde{G}_{\nu\nu'} - \tilde{G}_{\nu\nu'} (e^{-V'_{l\nu}} - e^{-V_{l\nu}}) \tilde{G}'_{\nu\nu'}, \quad (\text{B.5.3})$$

where

$$\tilde{G}_{\nu\nu'} = e^{V_{l\nu}} G_{\nu\nu'}. \quad (\text{B.5.4})$$

Multiplying both sides with $(\tilde{G}'_{\nu\nu'})^{-1}$ on the right, we get

$$I = \tilde{G}_{\nu\nu'} (\tilde{G}'_{\nu\nu'})^{-1} - \tilde{G}_{\nu\nu'} (e^{-V'_{l\nu}} - e^{-V_{l\nu}}). \quad (\text{B.5.5})$$

Hence

$$\tilde{G}_{\nu\nu'} (\tilde{G}'_{\nu\nu'})^{-1} = I + \tilde{G}_{\nu\nu'} (e^{-V'_{l\nu}} - e^{-V_{l\nu}}). \quad (\text{B.5.6})$$

Since

$$\tilde{G}_{\nu\nu'} = e^{V_{l\nu}} G_{\nu\nu'} = e^{V_{l\nu}} \vartheta_{l\nu}^{-1}, \quad (\text{B.5.7})$$

we have

$$(e^{V_{l\nu}} \vartheta_{l\nu}^{-1}) \left[e^{V_{l\nu}'} (\vartheta_{l\nu}')^{-1} \right]^{-1} = I + e^{V_{l\nu}} G_{\nu\nu'} (e^{-V_{l\nu}'} - e^{-V_{l\nu}}), \quad (\text{B.5.8})$$

$$e^{V_{l\nu}} (\vartheta_{l\nu}^{-1} \vartheta_{l\nu}') e^{-V_{l\nu}'} = I + e^{V_{l\nu}} G_{\nu\nu'} (e^{-V_{l\nu}'} - e^{-V_{l\nu}}). \quad (\text{B.5.9})$$

Here, we multiply on the left with $e^{-V_{l\nu}}$ and on the right with $e^{V_{l\nu}'}$,

$$\vartheta_{l\nu}^{-1} \vartheta_{l\nu}' = e^{-V_{l\nu}} e^{V_{l\nu}'} + G_{\nu\nu'} (e^{-V_{l\nu}'} - e^{-V_{l\nu}}) e^{V_{l\nu}'} \quad (\text{B.5.10})$$

$$\vartheta_{l\nu}^{-1} \vartheta_{l\nu}' = e^{V_{l\nu}' - V_{l\nu}} + G_{\nu\nu'} (I - e^{V_{l\nu}' - V_{l\nu}}) \quad (\text{B.5.11})$$

$$= e^{V_{l\nu}' - V_{l\nu}} + (G_{\nu\nu'} - I)(I - e^{V_{l\nu}' - V_{l\nu}}) + I(I - e^{V_{l\nu}' - V_{l\nu}}). \quad (\text{B.5.12})$$

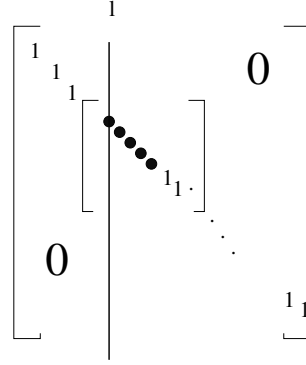
Hence

$$\vartheta_{l\nu}^{-1} \vartheta_{l\nu}' = I + (I - G_{\nu\nu'})(e^{V_{l\nu}' - V_{l\nu}} - I). \quad (\text{B.5.13})$$

By taking the determinant of the both sides, we obtain

$$\frac{\det \vartheta_{l\nu}'}{\det \vartheta_{l\nu}} = \det (I + (I - G_{\nu\nu'})(e^{V_{l\nu}' - V_{l\nu}} - I)) \quad (\text{B.5.14})$$

$(e^{V_{l\nu}' - V_{l\nu}} - I)$ has the non-zero elements only at the d sites so $I + (I - G_{\nu\nu'})(e^{V_{l\nu}' - V_{l\nu}} - I)$ has the form



In this matrix, the bullets show the impurity sites and the line denotes a single flip at an arbitrary l and ν orbital. This way

$$\det \left(I + (I - G_{\nu\nu'}) (e^{V'_{i\nu} - V_{i\nu}} - I) \right) = I + (I - G_{\nu\nu'}^{\sigma}(l, l)) (e^{V'_{i\nu} - V_{i\nu}} - I). \quad (\text{B.5.15})$$

Hence

$$R_{\nu\sigma} = I + (I - G_{\nu\nu'}^{\sigma}(l, l)) (e^{V'_{i\nu} - V_{i\nu}} - I). \quad (\text{B.5.16})$$

In heat-bath method, the transition probability from one state $S_{l\nu}$ to another state $S'_{l\nu}$ is

$$P(S_{l\nu} \rightarrow S'_{l\nu}) = \frac{1}{\prod_{\nu\sigma} R_{\nu\sigma} + 1} \quad (\text{B.5.17})$$

Then, by random number generator, if

$$P > \text{random number} \longrightarrow \text{accept}$$

else reject.

B.6. Impurity Green's Functions for the Multi-Orbital Case for When the Hubbard-Stratonovich Field is Zero

The impurity and host Green's functions with no hybridization and no Coulomb interaction are given by

$$G_{\nu\nu'}^{00} = \frac{\delta_{\nu\nu'}}{i\omega_n - (\epsilon_{d\nu} - \mu)} \quad \text{and} \quad G_m^{00}(i\omega_n) = \frac{1}{i\omega_n - (\epsilon_m - \mu)}. \quad (\text{B.6.1})$$

The Green's function with hybridization and no Coulomb interaction can be evaluated by using the following diagrams

Figure B.1. Feynman diagram representing the impurity Green's function $G_{\nu\nu'}^0(i\omega_n)$ for the $U = 0$. The double lines denote $G_{\nu\nu'}^0(i\omega_n)$ while the single lines denote $G_m^{00}(i\omega_n)$ and $G_{\nu''\nu''}^0(i\omega_n)$, respectively.

$$G_{\nu\nu'}^0(i\omega_n) = G_{\nu\nu'}^{00}(i\omega_n) + \sum_{\nu''} G_{\nu\nu'}^{00}(i\omega_n) \times \left\{ \sum_m V_{\nu m} V_{m\nu''} G_m^{00}(i\omega_n) \right\} G_{\nu''\nu''}^0(i\omega_n) \quad (\text{B.6.2})$$

and let's define the self-energy

$$F_{\nu\nu''}(i\omega_n) \equiv \sum_m V_{\nu m} V_{m\nu''} \frac{1}{i\omega_n - (\epsilon_m - \mu)}. \quad (\text{B.6.3})$$

Then;

$$G_{\nu\nu'}^0(i\omega_n) = G_{\nu\nu'}^{00}(i\omega_n) + G_{\nu\nu'}^{00}(i\omega_n) \sum_{\nu''} F_{\nu\nu''}(i\omega_n) G_{\nu''\nu''}^0(i\omega_n), \quad (\text{B.6.4})$$

$$G_{\nu\nu'}^0(i\omega_n) = G_{\nu\nu'}^{00} \left\{ 1 + \underbrace{\sum_{\nu''} F_{\nu\nu''}(i\omega_n) G_{\nu''\nu'}^0(i\omega_n)}_{T_{\nu\nu'}(i\omega_n)} \right\}. \quad (\text{B.6.5})$$

$$T_{\nu\nu'}(i\omega_n) = 1 + \sum_{\nu''} F_{\nu\nu''}(i\omega_n) G_{\nu''\nu'}^0(i\omega_n). \quad (\text{B.6.6})$$

$$\sum_{\nu''} T_{\nu\nu''}(i\omega_n) G_{\nu''\nu'}^0(i\omega_n) = G_{\nu\nu'}^{00}(i\omega_n). \quad (\text{B.6.7})$$

So

$$G_{\nu\nu'}^0(i\omega_n) = \sum_{\nu''} T_{\nu\nu''}^{-1}(i\omega_n) G_{\nu''\nu'}^{00}(i\omega_n) \quad (\text{B.6.8})$$

Up to now, we have got $i\omega_n$ dependent Green's functions. Now, all Green's functions are transformed to imaginary time space to be used in the Hirsch-Fye algorithm. Here, $G^0(l, l')$ is defined by

$$G_{\nu\nu'}^0(l, l') = T \sum_{i\omega_n} e^{-i\omega_n \Delta\tau(l-l')} G_{\nu\nu'}^0(i\omega_n) \quad (\text{B.6.9})$$

for $l, l' = 1, \dots, L$. However, for $l = l'$ cases, attention is required for implementation of boundary conditions in τ_l space. For $l = l'$, we define $G_{\nu\nu'}^0(l, l)$

$$G_{\nu\nu'}^0(l, l) = \lim_{\tau \rightarrow 0^+} T \sum_{i\omega_n} e^{-i\omega_n \tau} G_{\nu\nu'}^0(i\omega_n). \quad (\text{B.6.10})$$

We evaluate this expression from

$$G_{\nu\nu'}^0(l, l) = \left(T \sum_{i\omega_n} G_{\nu\nu'}^0(i\omega_n) - T \sum_{i\omega_n} \frac{1}{i\omega_n - (\varepsilon_{d\nu} + \frac{U_\nu}{2})} \right) - \left[1 - f(\varepsilon_{d\nu} + \frac{U_\nu}{2}) \right]. \quad (\text{B.6.11})$$

Our choice for $l = l'$ gives,

$$G_{\nu\nu'}^0(l, l) = - \left\langle T_\tau c_\nu(\tau_l) c_{\nu'}^\dagger(\tau_l) \right\rangle_0 \quad (\text{B.6.12})$$

$$= -[1 - \left\langle c_\nu(\tau_l) c_{\nu'}^\dagger(\tau_l) \right\rangle_0] \quad (\text{B.6.13})$$

$$= -[1 - \langle n_{d\nu\sigma} \rangle_0]. \quad (\text{B.6.14})$$

In the program, we calculate $G_{\nu\nu'}^0(l, l')$ for $l \neq l'$ and $l, l' = 1, \dots, L$ cases. After that, we use

$$G_{\nu\nu'}^0(\tau_l) = -G_{\nu\nu'}^0(\tau_l + \beta) = -G_{\nu\nu'}^0(\tau_{l+L}) \quad (\text{B.6.15})$$

to obtain $G_{\nu\nu'}^0(\tau_l)$ for $-L \leq l \leq -1$ and $l = L$.

B.7. Procedure to Update Impurity Green's Functions

Procedure to update Green's functions are the same in the case of single orbital Hirsch-Fye algorithm. Firstly, we calculate the $G_{\nu\nu'}^0(i\omega_n)$ which is the Green's function for non-zero hybridization and no Hubbard field. After that, for an initial spin configuration, $G_{\nu\nu'}(l, l')$ is calculated. State of whole system is changed from $S_{l\nu}$ to $S_{l\nu}'$ with probability $P(S_{l\nu} \rightarrow S_{l\nu}')$. Then the Green's function is updated if $P(S_{l\nu} \rightarrow S_{l\nu}')$ is larger than the random number which is generated from 1 to 0.

B.8. Flow chart for the HFQMC algorithm

- Calculate the non-interacting (HS field = 0) Green's function G^0 .
- By random number generator, choose starting HS field configuration.
- Calculate the Green's function G from the below equation,

$$G_{\nu\nu'}(l_1, l_2) = A_{\nu\nu'}(l_1, l_2) G_{\nu\nu'}^0(l_1, l_2) \quad (\text{B.8.1})$$

where

$$A_{\nu\nu'}(l_1, l_2) = \delta_{l_1, l_2} \delta_{\nu\nu'} e^{\lambda_{\nu\sigma} S_{l_2\nu}} - G_{\nu\nu'}^0(l_1, l_2) (e^{\lambda_{\nu\sigma} S_{l_2\nu}} - 1) \quad (\text{B.8.2})$$

- Choose imaginary time slice and $3d$ orbital randomly for spin flip and accept or reject the spin flip with respect to heat-bath QMC algorithm.
- Calculate the new Green's function $G'_{\nu\nu'}$ by using Dyson's equation.

$$G'_{\nu\nu'}(l_1, l_2) = G_{\nu\nu'}(l_1, l_2) + (G_{\nu\nu'}(l_1, l) - \delta_{l_1, l} \delta_{\nu\nu'}) (e^{V'_{l\nu} - V_{l\nu}} - I) \\ \times \frac{1}{[I + (I - G_{\nu\nu'}(l, l))(e^{V'_{l\nu} - V_{l\nu}} - I)]} G_{\nu\nu'}(l, l_2) \quad (\text{B.8.3})$$

- After certain number of warm up sweeps, the system reaches the equilibrium.
- Then, measurements start. In order to eliminate the correlations, a few update sweeps between the measurements should be considered.
- Finally, calculate the averages and standart deviation of the measurements.

APPENDIX C

CALCULATION OF THE HOST-IMPURITY AND HOST GREEN'S FUNCTIONS

In this appendix, host-impurity and host Green's functions are calculated for multi-orbital case. These equations were used for single-orbital HFQMC in [19].

Up to now, electronic and magnetic properties of Co $3d$ have been studied. To find the magnetic properties of vitamin B₁₂, impurity-host and host Green's functions must be calculated. Details of all calculations have been explained in Appendix A and Appendix B for $3d$ orbitals. Host-impurity and host Green's functions are calculated in the same way.

C.1. Calculation of $G_{m\nu}$

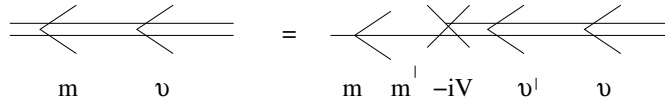


Figure C.1. Feynman diagram representing the Green's function $G_{m\nu}^0(i\omega_n)$ for $S_{lv} = 0$. The double lines denote the host-impurity Green's function $G_{m\nu}^0(i\omega_n)$ and the impurity Green's function $G_{\nu\nu'}^0(i\omega_n)$, respectively and the single line denotes the host Green's function $G_{mm'}^{00}(i\omega_n)$ for no hybridization and no Hubbard-Stratonovich field. Here, m is the index of host states and ν is the index of impurity orbitals.

By using above Feynman diagram, host-impurity Green's functions for zero Hubbard-Stratonovich field are calculated as

$$iG_{m\nu}^0(i\omega_n) = \sum_{m'=1}^{N_{host}} \sum_{\nu'=1}^5 iG_{mm'}^{00}(-iV_{m'\nu'}) iG_{\nu'\nu}^0(i\omega_n) \quad (C.1.1)$$

$$G_{m\nu}^0(i\omega_n) = \sum_{m'=1}^{N_{host}} \sum_{\nu'=1}^5 G_{mm'}^{00}(V_{m'\nu'}) G_{\nu'\nu}^0(i\omega_n). \quad (C.1.2)$$

where

$$G_{mm'}^{00} = \frac{\delta_{mm'}}{i\omega_n - (\varepsilon_m - \mu)} \quad (\text{C.1.3})$$

and $G_{\nu'\nu}^0$ is calculated in Appendix B. Here, Green's functions are defined by

$$G_{m\nu}^0(\tau, \tau') = - \langle T_\tau c_{m\sigma}(\tau) d_{\nu\sigma}^\dagger(\tau') \rangle, \quad (\text{C.1.4})$$

$$G_{m\nu}^0(\tau, \tau') = G_{m\nu}^0(\tau - \tau') \quad (\text{C.1.5})$$

By Fourier transformation,

$$G_{m\nu}^0(l, l') = T \sum_{i\omega_n} e^{i\omega_n(\tau_l - \tau_{l'})} G_{m\nu}^0(i\omega_n) \quad (\text{C.1.6})$$

and

$$G_{m\nu}^0(l, l') \longrightarrow G_{m\nu}^0(l, l', m, \nu) \quad (\text{C.1.7})$$

Here,

$$l \longrightarrow 1 : L \quad (\text{C.1.8})$$

$$l' \longrightarrow 1 : L \quad (\text{C.1.9})$$

$$m \longrightarrow 1 : N_{host} \quad (\text{C.1.10})$$

$$\nu \longrightarrow 1 : Nd. \quad (\text{C.1.11})$$

l and l' are imaginary time slice for host and impurity, respectively. m defines host orbitals and the total host orbitals is $N_{host} = 2431$. ν is Co $3d$ orbitals and total $3d$ orbitals are $Nd = 5$.

In Appendix B, by using Dyson's equation, $G_{\nu\nu'}$ has been calculated for non-zero Hubbard-Stratonovich fields. In the same way, $G_{m\nu}$ is found by Dyson equation from the $G_{m\nu}^0$ which is zero HS field Green's functions. (Forms of Dyson equations have been proved in Appendix A.)

$$G_{m\nu} = G_{m\nu}^0 + G_{m\nu}^0 (e^{V_{l\nu}} - I) G_{\nu\nu'} \quad (\text{C.1.12})$$

and

$$(G_{m\nu})_{l_1, l_2} = (G_{m\nu}^0)_{l_1, l_2} + \sum_{l_3=1}^L (G_{m\nu}^0)_{l_1, l_3} [e^{V_{l\nu}} - I]_{l_3, l_3} (G_{\nu\nu'})_{l_3, l_2} \quad (\text{C.1.13})$$

Here, l_1 is used for host orbitals, l_2 and l_3 is used for $3d$ orbitals. At this point, the most important point is that spin flip must be at both same l and same $3d$ orbital.

C.1.1. Calculation of the Updated $G'_{m\nu}$

By using $G_{m\nu}^0$ Green's functions, non-zero HS field Green's functions $G_{m\nu}$ have been obtained. In this subsection, the new HS field Green's functions are calculated from $G_{m\nu}$ and Dyson equation is used.

$$G'_{m\nu} = G_{m\nu} + G_{m\nu} (e^{V_{l\nu}} - I) G'_{\nu\nu'} \quad (\text{C.1.14})$$

Spin flips occur the same l and same $3d$ orbital so

$$\begin{aligned} (e^{V_{l\nu}^\sigma})_{l\nu', \nu\nu'} &= \delta_{l\nu'} \delta_{\nu\nu'} e^{\sigma \lambda S_{l\nu}} \\ S'_{l\nu} &= -S_{l\nu} \end{aligned} \quad (\text{C.1.15})$$

and

$$V_{l\nu}^{\sigma'} = \sigma \lambda S_{l\nu} \quad (\text{C.1.16})$$

Then

$$V_{l\nu}^{\sigma'} - V_{l\nu}^{\sigma} = (-\sigma\lambda_{\nu}S_{l\nu}) - (\sigma\lambda_{\nu}S_{l\nu}) = -2\sigma\lambda_{\nu}S_{l\nu} \quad (\text{C.1.17})$$

and

$$(e^{(V_{l\nu}^{\sigma'} - V_{l\nu}^{\sigma})})_{ll} = e^{-2\sigma\lambda_{\nu}S_{l\nu}}. \quad (\text{C.1.18})$$

By using Eq.C.1.15,

$$(e^{(V_{l\nu}^{\sigma'} - V_{l\nu}^{\sigma})} - I)_{l_1, l_2} = \delta_{l, l_1} \delta_{l, l_2} (e^{-2\sigma\lambda_{\nu}S_{l\nu}} - 1). \quad (\text{C.1.19})$$

If above equation is multiplied by $3d$ Green's functions,

$$[(e^{(V_{l\nu}^{\sigma'} - V_{l\nu}^{\sigma})} - I) G_{\nu\nu'}]_{l_1, l_2} = \delta_{l, l_1} e^{-2\sigma\lambda_{\nu}S_{l\nu}} (G_{\nu\nu'})_{l, l_2} \quad (\text{C.1.20})$$

is obtained. After that, Eq.C.1.20 is multiplied with host-impurity Green's functions and

$$\begin{aligned} [G_{m\nu} \sum_{l_3} (e^{V_{l\nu}^{\sigma'} - V_{l\nu}^{\sigma}} - I) G_{\nu\nu'}]_{l_1, l_2} &= \\ \sum_{l_3} (G_{m\nu})_{l_1, l_3} [(e^{V_{l\nu}^{\sigma'} - V_{l\nu}^{\sigma}} - I) G_{\nu\nu'}]_{l_3, l_2} &= (G_{m\nu})_{l_1, l} e^{-2\sigma\lambda_{\nu}S_{l\nu}} (G_{\nu\nu'})_{l, l_2} \end{aligned} \quad (\text{C.1.21})$$

the above equation is found. The Dyson equation for $G'_{m\nu}$ is

$$G'_{m\nu} = G_{m\nu} + G_{m\nu} + G_{m\nu} (e^{V_{l\nu}^{\sigma'} - V_{l\nu}^{\sigma}} - I) G'_{\nu\nu'} \quad (\text{C.1.22})$$

and by Eq.C.1.21,

$$(G'_{m\nu})_{l_1, l_2} = (G_{m\nu})_{l_1, l_2} + (G_{m\nu})_{l_1, l} e^{-2\sigma\lambda_{\nu}S_{l\nu}} (G_{\nu\nu'})_{l, l_2} \quad (\text{C.1.23})$$

the new HS field Green's functions are calculated.

C.2. Calculation of $G_{\nu m}$

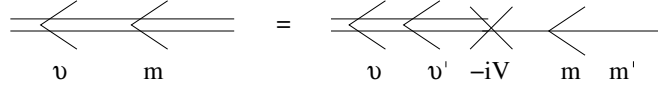


Figure C.2. Feynman diagram representing the Green's function $G_{\nu m}^0(i\omega_n)$ for $S_{I\nu} = 0$. The double lines denote the impurity-host Green's function $G_{\nu m}^0(i\omega_n)$ and the impurity Green's function $G_{\nu\nu'}^0(i\omega_n)$, respectively and the single line denotes the host Green's function $G_{mm'}^{00}(i\omega_n)$ for no hybridization and no Hubbard-Stratonovich field. Here, m is the index of host states and ν is the index of impurity orbitals.

From Feynman diagram,

$$iG_{\nu m}^0(i\omega_n) = \sum_{m=1}^{N_{host}} \sum_{\nu'=1}^5 iG_{\nu\nu'}^0(i\omega_n) (-iV_{\nu'm}) iG_{mm'}^{00}(i\omega_n) \quad (\text{C.2.1})$$

$$G_{\nu m}^0(i\omega_n) = \sum_{m=1}^{N_{host}} \sum_{\nu'=1}^5 G_{\nu\nu'}^0(i\omega_n) (V_{\nu'm}) G_{mm'}^{00}(i\omega_n). \quad (\text{C.2.2})$$

impurity-host Green's functions are calculated. Here, it is seen that host-impurity Green's functions and impurity-host Green's functions equal.

$$G_{m\nu}^0(i\omega_n) = G_{\nu m}^0(i\omega_n) \quad (\text{C.2.3})$$

C.3. Calculation of the Updated $G'_{\nu m}$

The new HS field Green's functions are calculated from Dyson equation:

$$G'_{\nu m} = G_{\nu m} + (G'_{\nu\nu'} - I) (I - e^{-(V'_{l\nu} - V_{l\nu})}) G_{\nu m}. \quad (\text{C.3.1})$$

In the case of single spin flip,

$$S'_{l\nu} = -S_{l\nu} \quad (\text{C.3.2})$$

$$V_{l\nu}^{\sigma'} = \sigma \lambda_{\nu} S_{l\nu} \quad (\text{C.3.3})$$

Then

$$V_{l\nu}^{\sigma'} - V_{l\nu}^{\sigma} = (-\sigma \lambda_{\nu} S_{l\nu}) - (\sigma \lambda_{\nu} S_{l\nu}) = -2\sigma \lambda_{\nu} S_{l\nu} \quad (\text{C.3.4})$$

$$(e^{(V_{l\nu}^{\sigma'} - V_{l\nu}^{\sigma})})_{ll} = e^{-2\sigma \lambda_{\nu} S_{l\nu}} \quad (\text{C.3.5})$$

$$(e^{(V_{l\nu}^{\sigma'} - V_{l\nu}^{\sigma})} - I)_{l_1, l_2} = \delta_{l, l_1} \delta_{l, l_2} (e^{-2\sigma \lambda_{\nu} S_{l\nu}} - 1) \quad (\text{C.3.6})$$

$$\begin{aligned} (G'_{\nu m})_{l_1, l_2} &= (G_{\nu m})_{l_1, l_2} \\ &+ \sum_{l_3, l_4} (G'_{\nu\nu'} - I)_{l_1, l_3} (I - e^{-(V'_{l\nu} - V_{l\nu})})_{l_3, l_4} (G_{\nu m})_{l_4, l_2} \end{aligned} \quad (\text{C.3.7})$$

$$\begin{aligned} &= (G_{\nu m})_{l_1, l_2} \\ &+ \sum_{l_3, l_4} (G'_{\nu\nu'} - I)_{l_1, l_3} \delta_{l, l_3} \delta_{l, l_4} (1 - e^{2\sigma \lambda_{\nu} S_{l\nu}}) (G_{\nu m})_{l_4, l_2} \end{aligned} \quad (\text{C.3.8})$$

and so the HS field impurity-host Green's functions are obtained. From Eq.C.3.8,

$$(G'_{\nu m})_{l_1, l_2} = (G_{\nu m})_{l_1, l_2} + ((G'_{\nu \nu'})_{l_1, l} - \delta_{l_1, l}) (1 - e^{2\sigma \lambda_{\nu} S_{l\nu}}) (G_{\nu m})_{l, l_2}. \quad (\text{C.3.9})$$

C.4. Calculation of $G_{mm'}$

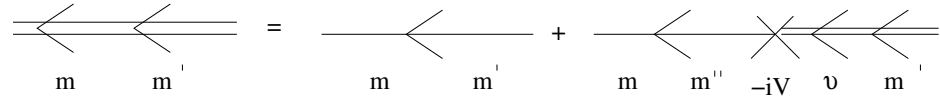


Figure C.3. Feynman diagram representing the host Green's function $G_{mm'}^0(i\omega_n)$ for $S_{l\nu} = 0$. The double lines denote the host Green's function $G_{mm'}^0(i\omega_n)$ and the impurity-host Green's function $G_{\nu m'}^0(i\omega_n)$, respectively and the single line denotes the host Green's function $G_{mm'}^{00}(i\omega_n)$ for no hybridization and no Hubbard-Stratonovich field. Here, m is the index of host states and ν is the index of impurity orbitals.

From Feynman diagram, host Green's function is calculated as the following:

$$iG_{mm'}(i\omega_n) = iG_{mm'}^{00}(i\omega_n) + \sum_{m''=1}^{N_{host}} iG_{mm''}^{00}(i\omega_n) \sum_{\nu=1}^5 (-iV_{m''\nu}) iG_{\nu m'}^0(i\omega_n), \quad (\text{C.4.1})$$

$$G_{mm'}^0(i\omega_n) = G_{mm'}^{00}(i\omega_n) + \sum_{m''=1}^{N_{host}} G_{mm''}^{00}(i\omega_n) \sum_{\nu=1}^5 V_{m''\nu} G_{\nu m'}^0(i\omega_n). \quad (\text{C.4.2})$$

Then

$$G_{mm'}^0(i\omega_n) = G_{mm'}^{00}(i\omega_n) + \sum_{m''=1}^{N_{host}} G_{mm''}^{00}(i\omega_n) \times \sum_{\nu=1}^5 V_{m''\nu} \left(\sum_{m=1}^{N_{host}} \sum_{\nu'=1}^5 G_{\nu\nu'}^0(i\omega_n) V_{\nu'm} G_{mm'}^{00}(i\omega_n) \right). \quad (\text{C.4.3})$$

By using Dyson equation, new HS fields Green's functions are obtained by Eq.C.4.4 and C.4.5.

$$G_{mm'} = G_{mm'}^0 + G_{m\nu}^0 (e^{-V_{l\nu}} - I) G_{\nu m} \quad (\text{C.4.4})$$

and

$$G'_{mm'} = G_{mm'} + G_{m\nu} (e^{(V'_{l\nu} - V_{l\nu})} - I) G'_{\nu m} \quad (\text{C.4.5})$$

C.5. Calculation of the Dynamical Magnetic Susceptibility $\chi_{\nu m}$

In this section, impurity-host dynamical magnetic susceptibility is defined as the following equation:

$$\chi_{\nu m}(\tau) = \langle (n_{\nu\uparrow}(\tau) - n_{\nu\downarrow}(\tau)) (n_{m\uparrow} - n_{m\downarrow}) \rangle \quad (\text{C.5.1})$$

$$= \langle (d_{\nu\uparrow}^\dagger(\tau) d_{\nu\uparrow}(\tau) - d_{\nu\downarrow}^\dagger(\tau) d_{\nu\downarrow}(\tau)) (c_{m\uparrow}^\dagger c_{m\uparrow} - c_{m\downarrow}^\dagger c_{m\downarrow}) \rangle_0 \quad (\text{C.5.2})$$

$$= \langle (d_{\nu\uparrow}^\dagger(\tau) d_{\nu\uparrow}(\tau) - d_{\nu\downarrow}^\dagger(\tau) d_{\nu\downarrow}(\tau)) (c_{m\uparrow}^\dagger c_{m\uparrow} - c_{m\downarrow}^\dagger c_{m\downarrow}) + d_{\nu\uparrow}(\tau) c_{m\uparrow}^\dagger d_{\nu\uparrow}^\dagger(\tau) c_{m\uparrow} + d_{\nu\downarrow}^\dagger(\tau) c_{m\downarrow} d_{\nu\downarrow}(\tau) c_{m\downarrow}^\dagger \rangle_{S_{l\nu}}. \quad (\text{C.5.3})$$

where 0 subscript indicates the all contractions and the $S_{l\nu}$ subscript means that the Monte Carlo average over the Hubbard Stratonovich fields is performed. We know that

$$G_{\nu\nu'\sigma}(\tau, \tau') = - \langle T_\tau d_{\nu\sigma}(\tau) d_{\nu'\sigma}^\dagger(\tau') \rangle \quad (\text{C.5.4})$$

$$G_{\nu m\sigma}(\tau, \tau') = - \langle T_\tau d_{\nu\sigma}(\tau) c_{m\sigma}^\dagger(\tau') \rangle \quad (\text{C.5.5})$$

$$G_{m\nu\sigma}(\tau, \tau') = - \langle T_\tau c_{m\sigma}(\tau) d_{\nu'\sigma}^\dagger(\tau') \rangle. \quad (\text{C.5.6})$$

Then, the magnetic susceptibility equals

$$\begin{aligned} \chi_{\nu m}(\tau) = & \langle (G_{\nu\nu\uparrow}(\tau, \tau) - G_{\nu\nu\downarrow}(\tau, \tau)) (G_{mm\uparrow}(0, 0) - G_{mm\downarrow}(0, 0)) \\ & - G_{\nu m\uparrow}(\tau, \tau') G_{m\nu\uparrow}(0, \tau) - G_{\nu m\downarrow}(\tau, 0) G_{m\nu\downarrow}(0, \tau) \rangle_{S_{iv}}. \end{aligned} \quad (\text{C.5.7})$$

By Fourier transformation, the impurity-host magnetic susceptibility is

$$\chi_{m\nu}(i\omega_m) = \int_0^\beta d\tau e^{i\omega_m\tau} \chi_{m\nu}(\tau), \quad (\text{C.5.8})$$

and especially the magnetic susceptibility for zero frequency is given by

$$\chi_{\nu m} = \int_0^\beta d\tau \chi_{\nu m}(\tau). \quad (\text{C.5.9})$$